The Inclusion of Thermal Emissions Within the SASKTRAN Framework

A Thesis

Submitted to the Faculty of Graduate Studies and Research

in Partial Fulfillment of the Requirements

for the Degree of

Master of Science

in the Department of Physics and Engineering Physics

by

Kenneth Lorne Jensen

Saskatoon, Saskatchewan

March 2015

In presenting this thesis in partial fulfillment of the requirements for a Postgraduate degree from the University of Saskatchewan, the author agrees that the Libraries of this University may make it freely available for inspection. The author further agrees that permission for copying of this thesis in any manner, in whole or in part, for scholarly purposes may be granted by the professor who supervised this thesis work or, in his absence, by the Head of the Department or the Dean of the College in which this thesis work was done. It is understood that any copying or publication or use of this thesis or parts thereof for financial gain shall not be allowed without written approval from the author. It is also understood that due recognition shall be given to the author and to the University of Saskatchewan in any scholarly use which may be made of any material in this thesis.

Requests for permission to copy or to make other use of material in this thesis in whole or in part should be addressed to:

Head of the Department of Physics and Engineering Physics

116 Science Place

University of Saskatchewan

Saskatoon, Saskatchewan

Canada

S7N 5E2

To my parents, the most honest and hard-working people I know.

Abstract

The current capabilities of SASKTRAN – a radiative transfer model at the University of Saskatchewan in Saskatoon, Canada – are to accurately model the scattering of solar radiation within the earth's atmosphere for the ultraviolet-visible (UV-Vis) and near infra-red (NIR) regions of the electromagnetic spectrum. However, the current model does not account for the radiation emitted by the ground and atmosphere, approximated by the blackbody spectrum. In the UV-Vis, this contribution is unimportant, but when transitioning to wavelengths longer than 2.5 μm, the solar spectrum decreases in intensity while radiation of terrestrial and atmospheric origin increases along the blackbody curve. At wavelengths longer than 5 μm in the far infra-red (FIR), the blackbody radiation is the dominant source in the atmosphere. A modification to the source code of SASKTRAN was made in order to include the additional effect of this "thermal" radiation – with the help of the spectral line database HITRAN – while still maintaining scattering capabilities of solar radiation. This would make SASKTRAN one of the first radiative transfer models with the ability to model radiation in the difficult region between 3 and 5 μm – the mid infra-red (MIR) region – where the solar and thermal radiation sources are equally diminished and are the same order of magnitude.

An introduction is given to atmospheric physics with a focus on the science of infra-red active molecules like H_2O, CO_2, CH_4, N_2O, O_3, and CO – the so-called "greenhouse gases" – and the measurement techniques used to determine their atmospheric distribution. A theoretical basis is then provided for general radiative transfer, and the physics of molecular absorption and emission is examined in detail. A summary of the implementation of thermal radiation within the SASKTRAN framework is given, followed by verification studies where the model's radiative transfer calculations in the infra-red are compared against measurements, including those made by the ground-based instrument E-AERI, the space-borne instruments IASI and GOSAT, and against model results from the LBLRTM, another well-verified radiative transfer model.

Acknowledgements

I would like to express my thanks for the opportunity to perform this work as a member of the Institute of Space and Atmospheric Studies research team and as a student of the University of Saskatchewan. I further want to thank the Institute and the University for providing funding for this work.

I would also like to give thanks to a number of individuals within ISAS. My thanks goes to Landon Regeir, Chris Roth, Daniel Zawada, Seth Dueck, Barrett Taylor, Matt Kozun, Paul Loewen, and Brenden Elash for being excellent office mates. Special thanks goes to Landon, Dan, Seth, Brenden, and Chris for assisting me with software design in my project, and to Chris for maintaining a light-hearted atmosphere in the office. I would also like to extend thanks to Dr. Nick Lloyd for his helpful advice throughout the course of this work, and to Dr. Adam Bourassa, for his excellent instruction both in my undergraduate and graduate work. Finally, I want to express my thanks to my supervisor, Dr. Doug Degenstein. I am grateful to Doug Degenstein for his excellence in teaching, relaxed approach to otherwise stressful work, and his inspiring approach to science. I am thankful for the opportunity to have work with such an excellent group of scientists and people.

Finally, I am indebted to both my family, Garry, Luela, and Lindsay, and my girlfriend and love of my life, Katie, for their constant support and encouragement throughout my studies.

Contents

List of Figures

List of Tables

Glossary of Terms

E-AERI	Explanation
ϵ	Emissivity - a dimensionless ratio relating the radiative emitting ability of a substance to an ideal black body emitter.
EUMETSAT	European Organisation for the Exploitation of Meteorological SATellites.
FIR	Far Infra-red.
FTS	Fourier Transform Spectrometer.
GOSAT	Greenhouse gases Observing SATellite.
h	Planck's constant.
HITRAN	High Resolution Transmission, spectral line database.
IASI	Infrared Atmospheric Sounding Interferometer.
LBLRTM	Line-by-line radiative transfer model.

METOP Meteorological operations satellite, operated by EUMETSAT, housing numerous instruments, including IASI.

MIR Mid Infra-red.

NIR Near Infra-red.

OSIRIS Optical Spectrograph and InfraRed Imaging System.

$\sigma_X(\nu)$ Absorption cross section [cm^2] of molecule X at wavenumber ν.

SASKTRAN Radiative transfer model at the University of Saskatchewan.

SCIAMACHY SCanning Imaging Absorption spectroMeter for Atmospheric CHartographY.

SZA Solar zenith angle.

TCCON Total Carbon Column Observing Network.

$\tau(\nu)$ Optical depth (dimensionless) at a frequency ν.

$\tilde{\nu}$ Wavenumber [cm^{-1}].

UV Ultraviolet

UV-VIS Ultraviolet-visible portion of the spectrum, generally referring to the region between 300 nm and 800 nm

Chapter 1

Introduction

> There's a sunrise and a sunset every single day, and they're absolutely free. Don't miss so many of the them.
>
> Jo Walton

1.1 The Current State of the Climate

The state of the atmosphere on a global scale is more important than ever in the present day. Debates about what measures need to be taken to slow the progression of global warming are at the forefront of international meetings, such as the G7/G8 Summits and UN Climate Summits, leading to commitments by countries to take the first steps to combat climate change, such as outlined in the Kyoto Protocol. The weight of the issue is not lost on many - a warming earth would have incredible effects on the biosphere, leading to changing weather patterns, increasing number of wildfires, longer periods of drought, and an increase in the number, duration, and intensity of violent storms (Bernstein et al., 2007). The leading authority on the effects of climate change, the Intergovernmental Panel on Climate Change (IPCC), composed of 1300 scientists from around the world, predicts a rise of 1.4 to 5.6

degrees Celsius over the next century, in addition to a 20.0 cm rise in sea levels globally (Bernstein et al., 2007). The IPCC (Bernstein et al., 2007) even goes so far as to predict the effects a warming climate would have regionally by saying,

- **North America**: Decreasing snowpack in the western mountains; 5-20 percent increase in yields of rain-fed agriculture in some regions; increased frequency, intensity and duration of heat waves in cities that currently experience them.

- **Latin America**: Gradual replacement of tropical forest by savannah in eastern Amazonia; risk of significant biodiversity loss through species extinction in many tropical areas; significant changes in water availability for human consumption, agriculture and energy generation.

- **Europe**: Increased risk of inland flash floods; more frequent coastal flooding and increased erosion from storms and sea level rise; glacial retreat in mountainous areas; reduced snow cover and winter tourism; extensive species losses; reductions of crop productivity in southern Europe.

- **Africa**: By 2020, between 75 and 250 million people are projected to be exposed to increased water stress; yields from rain-fed agriculture could be reduced by up to 50 percent in some regions by 2020; agricultural production, including access to food, may be severely compromised.

- **Asia**: Freshwater availability projected to decrease in Central, South, East and Southeast Asia by the 2050s; coastal areas will be at risk due to increased flooding; death rate from disease associated with floods and droughts expected to rise in some regions.

The projected impacts of climate change & global warming are indeed sobering. Therefore it is of key economic interest to investigate all possible causes of the current warming trend (Bernstein et al., 2007), and the role all constituents of the atmosphere play in its warming and cooling. The general consensus among the scientific community is that the relatively recent rise in global surface temperatures is due to the increased presence of water vapour, carbon dioxide, methane, nitrous oxides, and chlorofluorocarbons present in the atmosphere. These molecules occur naturally in the atmosphere, and contribute to the process known as the "greenhouse effect", where molecules act as a "blanket" to the earth, trapping outgoing longwave radiation emitted from the surface, and subsequently warming the earth. However, the advent of the industrial age and increased methane and carbon dioxide output from automobiles, factories, power plants, and large-scale farming operations, as well as an increasing world population, has increased the atmospheric content of these gases, resulting in an accelerated warming of the earth (Bernstein et al., 2007; Oreskes, 2004; Maslin, 2004).

Thus the measurement of these so-called "greenhouse gases" is an important field of study and is vital in understanding how to reduce humanity's impact on the atmosphere. To achieve this, spectroscopic techniques are used in both ground- and satellite-based instruments to examine the composition of the atmosphere and determine how the molecules react to varying wavelengths of electromagnetic radiation. These techniques have been used by scientists to investigate the composition of materials for over two centuries.

1.2 A Short History of Spectroscopy

Isaac Newton, in 1666, discovered that white light from the sun was actually composed of a continuous *spectrum* of coloured light, by use of a prism. In 1800, William Herschel discovered radiation lying beyond the red end of the spectrum, the so-called "infra-red" light. One of the most significant discoveries occurred in 1802, when William Hyde Wollaston observes dark lines in the spectrum of the sun. These lines were examined in detail in 1814 by Joseph

von Frauenhofer, who went on to build the first diffraction grating, and used it in 1823 to observe the spectra of the Moon, Mars, Venus, and several bright stars. Dark lines would appear in these spectra too, but at different locations along the spectrum (Thomsen, 2006).

John Herschel was the first to suggest in 1823 that it may be possible to determine chemical make-up from a material's spectrum, and in 1859 Gustav Robert Kirchhoff and Robert Wilhelm Eberhard von Bunsen discovered that these spectral lines were indeed unique to each element, and that it was the element absorbing light at specific wavelengths between the light source and observer that caused these lines. In 1860, Kirchhoff and Bunsen discover cesium and rubidium using their new spectral analysis techniques. By the year 1853, Anders Jonas Angström measured the hydrogen spectral line locations, which were later shown to exist in the solar spectrum. By 1868, the element helium was discovered through its absorption lines appearing in the solar spectrum, and was named for the Greek term for the sun, Helios (Thomsen, 2006).

The following years showed improved experimental techniques and increased precision in measurements, in addition to a deeper understanding of electromagnetic and absorption theory. Further understanding of the wavelength dependence of these spectral lines was contributed by Einstein (1905), Planck (1900), Lyman (1906), Rydberg (1888), and Balmer (1885), Heisenberg (1925), and Schrödinger (1926), among others (Thomsen, 2006).

By the turn of the nineteenth century, scientists started turning their knowledge of spectroscopy to investigate the earth's atmosphere. It was already evident that the absorption of radiation by the atmosphere had an important effect on the climate, as work from Fourier, Tyndall, Langley, Heine, Angström, Paschen, Röntgen, Pouillet, and others in the mid-19th century suggested (Arrhenius, 1896). This work motivated Svante Arrhenius to work on a theory in 1896 to explain the cause of the great ice ages originating from decreased levels of carbon dioxide, and subsequently calculated that human activity would warm the atmosphere by adding more carbon dioxide to the atmosphere (Maslin, 2004).

Arrhenius's work was independently confirmed by Thomas Chamberlain. Unfortunately, their work was largely shrugged off, as at the time human influences were thought insignificant compared to geological and astronomical forces (Maslin, 2004). However, with the improvement of infra-red spectroscopy in the mid and late 1940s, it was shown that small increases of carbon dioxide in a test volume of gas significantly increased the amount of absorption of incident infra-red radiation (Maslin, 2004).

A significant technical advance occurred in 1955 when Australian spectroscopist Alan Walsh developed atomic absorption spectroscopy (AAS), which has been deemed the most significant advance in technical analysis in the 20th century. Modern day spectrometers still operate with the basic techniques of AAS, albeit with improved precision (Thomsen, 2006). It was in this year that Gilbert Plass brought together the work of Arrhenius, Chamberlain, and the infra-red spectroscopy measurements of carbon dioxide in the 1940s together with the new spectroscopic techniques to conclude that adding more carbon dioxide to the earth's atmosphere would absorb more infra-red radiation from the ground, preventing it from being lost to space, thus warming the earth's surface (Maslin, 2004).

Plass's work justified the need for accurate measurements of atmospheric concentrations of carbon dioxide. Charles Keeling made manometric measurements twice a day at Mauna Loa observatory in Hawaii from 1958 to 2005 of carbon dioxide levels, resulting in what is known as the "Keeling curve", which although showing small seasonal variations, mainly serves to show that the concentration of atmospheric carbon dioxide has been steadily increasing since the 1950s until the present day (Harris, 2010a).

1.3 Techniques in Spectroscopy

Density measurements and knowledge of carbon dioxide's infra-red absorbing properties have led to programs devoted entirely to the measurement of atmospheric carbon dioxide, in

addition to other infra-red absorbing molecules. While there are multiple ways to measure the composition of air, the bulk of this thesis is concerned with remote sensing, and thus will focus on instruments that gather electromagnetic radiation - specifically in the infra-red.

Most optical spectrometers these days fall into one of two categories - Fourier transform spectrometers and diffraction grating spectrometers. Fourier transform spectrometers use a beamsplitter to divide source light into two beams - one which reflects off a fixed mirror, and the other off of a moveable mirror. The beams interfere, and the resulting intensity is related to the phase difference introduced by the moveable mirror, measuring the temporal coherence of the source light (essentially a frequency decomposition). Once completed for a range of mirror positions, the resulting measurement of intensities obtained is an *interferogram*. The spectrum of the light can be obtained by performing a Fourier transform on the interferogram.

Diffraction grating spectrometers utilize the fact that light of different wavelengths diffract through a diffraction grating at different angles. Once the light of different colours is spatially separated, it can be measured by individual pixels, producing a spectrum. These spectrometers can be mounted on satellite platforms, which allow for great spatial coverage of the atmosphere, but lower resolution. Spectrometers can also be ground-based or mounted on a balloon, which gives exceptional resolution, but very poor spatial coverage. It is a combination of these types of measurements spread globally that yield accurate time series on atmospheric composition and processes.

Spectroscopic measurements, though capable of achieving high precision, still cannot directly measure quantities of an absorbing material - essentially all that is measured is an intensity of light at very fine wavelength spacings. It is from these measurements that we must determine the *type* and *amount* of absorbing molecule(s) present, using our knowledge of radiative transfer theory (see chapter §3). Since the problem of electromagnetic radiation propagating in an absorbing and scattering material is quite complex, especially when dealing with the entire atmosphere, the work is left to a computer program called a radiative transfer model (RTM). With knowledge of *how* electromagnetic radiation propagates in air for a specific

configuration, one can find a regime of atmospheric molecules that yields the measurements made by a spectrometer - although this is much easier said than done!

There are two main types of RTMs - line-by-line models and band models. The former performs calculations of radiative transfer for very closely spaced frequencies, recalculating absorption and scattering parameters for each new frequency. Given highly absorbing molecules with thousands of absorption lines and/or complex scattering molecules, these RTMs are computationally intensive, but accurate. The latter, band models, assume the molecular parameters are roughly constant over some small frequency band, and thus fewer calculations have to be performed. The answers are less accurate, but give a good order-of-magnitude test for radiative transfer, especially when dealing with atmospheric radiative fluxes.

RTMs can be broken down into a few sub-categories. Depending on the wavelength regime being investigated, the model will make various simplifying assumptions. For instance, at shorter wavelengths in the visible end of the electromagnetic spectrum, at atmospheric temperatures, blackbody radiation from the earth and air molecules can be ignored, and only the scattering of solar radiation is considered. The opposite is true towards the infra-red end of the spectrum - the solar spectrum is overtaken by blackbody radiation from the earth and the atmosphere, and thus can be ignored, as can molecular scattering due to the $1/\lambda^4$ dependence of Rayleigh scattering. Very few models, at the time of writing this thesis, are capable of handling both situations.

1.4 Radiative Transfer and Spectroscopy at the University of Saskatchewan

The purpose of this thesis work was to take the existing radiative transfer code SASKTRAN, developed at the University of Saskatchewan by Bourassa et al. (2008), which accurately

models the UV-Vis end of the spectrum, and expand its capabilities to model atmospheric radiation in the infra-red, making it one of the first models of its kind. The model will be discussed in detail in later chapters, but essentially it considers every point in the atmosphere as an entity that can absorb, emit, and scatter radiation. From these points, the model traces rays in all directions, determining the attenuation of radiation as it is scattered to all other points, and dealing separately with light that has been scattered once, twice, three times, and so on. This is known as a *successive orders* model, and though it is generally a very inefficient way to calculate infra-red radiation in the atmosphere, it allows for highly accurate modelling of the radiative processes, and even allows for multiple scattering of infra-red radiation. Other methods of solving the radiative transfer equation include Monte Carlo and N-Stream Approximations.

The remainder of this thesis will delve into the topic of atmospheric spectroscopy. The composition and behaviour of the atmosphere will be covered in chapter §2, and chapters §3 and §4 cover the electromagnetic and quantum theory behind the propagation of light through air. Chapters §5 and §6 transition into the thesis work, explaining the incorporation of infra-red thermal emissions into the current SASKTRAN model, and verification of calculations made with the updated model to other radiative transfer models and satellite measurements. The work done in this thesis is summarized in chapter §5, describing the implementation of infra-red thermal emissions into the current SASKTRAN radiative transfer model. Chapter §6 transitions into the verification of radiative transfer calculations made with the modified SASKTRAN model, comparing with other radiative transfer models and satellite measurements.

Chapter 2

Earth's Atmosphere

> Air, I should explain, becomes wind when it is agitated.
>
> Lucretius

In this chapter the structure of the atmosphere will be introduced. The vertical distribution of temperature, density, and number density of trace gases will be discussed, as will the variations in these quantities in different regions of the globe. The calculation of hydrostatic balance is performed to derive the implied pressure and density profiles of the atmosphere, and is compared to observations. The radiative balance of the earth and atmosphere will be examined. The focus is then shifted towards the so-called *greenhouse gases* and their effect on the radiative balance of the atmosphere, and satellite measurements of these trace gases.

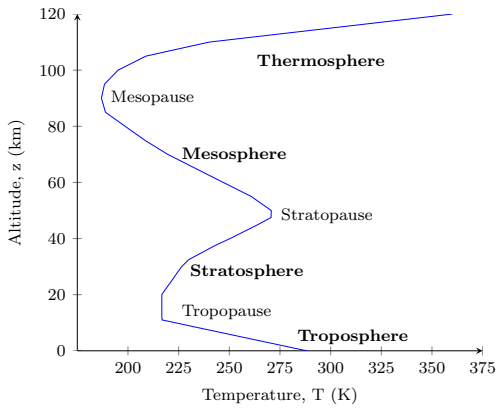

Figure 2.1: The US standard atmosphere for the vertical structure of atmospheric temperature.

2.1 Atmosphere Fundamentals

2.1.1 Vertical structure

The vertical structure of the atmosphere is ultimately determined by its vertical temperature variation. While there is a fair amount of horizontal variation in temperatures, the basic vertical structure of atmospheric temperature is qualitatively equivalent, and thus we can say there is a "typical" temperature profile for the atmosphere. The profile is not governed by any simple law, and is the result of a number of complex radiative and thermodynamic processes. As shown in figure 2.1, the temperature profile seems to have a few different "layers" with linearly decreasing/increasing temperature which have their boundaries at the temperature inversions. The "top" of the atmosphere is generally defined as roughly at 100-120 km altitude, as beyond this height the density of neutral molecules is comparable to that of charged particles, and the air can no longer be modelled as an ideal gas.

Starting at the top of the atmosphere, the first layer of air we encounter is the **thermosphere**, where the temperature is high and variable - temperatures can approach 1000 K. However, the density of air is so low at thermospheric altitudes that the notion of "temperature" starts to lose its common meaning. The region is dominated by atoms like oxygen, nitrogen, and

so on, due primarily to the top of the atmosphere receiving high-energy short-wave UV solar radiation, resulting in the dissociation of most polyatomic molecules. The resulting molecular oxygen absorbs the majority of the short-wave UV radiation, and due to the lack of infra-red active polyatomic molecules, loss of energy is weak, so the temperature of the region remains high.

The lower boundary of the thermosphere, the **mesopause**, is the upper boundary for the **mesosphere**. The temperature increases through the mesosphere as altitude decreases, until the "hot spot", the **stratopause**, is reached at roughly 50 km altitude. This peak in temperature is a result of the absorption of UV solar radiation (100 nm to 350 nm) by ozone molecules in the **stratosphere** (below the mesosphere). Interestingly enough, ozone does not peak until 20-30 km altitude, well below the temperature peak. This is because ozone is highly opaque to UV radiation, so that most of the UV is absorbed in the upper parts of the stratosphere, thus dissociating the ozone at these altitudes, depositing energy that manifests in the form of heat. The reason for the existence of ozone is that it is a by-product of *photo-dissociation* of molecular oxygen (O_2), producing atomic oxygen(O), which then combines with O_2 to produce ozone,

$$\begin{aligned} O_2 + h\nu &\rightarrow O + O, \\ O + O_2 + M &\rightarrow O_3 + M, \end{aligned} \tag{2.1}$$

where $h\nu$ is the energy of an incoming quantum of light (photon), and M is any third molecular body, necessary to carry the extra energy of the combination.

The existence of this layer to absorb UV radiation is incredibly important to life on earth, as most forms of life would perish if exposed to solar UV radiation. As the name suggests, the stratosphere is highly stratified, with long residence times for molecules. This means that particles injected into the layer, such as volcanic aerosols, can exist for months or even years in the stratosphere.

The stratosphere has a lower boundary at the **tropopause**, which marks the upper boundary of the final atmospheric layer, the **troposphere**, which exists at altitudes of 8 - 16 km, depending on latitude and time of year. From the tropopause down to the surface, temperature increases strongly. Almost all water vapour is contained in this region, as well as roughly 85% of the atmosphere's mass. The troposphere is warmed, in part, by the absorption of radiation by H_2O and CO_2, which must be in radiative equilibrium with the stratosphere. This leads to vertical profiles of CO_2 that are well-mixed, and thus follow the density of the surrounding air. Vertical profiles for water vapour are well-mixed above the tropopause, only due to the fact that nearly all atmospheric H_2O is contained in the troposphere, which is where all evaporation and condensation occurs in weather patterns.

2.1.2 Hydrostatic Balance of the Atmosphere

Assuming the atmosphere to be static and a fluid, the pressure at any height would depend on the total weight of the fluid above it. This approach to approximating the density of air is called *hydrostatic balance*. It is assumed that pressure, p, and density, ρ, are both functions of height, z, only. Imagine a cylindrical column of air as depicted in figure 2.2, whose bottom is at height z, has a height δz small enough that the density ρ can be approximated as a constant ρ(z) for the volume. The pressure at the top, p(z + δz), can be determined from the pressure at the bottom,

$$p(z + \delta z) = p(z) + \delta p, \tag{2.2}$$

$$\delta p = \frac{\partial p}{\partial z}\delta z, \tag{2.3}$$

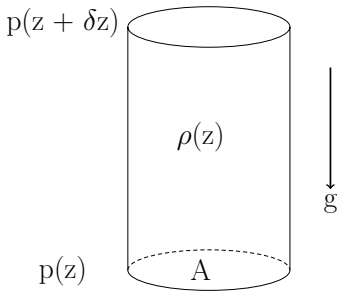

Figure 2.2: Hydrostatic balance.

where the change in pressure, δp, was assumed to vary linearly over the infinitesimal height δz. The mass of this cylinder, with cross-sectional area δA, is,

$$M = \rho\,\delta A\,\delta z. \tag{2.4}$$

Assuming the net force on the column of air to be zero, the gravitational force, $F_g = -gM = -g\,\rho\,\delta A\,\delta z$, the downward pressure force at the top, $F_T = -(p + \delta p)\,\delta A$, and the upward pressure force at the bottom, $F_B = p\,\delta A$, are summed to obtain the hydrostatic balance equation,

$$\begin{aligned} F_g + F_T + F_B &= -g\,\rho\,\delta A\,\delta z - (p + \delta p)\,\delta A + p\,\delta A = 0, \\ g\,\rho\,\delta z + \delta p &= 0, \\ \frac{\partial p}{\partial z} + g\,\rho &= 0. \end{aligned} \tag{2.5}$$

Equation 2.5 is the equation of hydrostatic balance. With the boundary condition that p $\rightarrow$ 0 as $z \rightarrow \infty$, and equation 2.5 can be integrated,

$$p(z) = -g \int_{z}^{\infty} \rho \, dz, \tag{2.6}$$

to give the pressure at any height z as a function of the mass per unit area of the atmospheric column above z. Using this, the global average pressure at sea level is p_s= g $\times$ Mass of unit area air column / surface area of earth = 1013 hPa, which is indeed the average.

To actually find the pressure as a function of height, we need to make a major assumption - that we are dealing with dry air that behaves as an ideal gas,

$$\begin{aligned} p\,V &= n\,R\,T, \\ \frac{n}{V} &= \frac{m\,/\,M}{V} = \frac{\rho}{M} = \frac{p}{R\,T}, \end{aligned} \tag{2.7}$$

where T is the temperature, V is the volume, n is the number of molecules, m is the mass, M is the molar mass, and R is the gas constant. Thus, inserting into equation 2.5,

$$\frac{\partial p}{\partial z} = -\frac{M\,g}{R\,T} p(z). \tag{2.8}$$

As we saw previously, T is not constant, but varies with height. However, as shown in figure 2.1, the temperature varies linearly (approximately) in each atmospheric layer. We define something called the local scale height,

$$H(z) = \frac{R\,T(z)}{M\,g}, \tag{2.9}$$

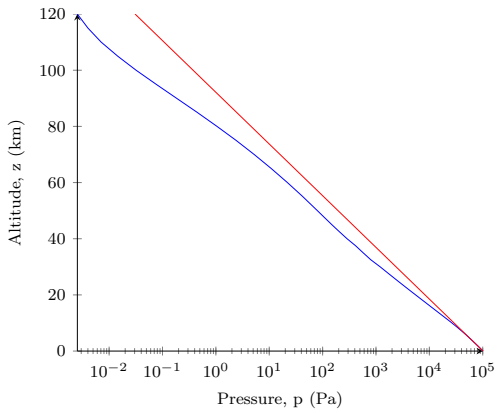

Figure 2.3: Actual pressure profile (blue) versus a pressure profile derived assuming an isothermal atmosphere (red).

such that the hydrostatic balance equation becomes,

$$\frac{\partial p}{\partial z} = -\frac{p}{H(z)}. \tag{2.10}$$

Therefore, we can solve the hydrostatic balance as,

$$p(z) = p_s \, \exp\Big(-\int_0^z \frac{dz'}{H(z')} \Big). \tag{2.11}$$

Note that if H(z) is constant (which is a decent approximation), the pressure as a function of height is just a simple exponential decay. Figure 2.3 shows the variation between the actual pressure profile and one derived assuming an isothermal (constant-temperature) atmosphere.

2.1.3 Composition

We already briefly mentioned in the previous sections some of the main components of the atmosphere, so in this section we will summarize all of them.

The air is composed mostly of molecular nitrogen (N_2), which constitutes 78.084% of all air molecules. While nitrogen has little to no absorption spectrum, it plays an important role in the radiative balance of the atmosphere from its ability to scatter radiation (in the Rayleigh regime). This effect, of course, drops off as wavelength increases. In addition, nitrogen is an essential building block for amino and nucleic acids, making it essential for life to occur on earth. Organisms use molecular nitrogen, and when they die and decompose, it is released to the atmosphere again - this is part of the *nitrogen cycle*.

The other primary component of the atmosphere is molecular oxygen (O_2), which makes up 20.946% of the atmosphere. Oxygen exhibits most of its radiative activity in the short-wavelength (high-energy) region of the spectrum, since most energy transitions that occur in oxygen are electronic. However, oxygen also exhibits a well-understood absorption at 762 nm, and another at 1.27 μm, and these regions are often used by satellites to calibrate measurements and/or determine cloud-free situations. Like nitrogen, molecular oxygen has the ability to scatter radiation. Together, they make up 99.03% of the atmosphere, and their effect of scattering radiation is the primary determining factor of radiative transfer in the UV-visible region of the spectrum.

Other main components of the atmosphere that are electromagnetically inactive are argon (Ar, 0.934% of the atmosphere), neon (Ne, 0.001818%), and helium (He, 0.0000524%). Since they play no significant role in the radiative balance of the atmosphere, they will not be discussed further.

The last components of the atmosphere are all considered trace gases, with the exception of carbon dioxide and water vapour. Carbon dioxide (CO_2) makes up roughly 0.04% of the atmosphere, and is the most closely monitored gas by the scientific community. Water vapour (H_2O), as anyone who has seen a prairie thunderstorm seemingly appear out of nowhere, is highly variable in its concentration in small regions. By mass, water vapour accounts for roughly 0.25% of the mass of the atmosphere. Methane (CH_4), accounts for 0.000179% of the atmosphere, while ozone (O_3) constitutes 0.001%, carbon monoxide (CO) 0.00001% and

nitrous oxide (N_2O) some 0.000032%. Together these gases, though constituting less than 1% of the atmosphere, are the primary determinants in the radiative balance of the atmosphere, and are known as **greenhouse gases**.

2.2 Greenhouse Gases

2.2.1 Radiative Balance - The Global Energy Budget

Radiation propagating in the atmosphere is divided into two main components: **shortwave** radiation which almost exclusively originates from the sun, and **longwave** radiation which originates from the thermal emissions of the ground and atmosphere. Analyzing the spectrum of radiation in the atmosphere, the radiation from the sun can be approximated by a blackbody emitter at roughly 5778 K, while the longwave radiation from the earth can be approximated with a 288 K blackbody (see Figure 2.4). While the solar spectrum is several orders of magnitude greater than the terrestrial spectrum, the actual radiation absorbed and scattered by the ground and atmosphere is a fraction of its full magnitude. Therefore, between 3 and 5 μm, terrestrial and solar radiation are of the same order of magnitude, and beyond 5 μm terrestrial radiation dominates. As seen in Figure 2.4, there is little overlap between the two regimes, so in attempts to model atmospheric radiation, they are almost always considered separately. With the assumption that the sun emits like a blackbody at temperature T_{sun}, it's total energy per unit area emitted follows the Stefan-Boltzmann law $\mathrm{F} = \sigma\, T_{sun}^4$, where σ is the Stefan-Boltzmann constant. The energy per unit area incident upon the sphere defined by the orbital radius of the earth is given by,

$$S_0 = \frac{\text{Flux} \times \text{Surface area of sun}}{\text{Surface area of orbital sphere}} = \frac{\sigma\, T_{sun}^4\, 4\pi\, r_{sun}^2}{4\pi\, r_{s-e}^2} \quad \left[\frac{\mathrm{W}}{\mathrm{m}^2}\right], \tag{2.12}$$

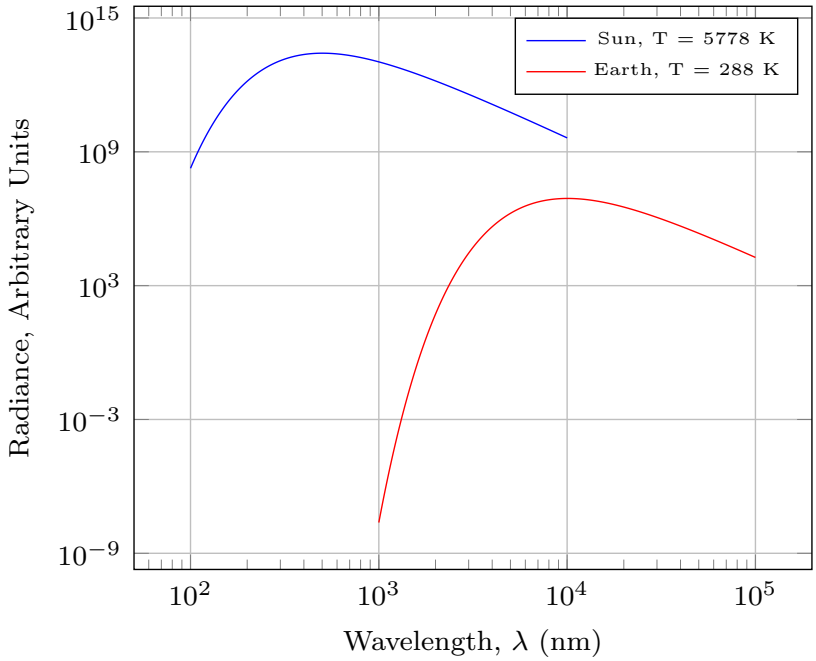

Figure 2.4: Blackbody spectra approximating the emitted radiation of the sun and the earth. Radiance in arbitrary units. Notice that there is very little overlap between the two spectra. While solar radiation is of significantly greater magnitude than terrestrial radiation, we are typically concerned with the *scattered* solar radiation, so beyond 5 μm terrestrial radiation dominates, and between 3 and 5 μm they are of the same order of magnitude.

where r_{s-e} is the distance from the sun to the earth, r_{sun} is the radius of the sun, and the temperature of the sun is taken to be 6000 K. This yields the solar constant, S_0, of 1368 W/m^2 - a measure of the average power flux density originating from the sun occurring at the top of the earth's atmosphere. Assuming that a certain percentage, A (the **albedo**), of the solar radiation is reflected back out to space, and that the solar radiation incident on the earth covers the area of a circle defined by the earth's radius, r_e, the total energy, E_{in}, input to the earth is,

$$E_{in} = S_0 \, \pi \, r_e^2 \, (1 - A) \tag{2.13}$$

The energy emitted by the earth has to balance this incoming energy. Assuming the earth as a perfect blackbody, the total energy emitted by the earth equates with the solar energy,

$$\begin{aligned} E_{in} &= E_{out}, \\ S_0 \, \pi \, r_e^2 \, (1 - A) &= 4 \, \pi \, r_e^2 \, \sigma \, T_{earth}^4, \\ T_{earth} &= \left[\frac{S_0 \, (1 - A)}{4\sigma} \right]^{1/4}. \end{aligned} \tag{2.14}$$

Assuming an albedo A = 0.32 – which is approximately the global average – the temperature of the earth is approximated to 255 K. This is 20-30 K cooler than actual average temperatures on earth. A better model of the radiation balance is obtained by taking into account the absorbing and emitting properties of the atmosphere, which were ignored in the previous derivation. While solar radiation is moderately scattered and weakly absorbed by the atmosphere, infrared radiation emitted by the earth (and atmosphere) is strongly absorbed by the greenhouse gases. A decent approximation is to assume the atmosphere as a single block between space and the earth's surface capable of emitting and absorbing radiation (see Figure 2.5) - the bulk radiative transfer model of the atmosphere. In this model we consider the solar flux in the UV-Vis and the flux in the IR separately. The atmospheric bulk has a temperature T_a, solar absorption f, and **emissivity** ϵ - which is a ratio of how well a real material emits relative to an ideal blackbody. The flux at the top of the atmosphere is found by,

$$\begin{aligned} S_0 \, \pi \, r_e^2 \, (1 - A) &= 4 \, \pi \, r_e^2 \, \times \text{flux}, \\ \text{flux} &= \frac{1 - A}{4} S_0. \end{aligned} \tag{2.15}$$

Since the atmosphere absorbs f of the solar radiation, the solar flux reaching the ground is,

$$\text{Solar flux at ground} = (1 - f) \frac{(1 - A) \, S_0}{4}. \tag{2.16}$$

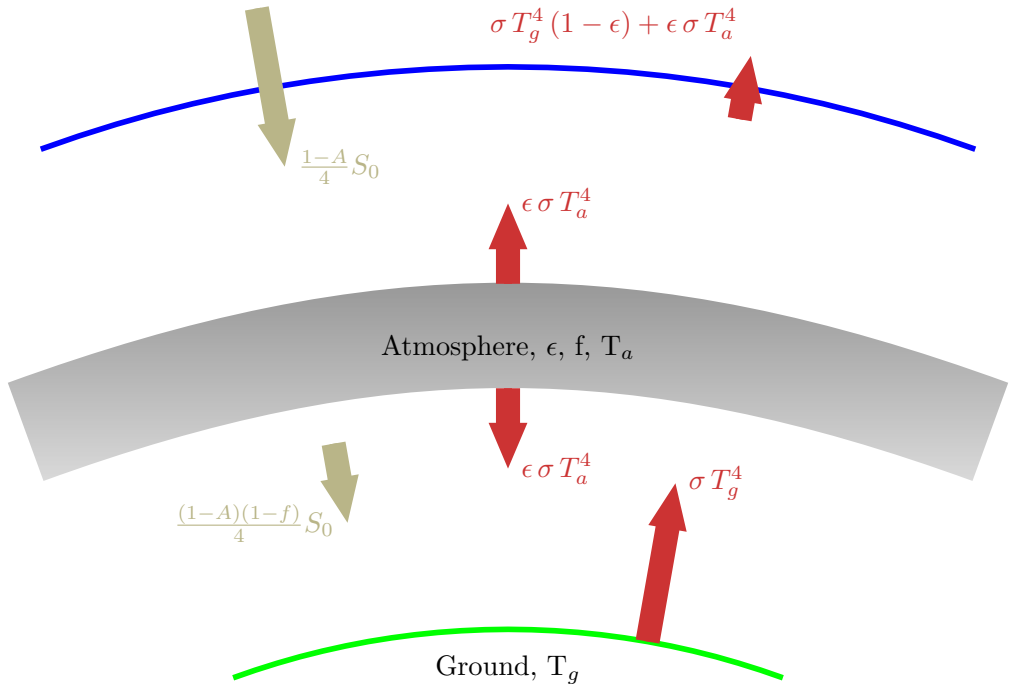

Figure 2.5: The bulk radiative transfer model of the atmosphere. Yellow arrows are short wave (solar) radiation, and red arrows are long wave (thermal) radiation. The albedo, A, is the amount of solar radiation reflected back to space by the atmosphere. The atmosphere absorbs f percentage of short waves, and ϵ percentage of long waves.

The radiation flux both upward and downward is given by $\epsilon\sigma\, T_a^4$, and the ground emits upward flux of $\sigma\, T_g^4$. Lastly, infra-red radiation passing through the atmosphere from the ground is absorbed by the factor $1-\epsilon$. Balancing the fluxes at the top of the atmosphere and the ground, we can obtain the ground temperature,

$$\text{Top}: (1-\epsilon)\,\sigma\, T_g^4 + \epsilon\,\sigma\, T_a^4 = \frac{1-A}{4}\, S_0,$$

$$\text{Bottom}: \sigma\, T_g^4 = (1-f)\frac{1-A}{4}\, S_0 + \epsilon\,\sigma\, T_a^4,$$

$$T_g = \left[\frac{(2-f)(1-A)\, S_0}{(2-\epsilon)\, 4\,\sigma}\right]^{1/4}. \tag{2.17}$$

Using average values for albedo and atmospheric emissivity, we obtain a much better approximation of 288 K. The idea of the atmosphere as a "blanket" for the earth is known as the **greenhouse effect**. With more layers added to the atmosphere, this model can increase in accuracy. As shown in Figure 2.6, numerous factors work into the overall balance of radiation in the atmosphere. All processes involving clouds and transport of heat, aside from electromagnetic processes, play a critical role in the earth's energy budget. By far the most important factor in the overall balance of radiation is the **atmospheric window** - an optically thin region of the electromagnetic spectrum from 7.5 μm to 14 μm that allows a large flux of infrared radiation to escape the earth to space without being absorbed and re-emitted. What makes this region extra important is that it also contains the peak of the earth's blackbody spectrum at roughly 10 μm, so any additional absorption in this region would greatly increase the ground temperature. This does not mean gases do not absorb in this region - CO_2, H_2O, and O_3 all have weak absorption features in this window. Since their relative populations are small enough in the atmosphere, their effect on the flux is small. An increase in their molecular concentrations would greatly affect the radiation balance, leading to the increase of strict regulations on "greenhouse emissions" for industrialized countries.

Flux estimates over the entire UV-Vis-IR band give a good idea of the greenhouse effect,

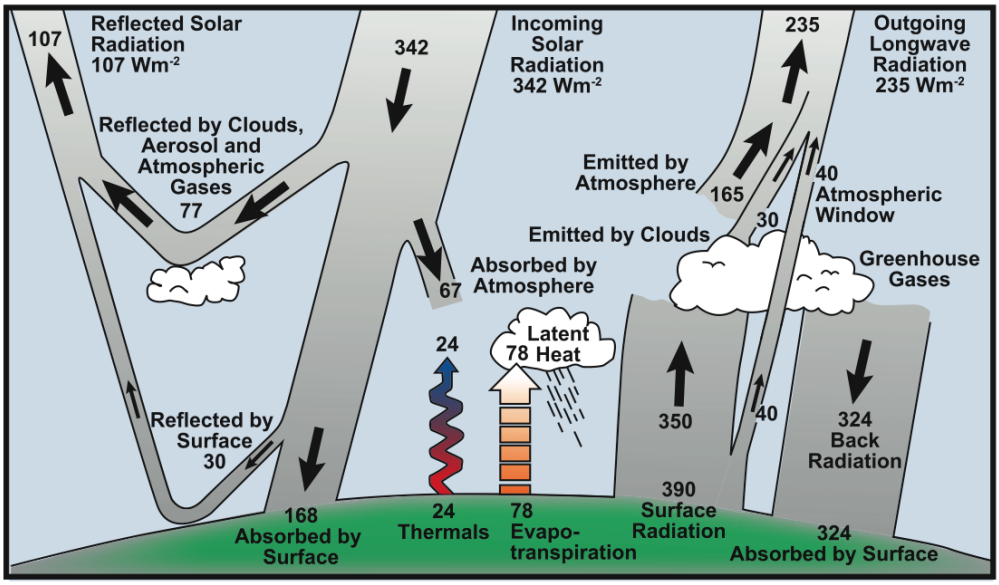

Figure 2.6: Earth's energy budget, taking into account all major contributors. (Kiehl and Trenberth, 1997)

but one must examine the absorption properties and atmospheric chemistry of each of these greenhouse gases to obtain an understanding of the underlying processes (as we have already done to some extent).

Electromagnetic radiation incident upon a molecule will cause the molecular bonds to vibrate if the frequency of the radiation is close to the resonance frequency (frequencies) of the molecule, changing the vibrational energy. This is analogous to the classical harmonic oscillator subject to an external driving frequency. If there is a dipole moment in the molecule, the oscillating electric field of the incident radiation will cause a change in the rotational energy of the molecule. If the energy of the radiation is high enough (high frequency), it can also induce a transition of the molecule's electron's from one energy state to another. However, since this work focuses on visible-IR spectrum radiation, and electronic transitions almost exclusively occur in the short-UV range, they will be ignored.

To characterize the spectral properties of each molecule in the following sections, *transmission spectrums* were computed using LBLRTM (Clough et al., 2005) for each molecule. A

transmission spectram is a convenient way to represent the ability of radiation to propagate through a given material. It characterizes the percentage of radiation at the end of a path after being absorbed and scattered by the material contained within the path, at a given wavelength/frequency. A transmission of 1.0 means that no radiation was scattered/absorbed by the path, and 0.0 means that no radiation reached the end of the path, due to scattering/absorption. The following sections will discuss the spectral properties of water vapour, carbon dioxide, methane, ozone, and carbon monoxide in the infra-red, and their origin and distribution within the atmosphere.

2.2.2 Water Vapour (H_2O)

Water vapour is often deemed "the most important greenhouse gas," primarily due to its abundance in the atmosphere (80% of all greenhouse gases by mass), and its strong absorption features in longwave thermal radiation. Simple radiative-convective models implemented by (Ramanathan and J.A. Coakley, 1978) and (Schmidt et al., 2010) show that water vapour accounts for between 36% and 66% of the greenhouse effect, and when combined with clouds those numbers jump to 66% and 85%. However, due to its relatively short residence time in the atmosphere (on the order of 10 days), and its high regional and temporal variability, it is often not considered in climate models as a greenhouse gas. Evaporation, condensation, sublimation, and precipitation of water accounts for this high variability. Rather, water vapour is considered to be more of a *feedback mechanism* to the greenhouse effect. Essentially, the warmer the earth and atmosphere become, the more water vapour becomes evaporated into the atmosphere. With increased water vapour content, more radiation is absorbed, and thus the warmer the earth and atmosphere become. This is obviously a positive feedback, and scientists are concerned that if the earth warms to a certain point, it will create a *runaway greenhouse effect*.

Spectral Properties

Due to its bent molecular shape, H_2O exhibits a small dipole moment, making it highly active to infra-red radiation. In the near and mid infra-red, water vapour undergoes a combination of vibrational and rotational transitions from absorbed radiation. Approaching long infra-red (thermal) radiation, absorption of radiation is almost exclusively due to rotational transitions. The transmission spectrum for a typical profile of atmospheric water vapour is shown in Figure 2.7.

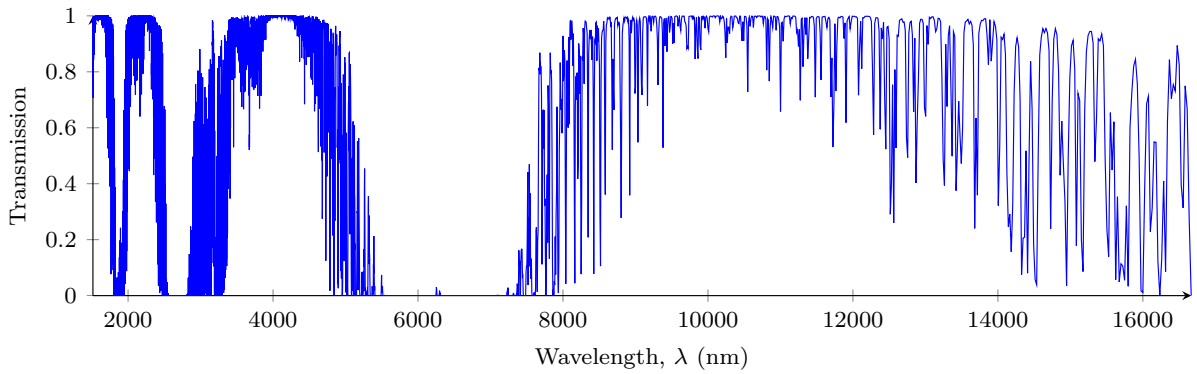

Figure 2.7: Transmission (1 - absorption) spectrum of water vapour in the infra-red. Results calculated from LBLRTM (Clough et al., 2005)

Climatology

Water is evaporated from the earth's surface to the air; once there, the average water molecule spends 9 days in the air before returning to the surface. Due to this rapid turnover, and varying geography, atmospheric water vapour is highly variable regionally and temporally. In general, more water vapour is contained at the equator than the poles, since warm air has a higher capacity to hold moisture - see Figure 2.8. As well, roughly 50% of atmospheric water vapour is contained below a height of 1.5 km, and rapidly decreases with increasing height. Very similarly, the *concentration* of water vapour decreases with increasing height -

i.e. the air becomes drier (see Figure 2.9). Still, numerous attempts have been made to find a "typical" distribution of water vapour in the atmosphere.

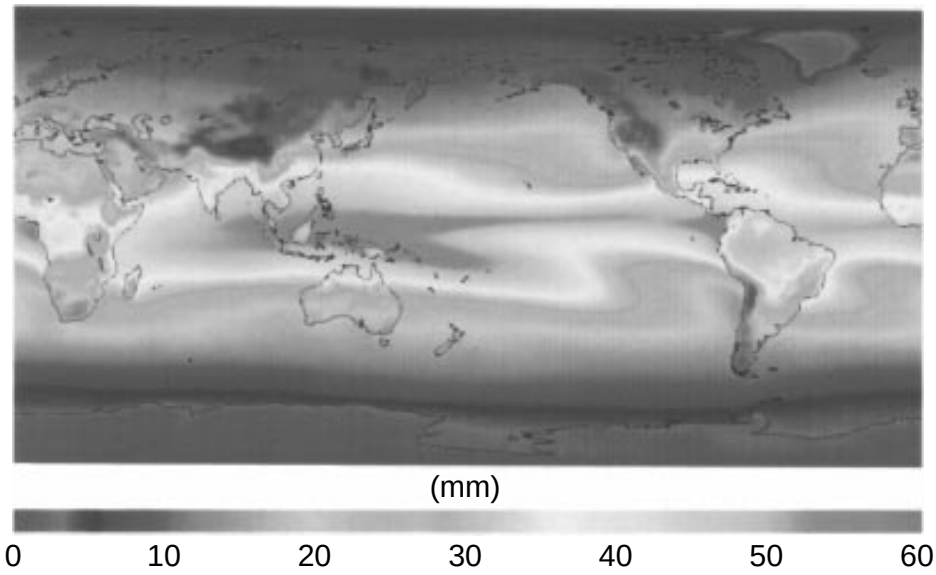

Figure 2.8: Global distribution of precipitable water vapour (in mm) above the earth's surface. Data is taken from both satellite and weather balloon observations and is an average from 1988 - 1997 (Seidel, 2002)

The vertical distribution of water vapour is largely determined by the Clausius-Clapeyron relation (see equation 2.18), which basically states that water vapour content decays rapidly with decreasing temperature. The equation describes the relation of the pressure and temperature of a substance undergoing a phase transition,

$$\frac{de_s}{dT} = \frac{L_v(T)\, e_s}{R_v\, T^2}, \tag{2.18}$$

where L_v is the specific latent heat of evaporation, e_s is the saturation vapour pressure and R_v is the water vapour gas constant. The saturation vapour pressure is a measure of the maximum quantity of water vapour air can "hold" at a given temperature - the hotter the air, the greater capacity to store water vapour.

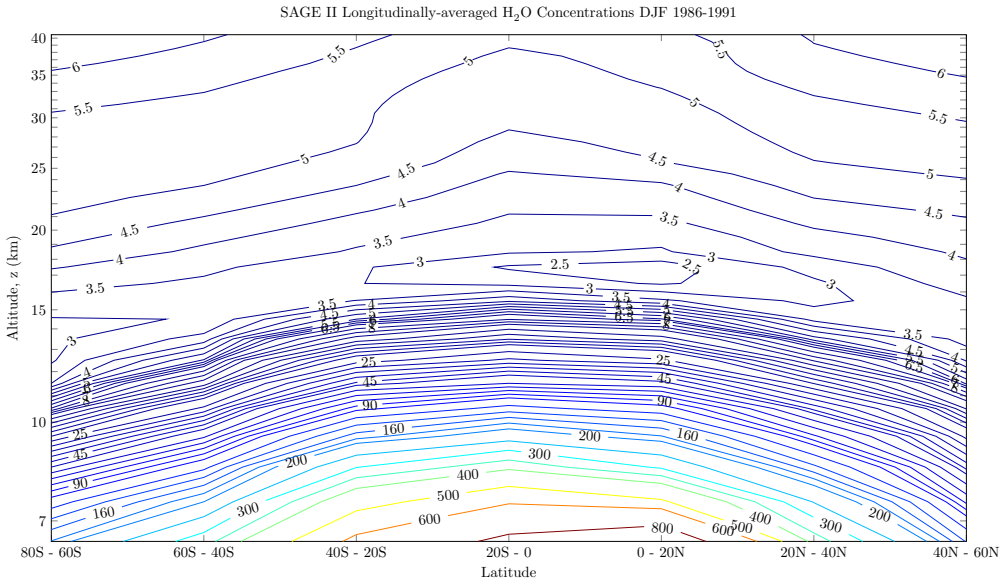

Figure 2.9: Vertical distribution of water vapour in PPMV concentration as determined by longitudinal averages from SAGE II, average for December-January-February of 1986-1991. Note the logarithmic height axis, and minimum height of 6.5 km.

Due to the temperature inversion at the tropopause, water vapour is essentially "contained" in the troposphere, with very little escaping into the stratosphere and beyond, leading to the profiles shown in Figure 2.9 - almost all water is contained below 5 km altitude. Based on a five year study of SAGE II measurements, Chiou et al. (1997) discovered three key identifiers of water vapour distribution in the atmosphere: i) A region of minimum water vapour density ("hygropause") occurred in all latitude bands; ii) distance between the tropopause and hygropause varies between 1 km at low latitudes to 4 km at high latitudes; and iii) a positive poleward gradient throughout all seasons exists for altitudes between 20 km and 40 km - i.e. as you move away from the equator, the air gets progressively less humid.

2.2.3 Carbon Dioxide (CO_2)

Among the general public, this is the most well-known of the greenhouse gases. It was the first of the infra-red active molecules to be closely monitored, beginning in 1956 with the

research of Dave Keeling on Mauna Loa, Hawaii (Harris, 2010b). His observations provided one of the most thorough time-series measurements of atmospheric CO_2 in the scientific community. His measurements showed an annual oscillation in the CO_2, and in addition showed a steady increase year after year. Figure 2.10 shows the Mauna Loa measurements from 1956 to present. The Keeling measurement series was the launch pad for numerous

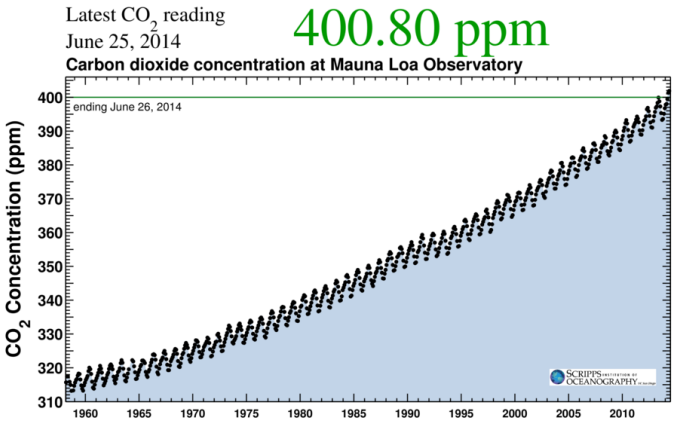

Figure 2.10: Carbon dioxide concentrations at Mauna Loa observatory (Monroe, 2014)

scientific endeavours to further investigate the concentration of atmospheric CO_2 - numerous satellites are devoted primarily to the retrieval of CO_2 on a global scale. Most prominent among these are OCO-2 (Osterman et al., 2014), GOSAT (Kuze et al., 2009), IASI (Chalon et al., 2001), and AIRS (Kempler, 2002).

Spectral Properties

The transmission spectrum of CO_2 is shown in Figure 2.11. Like H_2O, CO_2 is a triatomic molecule, so it has similar modes of vibration. However, instead of being bent, it is linear, which means it exhibits no permanent dipole, making CO_2 far less active in the infra-red than H_2O. Thus most electromagnetic activity is due to vibrational transitions within the molecule. However, one vibrational mode of CO_2 "bends" the molecule, inducing a transient dipole, allowing the molecule to make rotational energy transitions, although not near as

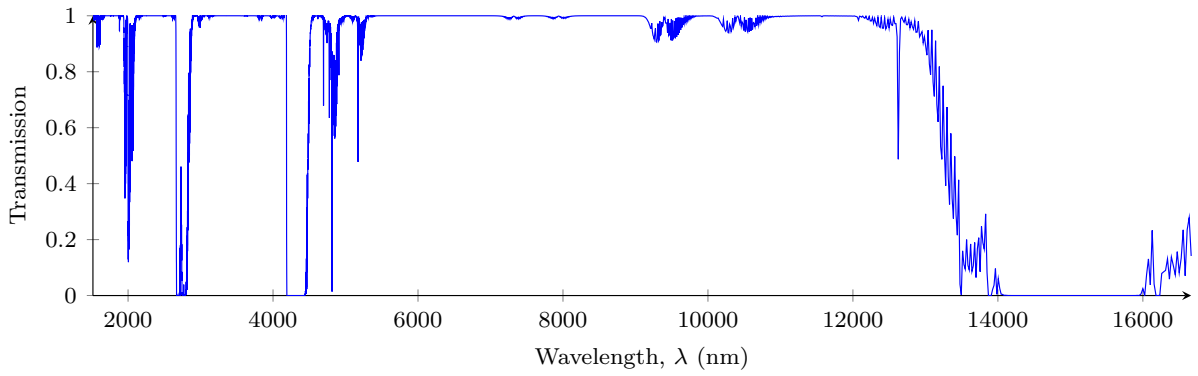

Figure 2.11: Transmission spectrum for an atmosphere of CO_2, calculated using LBLRTM (Clough et al., 2005).

drastic as occurs in H_2O. These vibrational-rotational transitions occur most prominently around the 15 μm vibrational bending mode, spanning 12-18 μm. The absorption feature centred at 15 μm (see Figure 2.11) of CO_2 arguably has the most significant effect on the earth's radiation budget of all greenhouse gases (i.e. excluding H_2O), since it lies close to the peak of the earth's blackbody spectrum. However, absorption features in the near infra-red (NIR) play a role in atmospheric heating. In the 60-85 km region of the atmosphere, NIR bands of CO_2 strongly affect the thermal budget of the mesosphere. This is partly due to the local minimum of O_3. Despite this, preliminary models that have modelled NIR bands do not respond significantly to even a *doubling* of CO_2 - i.e. the radiative forcing due to CO_2 in the NIR is not strong enough to have an "overall effect" (Fomichev et al., 2004; Schmidt et al., 2010).

Climatology

The average CO_2 concentration at present can range from 370 - 400 ppmv, depending on the region examined. This has increased steadily from the pre-industrial levels of roughly 280 ppmv. It is the general consensus in the scientific community that the source of this increase is entirely anthropogenic (Bernstein et al., 2007).

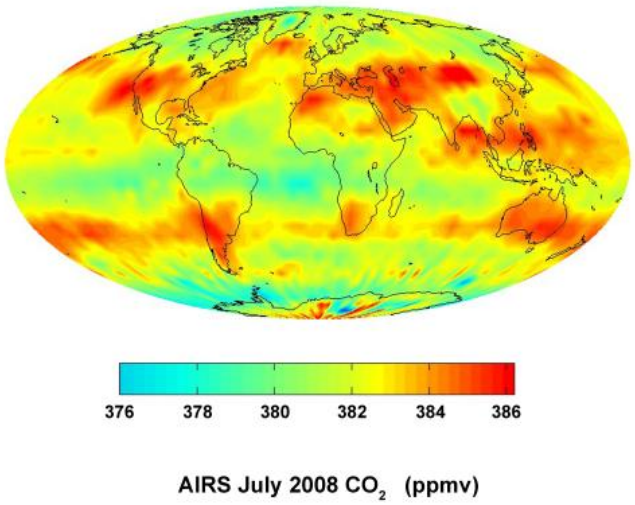

Figure 2.12: Global variation of total column CO_2 for July 2008 (Buis, 2008).

In general, concentrations of CO_2 are higher in northern latitudes than southern latitudes. This is due to the larger percentage of land mass, and larger distribution of vegetation. Most notably, the boreal forest dominates a huge portion of the northern hemisphere, and is active in respiration during summer months, but lies dormant in winter months due to its extreme latitude. This causes a "build-up" of CO_2 during these months, while the forests of the South America, Africa, and Asia remain active in respiration throughout the year, due to their proximity to the equator. This is the primary reason for the annual oscillation of CO_2 concentration seen in the Keeling curve. Globally, the oceans act as a net sink of CO_2. High latitudes absorb more, while low latitude ocean regions release a significant amount of CO_2. This can all be encompassed in terms of the *global carbon cycle* (Pak, 2010). Since CO_2 is fairly chemically inert, it has a long life time in the atmosphere, and thus is well mixed, following a similar density profile as the atmospheric pressure. Therefore, the regional variation observed is due to transport processes, such as heating cells, wind, etc., and to regional anthropogenic activity. Due to being well-mixed, it is common for measurements to make a *total column* measurement - considering the quantity of CO_2 in a given vertical column of air with unit cross-sectional area, and dividing by the total amount of air in that

column. This gives relative measurements of concentration, such as ppmv, ppbv, or g/kg. The process of determining atmospheric characteristics of a given molecule from measurements is referred to generally as a **retrieval** – the retrieval of density data from measurements would be a *density retrieval* – and is generally a complex process. For instance, the method (*very* briefly) used at the University of Saskatchewan involves assuming an initial density profile for a given molecule (such as O_3), running the SASKTRAN model, comparing the computed spectrum at a few key wavelengths with radiance measurements, adjusting the density profile, and repeating until the computed values approach the measurement values within a certain tolerance.

The majority of CO_2 measurements are derived from absorption bands in the far infra-red (FIR), where CO_2 has its strongest absorption band. However, the difficulty with using these measurements for density retrievals is that a temperature contrast between the ground and atmosphere is *necessary*, as CO_2 becomes very optically thick to radiation in these wavelengths at roughly 2 km altitude. Therefore instruments have difficulty distinguishing between radiation emitted from the dense atmospheric CO_2 at this altitude and the ground radiation (Christi and Stephens, 2004). Near and mid infra-red (NIR and MIR) measurements, once avoided due to the difficulty of the retrieval calculations and low signal-to-noise in detectors, are becoming more popular for the ability to distinguish ground radiation in the measurement. This is the main reason we are pursuing further development of the SASKTRAN model.

2.2.4 Methane (CH_4)

Spectral Properties

The transmission spectrum for methane is shown in Figure 2.13. Methane has a higher capacity to absorb infra-red radiation than other common atmospheric species, owing to its

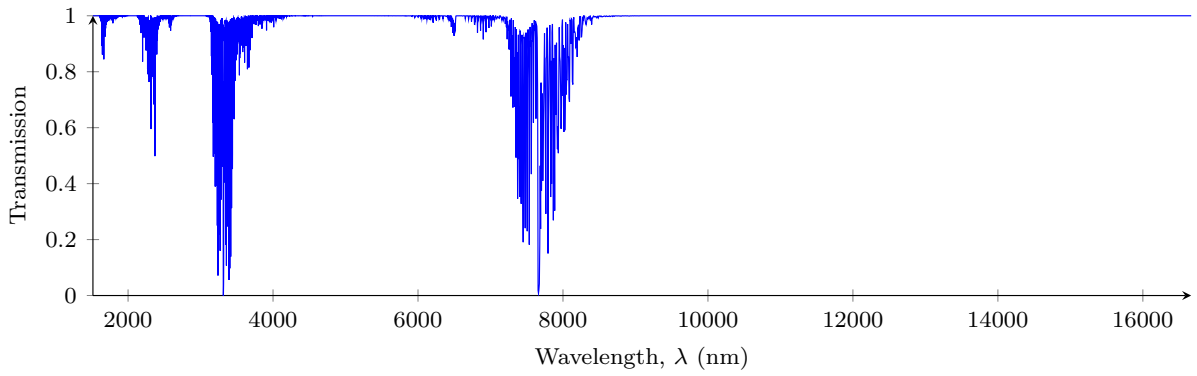

Figure 2.13: Transmission spectrum for atmospheric methane, calculated with LBLRTM (Clough et al., 2005).

larger size. Since it preferentially absorbs longwave radiation much more readily than other molecules, its concentrations in the atmosphere play a significant role in the global radiative balance. Methane's absorption bands, alongside nitrous oxide, dominate the regions between the primary CO_2 and H_2O bands. While CO_2 and H_2O have three vibrational modes, CH_4 has four separate vibrational modes, but due to symmetry in the molecule, only two of them interact with infra-red radiation. Just like CO_2, when CH_4 bends it gains a transient dipole, and thus can also change rotational energy in the presence of electromagnetic radiation. The effect is lessened with CH_4 since it has more symmetry than CO_2.

Climatology

Like CO_2, methane is well-mixed in the atmosphere, and thus most attention is devoted to total column amounts of CH_4 rather than the vertical distribution. Methane concentrations have risen from 700 ppbv in pre-industrial times up to nearly 1800 ppbv in the present. So while methane is naturally occurring - main natural sources include termites, methane hydrates, the ocean, and wetlands - most atmospheric methane is anthropogenic in nature (see table 2.1). The methane resulting from large-scale livestock farms (listed as "ruminants" in the table 2.1), especially cows, is one of the biggest contributors to atmospheric methane,

and is considered anthropogenic as the vast number of livestock in the world is maintained solely through the efforts of large-scale agriculture.

Source	**Mt/yr**
Wetlands	92 - 237
Termites	20
Ocean	10 - 15
Hydrates	5 - 10
Energy Industry	75 - 110
Landfills	35 - 73
Ruminants	80 - 115
Waste Treatment	14 - 25
Rice Agriculture	53 - 100
Biomass	23 - 55

Table 2.1: Various natural and anthropogenic sources of atmospheric methane. Variation in values are the result of different academic studies (Jardine et al., 2004).

Overall, the production of methane seems to closely coincide with the rise in population of the earth, due to an increase in livestock and human waste. The biggest concern for most climate scientists is that nearly 3000 times the atmospheric content of methane is "locked up" in hydrate form - primarily in ocean floor sediments and Arctic permafrost. With global temperatures already on the rise, and the increased melting of ice, this could create a catastrophic release of methane, accelerating global warming even further than the upper 5.8^{o}C estimate by the IPCC (Jardine et al., 2004). Methane sinks include tropospheric oxidation (by the free radical OH), stratospheric oxidation (by OH and Cl radicals, and oxygen atoms), and uptake by soils (Jardine et al., 2004).

2.2.5 Ozone (O_3)

Ozone (O_3) is the only greenhouse gas that has a significant presence above the troposphere. While other molecules decrease with increasing altitude, ozone actually peaks in density in the stratosphere, in what is known to the public as "the ozone layer." Most people know that the ozone layer is what protects life on earth from high-energy ultraviolet radiation from the sun. However, ozone doesn't always have a positive effect on our lives - it depends highly upon what altitude it is located. For instance, when ozone is at above-normal concentrations in the lower troposphere, it will produce smog, harmful to human health. Ozone in the middle troposphere is beneficial as it undergoes chemical reactions which help to destroy pollutants. Due to its absorption properties, above-normal concentrations of ozone in the upper troposphere absorb up-welling infra-red radiation from the earth and re-emit it back into the troposphere, thus greatly contributing to global warming.

Spectral Properties

The transmission spectrum for ozone is shown in Figure 2.14. Ozone is highly opaque to ultraviolet radiation, responsible for absorbing most of the solar radiation from 200 to 350 nm - this is known as the *Hartly-Huggins* band. Absorption of visible light from 500 - 700 nm by ozone is part of the *Chappuis* band. Absorption at these wavelengths is due mostly to electronic energy transitions. The absorption of UV light by ozone in the stratosphere is the primary cause of the observed temperature inversion. Absorbed UV light is redistributed as heat to the surrounding atmosphere, either through emission of infra-red radiation or collisions with adjacent molecules. Like water vapour, ozone forms a bent triatomic molecule, and thus has a net dipole moment, also making it active in the far infra-red, though not nearly as active as water vapour. The main infra-red absorption features for ozone are centred at 4.75 μm, 9.6 μm, and 14.3 μm, with the strongest absorption at 9.6 μm. Being that the latter two bands fall close to the peak of the earth's blackbody radiation, concentrations of

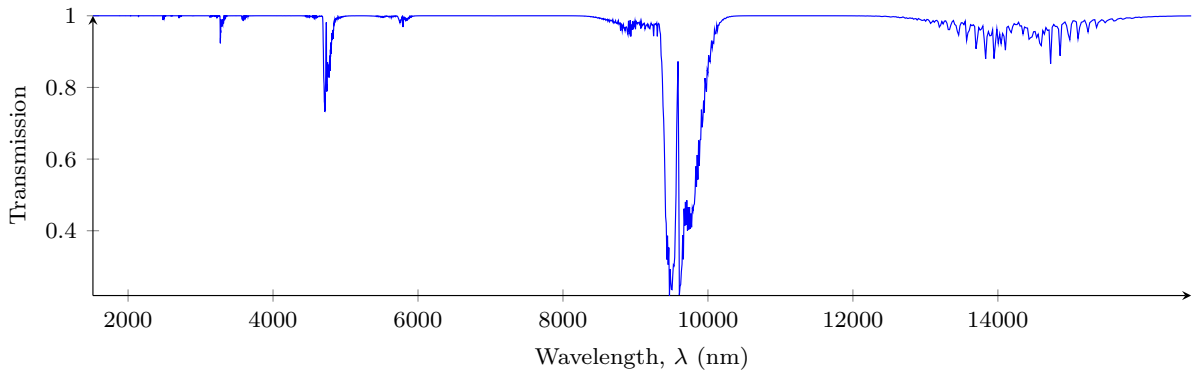

Figure 2.14: Transmission spectrum for atmospheric concentrations of ozone, calculated using LBLRTM (Clough et al., 2005).

ozone (especially upper-tropospheric ozone) play a vital role in the radiative balance of the atmosphere. Ozone is especially effective as an infra-red absorber in the troposphere, since its absorption lines will undergo significant pressure broadening.

Climatology

The majority of ozone is located above the troposphere, with a peak in the stratosphere between 20 and 30 km altitude, varying regionally. The production of ozone is a photochemical process (see Figure 2.1), which gives a vertical distribution which can be approximated by the Chapman function (see §A). A typical vertical distribution of ozone is shown in Figure 2.15). Additional tropospheric ozone forms when NO_x, CO, and other "volatile organic compounds" react in the presence of sunlight; these molecules are known as *ozone precursors*. Below is the set of reactions which produce ozone from carbon monoxide and hydroxyl (·HO

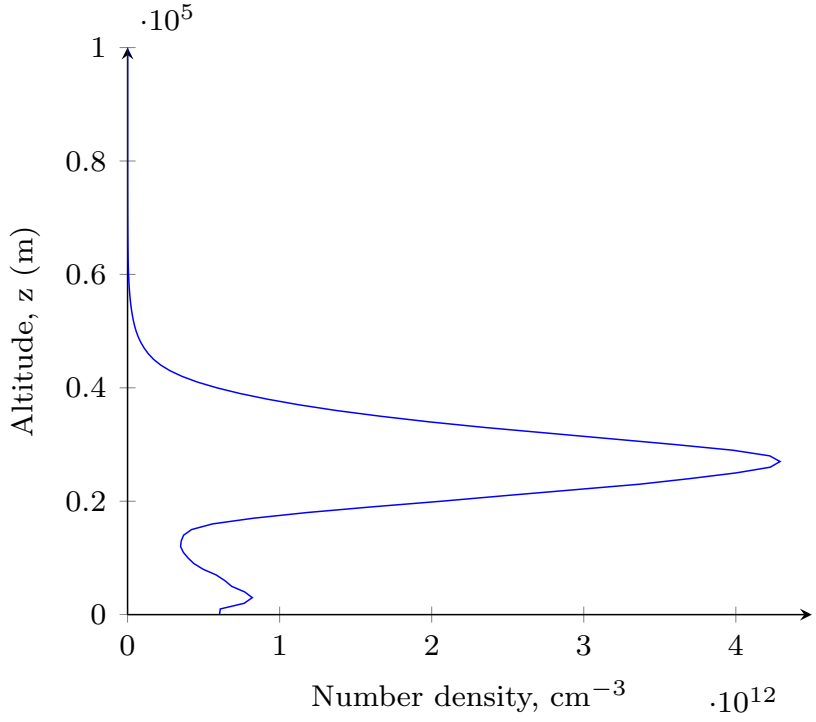

Figure 2.15: Typical vertical distribution of atmospheric ozone.

- the dot denotes a radical),

$$\begin{aligned} \cdot HO + CO &\rightarrow \cdot HOCO, \\ \cdot HOCO + O_2 &\rightarrow CO_2 + \cdot HO_2, \\ \cdot HO_2 + NO &\rightarrow NO_2 + \cdot HO, \\ NO_2 + h\nu &\rightarrow NO + O(^3P), \\ O(^3P) + O_2 &\rightarrow O_3, \end{aligned} \tag{2.19}$$

Total :

$$CO + 2O_2 + h\nu \rightarrow CO_2 + O_3. \tag{2.20}$$

It is also possible for stratospheric ozone to be transported down to the troposphere. The lifetime of tropospheric ozone is on the order of weeks to months, so once it is formed there, it can be globally transported, and homogeneity of tropospheric ozone across geographi-

cal regions can be achieved. When carbon monoxide is lofted into the troposphere, ozone precursors experience longer lifetimes and middle and upper troposphere ozone increases in concentration.

2.2.6 Nitrous Oxide (N_2O)

Nitrous oxide, or N_2O, is known better as laughing gas. It is also used as an oxidizer in rocketry and propellant to increase power output of engines in motor racing (commonly known as "nitrous"). While produced in large scales artificially, it is a naturally occurring molecule in the atmosphere, and is the main naturally occurring regulator of stratospheric ozone. While it is less abundant than carbon dioxide, it has much greater potential for warming.

Spectral Properties

The transmission spectrum for nitrous dioxide is shown in Figure 2.16. Like carbon dioxide, nitrous oxide is a linear triatomic molecule. Oddly enough, the oxygen atom is not the centre of the three atoms, one of the nitrogen atoms is the centre. Due to this, there is no "symmetric stretching" mode for the vibrational states. It has two asymmetric stretching modes at roughly 4 μm and 8 μm. The 4 μm mode is mostly due to the N-N bond vibrating, while the 8 μm mode is mostly from N-O stretching - the wavelength difference in the two absorption bands is a direct consequence of the energy present in both bonds. A further bending vibration mode exists at 17 μm, and exhibits some rotational fine structure. The IPCC defines the quantity *Global Warming Potential* (GWP), an empirical ratio taking into account a molecule's atmospheric lifetime and absorption properties to define its ability to warm the atmosphere as compared to a reference molecule (Bernstein et al., 2007). Depending on the time span of interest, nitrous oxide has a GWP 268-298 times that of carbon dioxide.

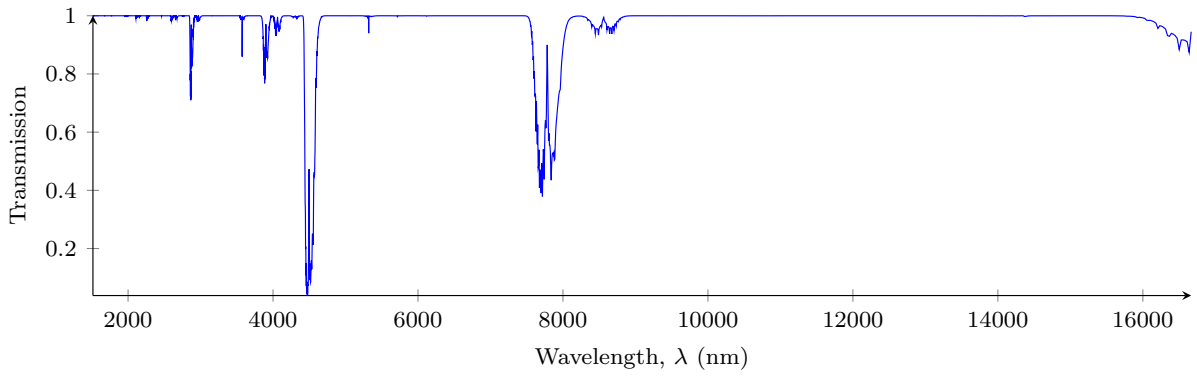

Figure 2.16: Transmission spectrum for nitrous oxide.

Climatology

Nitrous oxide is produced naturally in the soil during microbial processes, as part of the natural nitrogen cycle. From anthropogenic sources, its largest contributor is from agricultural soils, though it also arises in the production of nitric acid and synthetic fibres. Nitrous oxide has an especially long atmospheric lifetime, staying in the air for an average of 120 years before being removed by a sink or through chemical reactions. Because of its extended lifetime, it is well mixed in the atmosphere, both vertically and horizontally, and thus global variation is ignored and total column measurements represent the entire atmosphere. At present, total column amounts of nitrous oxide average around 319 ppbv, which have increased from pre-industrial era levels of 270 ppbv.

2.2.7 The Overall Effect

The IPCC, as the leading authority on climate change, has concluded that the warming trend we have seen over the past few centuries (since formal measurements of atmospheric temperatures began) are due to the observed increase in greenhouse gases of anthropogenic origin (Bernstein et al., 2007). Figure 2.18 summarizes all natural and anthropogenic sources of radiative forcing in 2005 compared with their 1750 values.

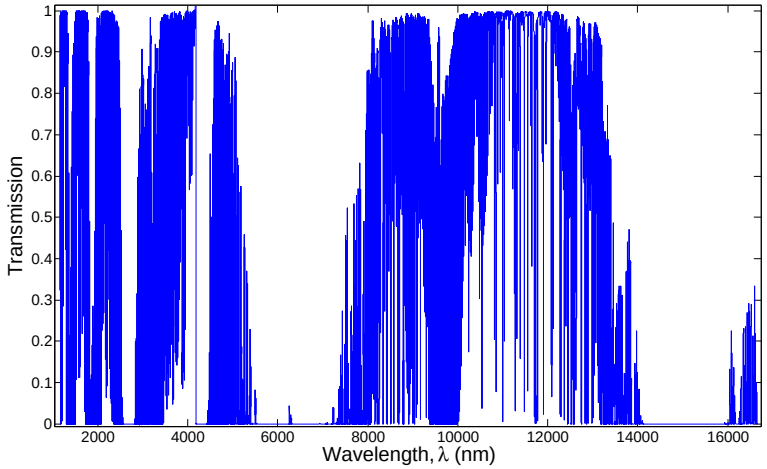

Figure 2.17: Transmission spectrum for the earth's atmosphere.

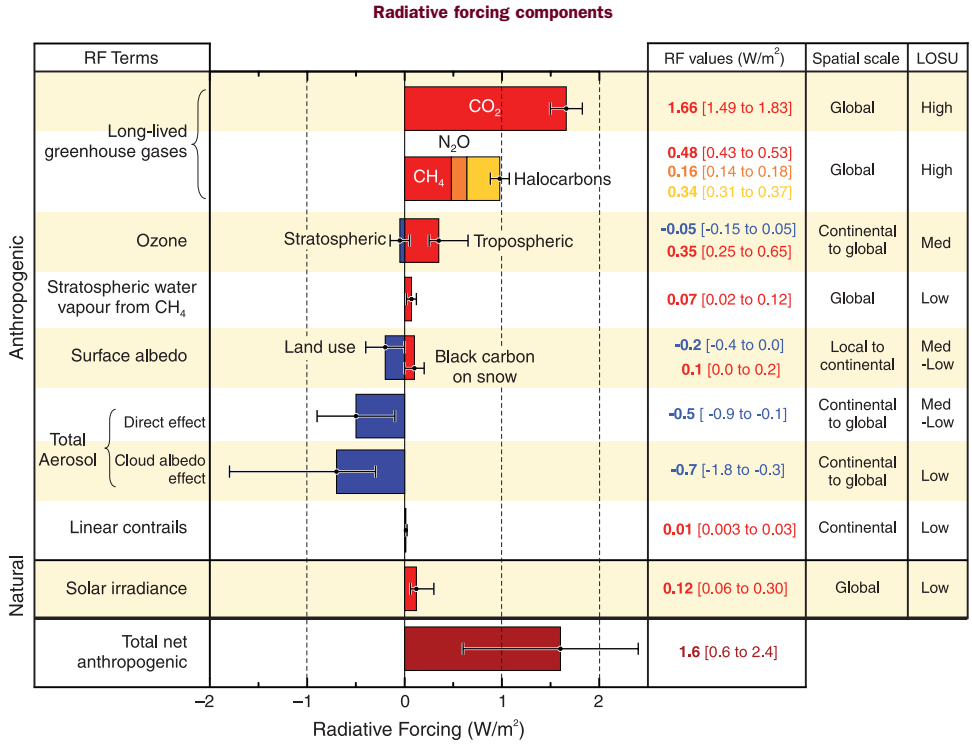

Figure 2.18: Average global radiative forcing for 2005 with respect to values from 1750 (Bernstein et al., 2007).

One important factor that has not been mentioned thus far is the effect of chlorofluorocarbons (CFC) on the radiative balance. CFC's are anthropogenic in origin, and due to their role in ozone depletion, are still in the process of being phased out from the manufacturing industry via the Montreal Protocol (Vaara, 2003). In climate models, increasing the concentration of CFC-11 and CFC-12 from 0 to 1 ppbv leads to a 0.13 K and 0.15 K increase in surface temperature (Ramanathan, 1998). Comparatively, one molecule of CFC-11 or CFC-12 has roughly the same warming effect as 10 000 carbon dioxide molecules. The reason for this lies in CFC-11 and CFC-12 absorbing strongly in the 7-13 μm atmospheric window, and since concentrations are low at present, their greenhouse effect increases linearly with their concentrations (Ramanathan, 1998).

2.3 Infra-red Measurements of the Atmosphere

There are three main platforms for infra-red measurements of the atmosphere - ground, balloon, and satellite.

Ground-based measurements are limited to the near infra-red where direct solar radiation dominates and scattering and thermal radiation can be neglected, and the far infra-red where the radiative emissions from the atmosphere are significant enough to be detected. They are advantageous in that they provide a very accurate measurement for a long time series of the same location. Limited coverage is also a ground-based instrument's downfall. To get a rough idea of the global distribution of, say, carbon dioxide, it is necessary to build several ground-based stations worldwide; such is the case of the Total Carbon Column Observing Network (TCCON) (Toon et al., 2009). Due to its strategic network of ground-based Fourier transform spectrometers (FTS), it serves as validation for satellite-based measurements of CO_2 that coincide with station locations.

Balloon instruments provide a few advantages over ground-based instruments, while still

retaining the asset of local accuracy. Balloon instruments provide a great validation of the height distribution of molecular species, which is otherwise a challenging task to retrieve from ground-based measurements. In addition, knowledge of a larger swath of geographical area is obtained, as balloon instruments tend to view in the **limb** of the earth - i.e. tangent to the earth's surface. Balloons are obviously limited by the altitude which they can achieve, thus their measurements typically only extend to 40 km altitude.

Satellite platforms provide the best chance for measurements to achieve global coverage. The average satellite can achieve global coverage within 1-3 days, depending on the viewing configuration. Satellite measurements come in three main viewing geometries: **limb**, **nadir**, and **occultation**.

Limb geometry has already been mentioned - it is the viewing direction looking *through* the atmosphere, approximately tangent to the earth's surface (see Figure 2.19). Limb geometry offers the advantage of excellent vertical resolution of the atmosphere, at the expense of poor horizontal resolution. This is because the line of sight (LOS) spans roughly 2000 km through the atmosphere, with the observed intensity potentially coming from anywhere along that span. However, the horizontal resolution can be increased by assuming the majority of the signal in limb geometry will come from the densest portion of the atmosphere viewed, which is the lowest vertical position along the LOS, known as the *tangent point*. Still, this distance will be on the order of hundreds of kilometres. Limb measurements are most useful in the UV-VIS-NIR region, as FIR measurements may be difficult to discern from what altitude most of the signal is coming from in optically thick portions of the spectrum, and the tangent point approximation is lost. Occultation geometry looks through the atmosphere straight at the sun, either when ascending to the day side of the earth or descending to the night side. This offers the advantage of a high signal-to-noise ratio, as the signal directly from the sun washes out any diffuse scattered sunlight, and the measurement is the transmission of the atmosphere. The disadvantage is very poor spatial coverage - only 1-2 measurements can be made per orbit, and global coverage takes longer to achieve. Occultation measurements are

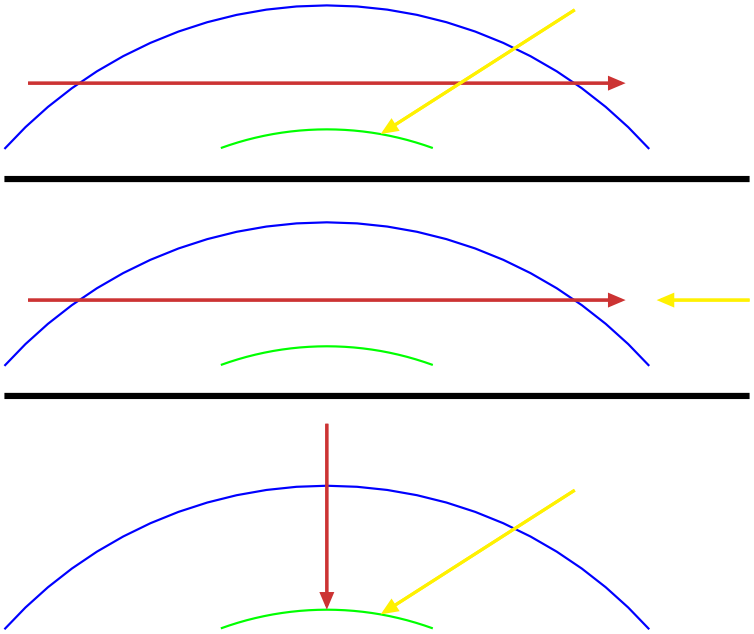

Figure 2.19: The three viewing geometries for satellite platforms, red is the observer line of sight, and yellow is the incoming solar rays. From top to bottom: limb, occultation, nadir.

not useful in the mid and far infra-red, as the sun's intensity has diminished several orders of magnitude.

Nadir geometry looks down at the ground through the atmosphere. This has the advantage of excellent horizontal resolution, with moderate to poor vertical resolution. Nadir measurements offer the best geometry for viewing mid and far infra-red radiation, though they are still used in UV-VIS measurements. Table 2.2 summarizes the main satellites instruments used for retrieval of greenhouse gases, excluding those used only in the UV-VIS and microwave portions of the spectrum.

In this chapter, fundamental properties of the atmosphere were introduced. The temperature and pressure profiles of the atmosphere were outlined, and the distribution and optical properties of the main greenhouse gases was illustrated. Lastly an outline of measurement techniques of these greenhouse gases was shown. The following chapter will delve into radiative transfer theory, the study of how electromagnetic radiation propagates through matter.

Instrument	Type	Active	Focus	Modes	Spectral Regions	Measurement Bands (cm^{-1})
GOSAT	Fourier transform spectrometer	Jan 2009 - present	CO_2, CH_4	Nadir (+/- 35^o)	NIR, FIR	12900 - 13200 5800 - 6400 4800 - 5200 700 - 1800
SCIA-MACHY	High -resolution imaging double spectrometer	Mar 2002 - Apr 2012	H_2O, CH_4, N_2O, NO_2, SO_2, HCHO, BrO, OClO, H_2CO, CO_2, CO, ClO, O_3	Nadir Limb Occultation	UV, VIS, NIR	24691 - 32362 16129 - 25380 12422 - 16556 9524 - 12739 4902 - 5155 4202 - 4415
MIPAS	Michelson interferometer	Mar 2002 - Apr 2012	O_3, H_2O, CH_4, N_2O, HNO_3, NO_2	Limb	MIR, FIR	685 - 2410
OCO-2	Diffraction grating	Launch set Jul 2014	CO_2	Nadir	NIR	6211 region 4854 region
IASI	Michelson interferometer	Oct 2006 - present	O_3, CO_2, CH_4, N_2O CO	Nadir (+/- 48.3^o)	MIR, FIR	645 - 2760
AIRS	Fourier transform spectrometer	May 2002 - present	CO_2, H_2O, CH_4, SO_2 O_3	Nadir (+/- 48.95^o)	MIR, FIR	2150 - 2700
MOPITT	Gas correlation spectrometer	Dec 1999 - present	CO, CH_4	Nadir	NIR, MIR	2128 region 4545 region 4348 region

Table 2.2: Various infra-red atmosphere-monitoring satellite-mounted instruments.

Specifically, the radiative transfer theory is focused on the propagation of light through the atmosphere.

Chapter 3

Radiative Transfer

> No one lights a lamp in order to hide it behind the door: the purpose of light is to create more light, to open people's eyes, to reveal the marvels around.
>
> Paulo Coelho

3.1 Background theory

Signatures of atmospheric trace gases are contained in the outgoing ultraviolet, visible, and infrared light propogating inside and away from the earth's atmosphere. Therefore it is necessary to understand the processes electromagnetic radiation undergoes when interacting with a semi-transparent material, such as air molecules, and with opaque materials, such as the ground. Radiative transfer theory allows us to determine the way light propogates through such materials. The natural starting point for any such study of electromagnetic radiation is Maxwell's equations. In an arbitrary material with permittivity ϵ and permeability μ, and electromagnetic radiation with electric field $\mathbf{E}$ and magnetic field $\mathbf{H}$, Maxwell's equations are

written as,

$$\begin{aligned} \epsilon\dot{\mathbf{E}} + \mathbf{J} &= \nabla \times \mathbf{H}, \\ \mu\dot{\mathbf{H}} &= -\nabla \times \mathbf{E}, \\ \nabla \cdot \mathbf{E} &= \frac{\rho}{\epsilon}, \\ \nabla \cdot \mathbf{H} &= 0, \end{aligned}$$

where $\mathbf{J} = \sigma\mathbf{E}$ is the current density, σ is the conductivity, ρ is the charge density, and the "dot" denotes a derivative with respect to time. In a vaccuum, $\epsilon \to \epsilon_0$ and $\mu \to \mu_0$, and $\mathbf{J} = \rho = 0$. With this in place, the first two equations become coupled, and with the introduction of either a change in the electric field or magnetic field with time, electromagnetic radiation will propogate - this is Huygen's principle. Working in a charge- and current-free region in a given medium, one can use the first two equations to obtain a second-order differential equation for $\mathbf{E}$. This is an equation in three dimensions, so it must be solved individually for all three components of the electric field: E_x, E_y, and E_z, each as a function of x, y, z, and t. In most radiative transfer applications, the conductivity $\sigma = 0$, so the differential equation becomes,

$$\ddot{\mathbf{E}} = -\frac{1}{\epsilon\mu}\nabla^2\mathbf{E}. \tag{3.1}$$

This is the all-familiar wave equation, with general solution,

$$\mathbf{E} = \tilde{\mathbf{E}}_0 \exp(i\mathbf{k} \cdot \mathbf{r} - i\omega\, t). \tag{3.2}$$

Equation 3.2 represents an electric field propagating in the direction of the wave vector $\mathbf{k}$ with oscillation frequency ω and complex amplitude $\tilde{\mathbf{E}}_0$. Normally $\mathbf{k}$ is aligned with the

z-axis, forcing the z-component of the electric field to be zero. Thus we obtain,

$$\tilde{\mathbf{E}} = (\tilde{E}_{0x}\hat{\mathbf{i}} + \tilde{E}_{0y}\hat{\mathbf{j}})e^{i(kz-\omega t)}. \tag{3.3}$$

In this case, k is the wave number, and is related to ω simply by,

$$\frac{\omega}{k} = \frac{1}{\sqrt{\epsilon\mu}} \equiv \frac{c}{n}, \tag{3.4}$$

where n is the index of refraction of the material the wave is passing through. Note that both $\tilde{E}_{0x}$ and $\tilde{E}_{0y}$ have a phase ϕ_x and ϕ_y with them, which is what determines the polarization of the electric field in question. Now in any measurement of electromagnetic radiation, the actual measured quantity is the intensity of the beam, which is proportional to the square of the average amplitude of the electric field,

$$I = \frac{\eta}{2Z_0}(|\tilde{E}_{0x}|^2 + |\tilde{E}_{0y}|^2), \tag{3.5}$$

where Z_0 is the characteristic impedance of free space, and η is the wave impedance. Additional terms arising from functions of $\tilde{E}_{0x}$ and $\tilde{E}_{0y}$ yield the **Stokes' parameters** Q, U, and V, which define the degree of polarization of the electromagnetic wave,

$$\begin{aligned} Q &= \frac{\eta}{2Z_0}(|\tilde{E}_{0x}|^2 - |\tilde{E}_{0y}|^2), & (3.6)\\ U &= \frac{\eta}{2Z_0}(2\,\mathrm{Re}(\tilde{E}_{0x}\tilde{E}_{0y}*)), & (3.7)\\ V &= \frac{\eta}{2Z_0}(-2\,\mathrm{Im}(\tilde{E}_{0x}\tilde{E}_{0y}*)). & (3.8) \end{aligned}$$

The quantity Q represents the degree of horizontal polarization, U represents the degree of 45°polarization, and V represents the degree of right-hand circular polarization. When dealing with partially polarized light, this is the most common way to represent it. In the

analysis of scattering of light off of asymmetrical and partially symmetric particles, it is important to use each of these parameters to characterize the scattered light. However, in the bulk of this work we will only be concerned with the overall intensity of the beam, I.

3.2 Propogation of Electromagnetic Radiation in Material

The purpose of radiative transfer is to quantify how light is attenuated and redirected as it travels through a material. Consider a differential amount of radiant energy dE_λ incident on an elemental area dA at normal angle θ, in a time interval dt, in a specified wavelength interval λ to $\lambda + d\lambda$, confined to a differential solid angle $d\Omega$ in the direction $\hat{\mathbf{\Omega}}$. We relate these quantities by the linear factor I_λ,

$$dE_\lambda = I_\lambda \cos\theta \, d\Omega \, dA \, d\lambda \, dt. \tag{3.9}$$

This can be used to define the **spectral radiance**,

$$I_\lambda = \frac{dE_\lambda}{\cos\theta \, d\Omega \, d\lambda \, dA \, dt} \quad \left[\frac{\text{photons}}{\text{s} \cdot \text{cm}^2 \cdot \text{sr} \cdot \text{nm}} \right]. \tag{3.10}$$

The radiance can be transformed to a “per-wavelength-interval" if that better matches the instruments measurements - for example, Fourier transform spectrometers sample radiances uniformly in wavenumber (frequency) space, while a spectrograph (i.e. an instrument which utilizes a diffraction grating, such as OSIRIS) samples evenly in wavelength space. The units can be transformed with the general relation $\nu = \frac{c}{\lambda} \rightarrow |d\nu| = \frac{c\, d\lambda}{\lambda^2}$. Therefore, the spectral

radiance as a function of frequency/wavenumber, I_ν is,

$$I_\nu = \frac{\lambda^2}{c} I_\lambda \left[\frac{\mathrm{W}}{\mathrm{cm}^2 \cdot \mathrm{sr} \cdot \mathrm{cm}^{-1}} \right]. \tag{3.11}$$

3.3 The Equation of Transfer

The following section on the derivation of the equation of transfer follows closely to the derivation of the equation of transfer found in Bourassa (2007), and reproduces a number of figures found in said thesis. The formulation of the equation of radiative transfer requires specifying the radiation field at some point $\mathbf{r}$ in a propagation direction $\hat{\mathbf{\Omega}}$, and how it transports from one location to the next. Assuming radiation traverses space in a straight line given by the propagation direction, it is useful to define the geometric path coordinate s,

$$\mathbf{r} = \mathbf{r}_0 + \hat{\mathbf{\Omega}}\, s, \tag{3.12}$$

where $\mathbf{r}_0$ is the reference point, defined as $s = 0$. The radiation travels in the direction of decreasing s, as the observer is usually defined to be at position $\mathbf{r}_0$. Refer to Figure 3.1.

We begin by considering the general equation of transfer for a “pencil of radiation" passing through a medium. Naturally, the radiation will be weakened by its interaction with the matter. If the spectral radiance I_λ becomes $I_\lambda + dI_\lambda$ after traversing a thickness ds, then,

$$dI_\lambda = -k_\lambda\, I_\lambda\, ds,$$

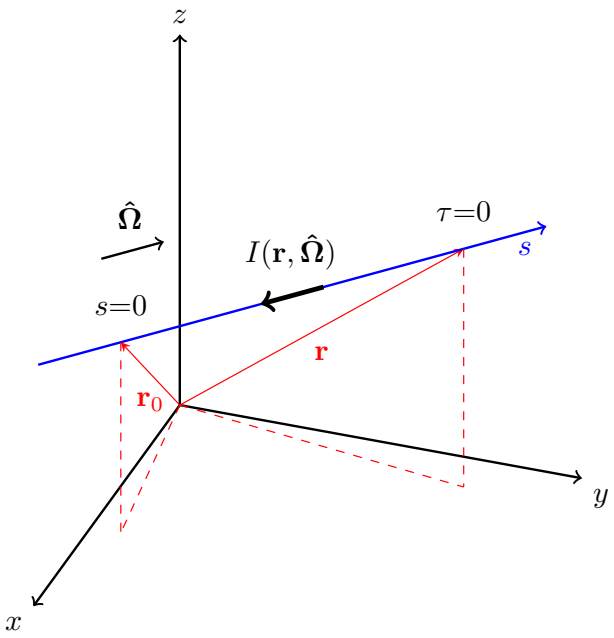

Figure 3.1: The radiation path length coordinate, s, given by the look direction $\hat{\mathbf{\Omega}}$ from an observer $\mathbf{r}_0$ and end path point $\mathbf{r}$. The optical depth $\tau(s)$ is 0 at the end point of the ray and increases with decreasing path distance s.

where k_λ is the total *extinction* of the radiation along the propagation direction, and has units of inverse length. This extinction is due to a combination of radiation being absorbed and scattering of the radiation away from the propagation direction by the material,

$$k_\lambda(s) = k_{\lambda,abs}(s) + k_{\lambda,scat}(s), \tag{3.13}$$

$$k_\lambda(s) = \sum_i n_{i,abs}(s)\sigma_{i,abs}(s) + \sum_j n_{j,scat}(s)\sigma_{j,scat}(s). \tag{3.14}$$

The different subscripts denote extinction due to absorption and scattering processes, respectively. The number density per unit volume, n [cm^{-3}], and the cross section, σ [cm^2], are both functions of position along the propagation direction - in atmospheric applications they generally only vary with altitude above the ground. The **cross section** is an effective area that describes the likelihood of photons interacting with a single molecule, either through absorption or scattering. The summation denotes that many types of molecules can contribute

to the overall extinction. However, the intensity may also be *increased* by emission of the material plus radiation from all other directions scattering into the propagation direction. Defining the source function coefficient j_λ (or volume emission coefficient), the increase of radiance is given by,

$$dI_\lambda = j_\lambda ds.$$

It is convenient to define the source function J_λ such that,

$$J_\lambda \equiv j_\lambda / k_\lambda,$$

so that the source function has the same units of radiance as I_λ. The total change in radiance is then given by,

$$\frac{dI_\lambda}{ds} = -k_\lambda \, I_\lambda + k_\lambda \, J_\lambda. \tag{3.15}$$

This is the general equation of radiative transfer, without any coordinate system imposed. In atmospheric applications, the source function J_λ is a combination of scattered sunlight and blackbody radiation from the ground and air. The boundary conditions for equation 3.15 are the top of the atmosphere (typically defined to be 100 km) and the earth's surface. Theoretically the entire latitude-longitude range of the earth should be included, but local radiance dominates in all realistic applications, so the latitude and longitude are greatly reduced - for example, in the case of a satellite looking straight down at the ground (nadir geometry), the vast majority of the light interacts with the atmosphere in a region directly below the satellite. The following sections will look closer at the absorption, scattering, and emission processes contained within equation 3.15. From here on, the subscript λ will be dropped for brevity, as most processes are assumed to have some wavelength dependence.

3.3.1 Absorption & Scattering

When emissions can be neglected, and the frequency of the incident radiation is near to the resonance frequency of text itsome of the molecules in the volume but far from the resonance frequency of others, the incoming radiance will be increased by incoming scattered light and reduced by a combination of absorption in the material and scattering out of the propagation direction. Then equation 3.15 reduces to,

$$\frac{dI}{ds} = -k(s)\, I(s).$$

Defining the incident radiance $I(s)$ at s$'$ = s and $I(0)$ as the final observed radiance along the propagation direction (see Figure 3.1), we obtain,

$$I(0) = I(s) \exp\left(-\int_{s}^{0} k(s')\, ds' \right) \tag{3.16}$$

Defining the unit-less quantity τ, the optical depth, as the line integral of all absorption and scattering processes along the propagation direction,

$$\tau = \int_{s}^{0} (k_{abs} + k_{scat})\, ds, \tag{3.17}$$

then equation 3.16 becomes,

$$I(0) = I(s)\, e^{-\tau}. \tag{3.18}$$

Equation 3.18 is known as the Beer-Bouguer-Lambert Law. A more detailed look at the molecular processes behind absorption (and emission) will occur in following sections.

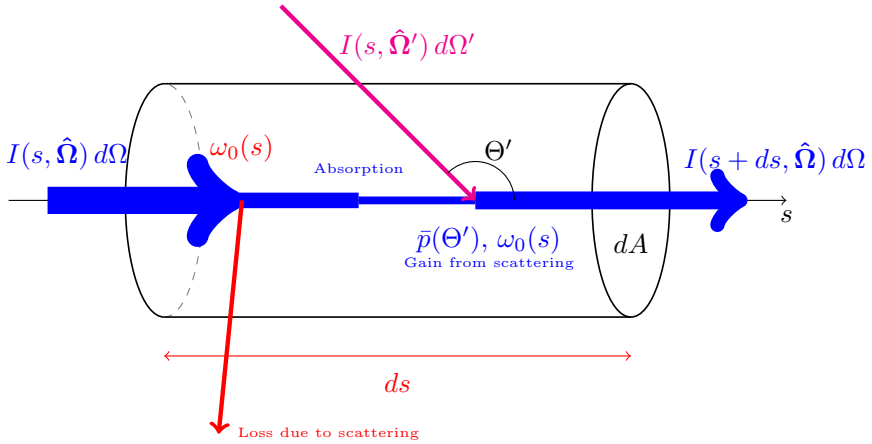

Figure 3.2: Differential geometry for scattering and absorption processes in a volume element of length ds and cross-sectional area dA. Incident radiance is attenuated by absorption and scattering out of the look direction $\hat{\mathbf{\Omega}}$ characterized by the single scatter albedo ω_0, and is increased by radiance from all other directions $\hat{\mathbf{\Omega}}'$ scattering into the look direction, characterized by the single scatter albedo and mean phase function $\bar{p}(\Theta')$ for the scattering angle Θ'.

Scattering also has the effect of *adding* radiation into the propagation direction from all other directions. Figure 3.2 shows how radiation is both removed from the propagation direction by scattering and increased from radiation scattering from all other directions. The source function is given by the radiance from all directions scattering at some path point s into the propagation direction $\hat{\mathbf{\Omega}}$,

$$J(s, \hat{\mathbf{\Omega}}) = \frac{k_{scat}(s)}{k(s)} \int_{4\pi} I(\mathbf{r}, \hat{\mathbf{\Omega}}')\, \bar{p}(s, \Theta)\, d\Omega' \quad \left[\frac{\text{photons}}{\text{s} \cdot \text{cm}^3 \cdot \text{sr} \cdot \text{nm}} \right], \tag{3.19}$$

where $I(\mathbf{r}, \hat{\mathbf{\Omega}}')$ is in the general form of the radiance field to indicate that it is coming from all directions and scattering into the propagation direction $\hat{\mathbf{\Omega}}$. The effective phase function, $\bar{p}(s, \Theta)$, defines the probability of radiation scattering from the $\hat{\mathbf{\Omega}}'$ direction to the $\hat{\mathbf{\Omega}}$ direction at ray position s and scattering angle Θ defined by,

$$\Theta = \cos^{-1}(\hat{\Omega} \cdot \hat{\Omega}'). \tag{3.20}$$

The effective phase function $\bar{p}(s, \Theta)$ takes into account all types of scattering molecules present at the scattering point, by taking a weighted average of their individual phase functions and number densities at that point. The fraction $\frac{k_{scat}(s)}{k(s)}$ is required because $1 - \frac{k_{scat}(s)}{k(s)}$ of the radiation is absorbed at the scattering location, and the remainder is scattered. This is sometimes referred to as the single scattering albedo, ω_0. The phase function is normalized by integrating over all solid angles,

$$\frac{1}{4\pi} \int_0^{2\pi} \int_0^{\pi} \bar{p}(\theta) \, \sin\theta \, d\theta \, d\phi = 1. \tag{3.21}$$

Rayleigh Scattering

The phase function is highly wavelength- and geometry-dependent. For molecules much smaller than the incident electromagnetic wave, they can be approximated as tiny spheres. Assuming the polarizability of the molecule is proportional to the electric field, the incident electric field will create a dipole given by,

$$\mathbf{p} = \alpha \mathbf{E}_0, \tag{3.22}$$

where α is the polarizability of the molecule. In general, α is a tensor that depends on the orientation and shape of the molecule. In the Rayleigh-small sphere limit, we ignore this effect. However, most Rayleigh-scattering particles in the atmosphere are diatomic molecules (O_2 and N_2), and thus exhibit a small non-linear component. The electromagnetic field will cause the molecule to oscillate in the plane of the electric field at the same frequency, causing the molecule to emit as a dipole (see Figure 3.3).

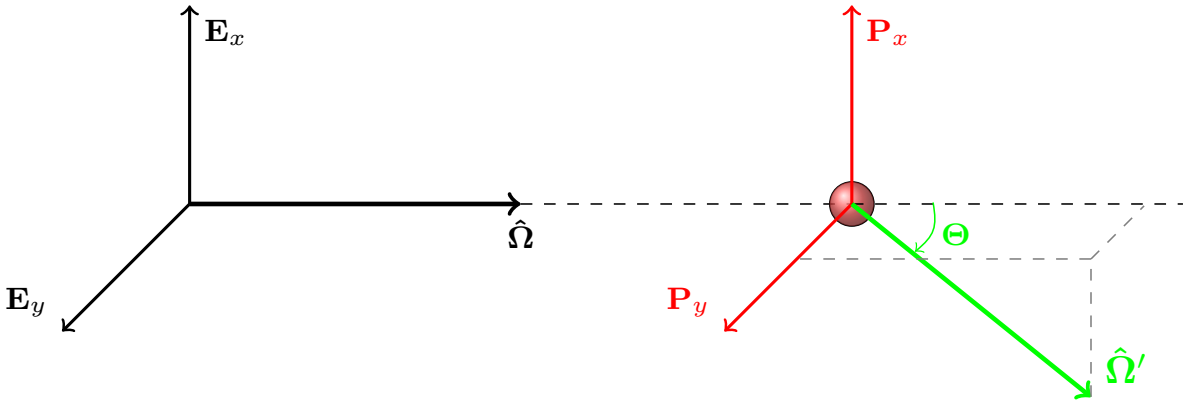

Figure 3.3: Geometry for light scattering off of a molecule. This figure represents the Rayleigh-scattering regime. The incident light (with orthogonal components $\mathbf{E}_x$ and $\mathbf{E}_y$) with frequency ω induces a dipole (a combination of the orthogonal components $\mathbf{P}_x$ and $\mathbf{P}_y$) oscillating at the same frequency. The dipole is in the same direction as the electric field, so long as the polarizability α is not a tensor. The resulting scattered field is the field emitted by the oscillating dipole at the scattering angle $\mathbf{\Theta}$.

The resulting phase function is,

$$p(\Theta) = \frac{3}{4}(1 + \cos^2 \Theta), \tag{3.23}$$

and the scattering cross section σ_{scat} is,

$$\sigma_{scat} = \frac{128\alpha^2\pi^5}{3\lambda^4}. \tag{3.24}$$

This is the dominant type of scattering in the atmosphere, as N_2 and O_2 scatter visible light according to this regime. Notice that the cross section is proportional to the inverse fourth power of the wavelength. This roughly explains why we see the sky to be blue during the day - blue light scatters 5.5 times more than red light. However, at sunset sunlight has much longer to travel through the atmosphere, so most of the blue light is scattered away before reaching our eyes, and the sky takes on a red hue (Liou, 1980).

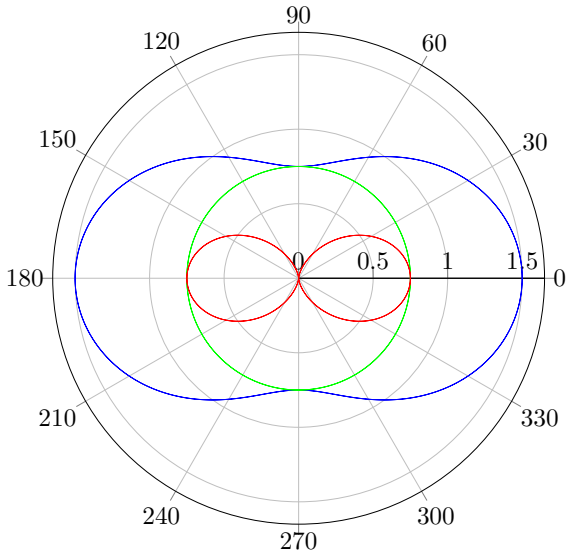

Figure 3.4: Plot of the Rayleigh phase function. The circular distribution (green) is the scattering of polarized light, while the red distribution is the scattering of unpolarized light, which peaks in the forward and backwards directions of the propagation direction, as one would suspect.

Mie Scattering

When spherical dielectric (absorbing) particles are on the same order of size as the wavelength of the incident light, a full analysis of Maxwell's equations is necessary to determine the scattered field. Figure 3.5 shows the geometry for such a condition.

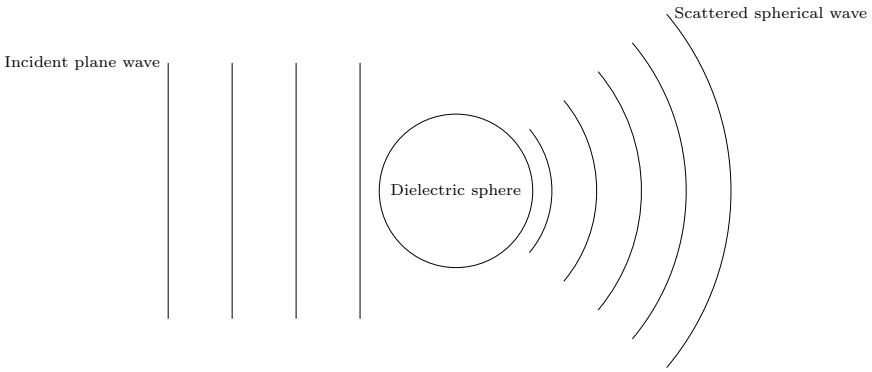

Figure 3.5: Scheme for Mie scattering - a plane wave incident on a dielectric sphere of approximately the same size as the wavelength of light, and the scattered spherical wave. Most solutions are for the scattered wave far from the source.

Scattering by a spherical particle of arbitrary size was treated exactly by Mie in 1908. He considered the incident electromagnetic field as a plane wave, then checked the boundary conditions at the surface with the resulting scattered field and internal field at the boundary for continuity. The final results are expressed as the efficiencies of extinction and scattering, Q(r) and Q_{scat}(r), where r is the radius of the scattering particle approximated as a sphere. The results below only hold for distances much larger than the particle radius, and expressed in terms of the wave number k = $2\pi/\lambda$, are,

$$Q(r) = \frac{2}{(k\,r)^2}\sum_{j=1}^{\infty}(2j+1)Re\{a_j + b_j\}, \tag{3.25}$$

$$Q_{scat}(r) = \frac{2}{(k\,r)^2}\sum_{j=1}^{\infty}(2j+1)\{|a_j|^2 + |b_j|^2\}, \tag{3.26}$$

where a_j and b_j are coefficients given by a combination of half integral order Bessel functions, $\psi_j(\alpha)$, Hankel functions, $\xi_j(\alpha)$, and the index of refraction, n. Refer to Fleagle and Businger (1980) for a full derivation of the functions. The resulting cross sections are given by,

$$\sigma(r) = \pi\,r^2\,Q(r), \tag{3.27}$$

$$\sigma_{scat}(r) = \pi\,r^2\,Q_{scat}(r). \tag{3.28}$$

The scattering phase function is derived in a similar manner. The most common application of Mie scattering is to aerosols in the atmosphere. Aerosols exhibit a highly anisotropic phase function with a large peak in the forward direction (around $\Theta = 0$), and a smaller peak around the backscatter direction ($\Theta = 180$). One common parametrization is the Henyey-Greenstein approximation (Henyey and Greenstein, 1941),

$$p(\Theta) = \frac{1}{4\pi}\frac{1-g^2}{(1-2\,g\cos\Theta+g^2)^{3/2}}, \tag{3.29}$$

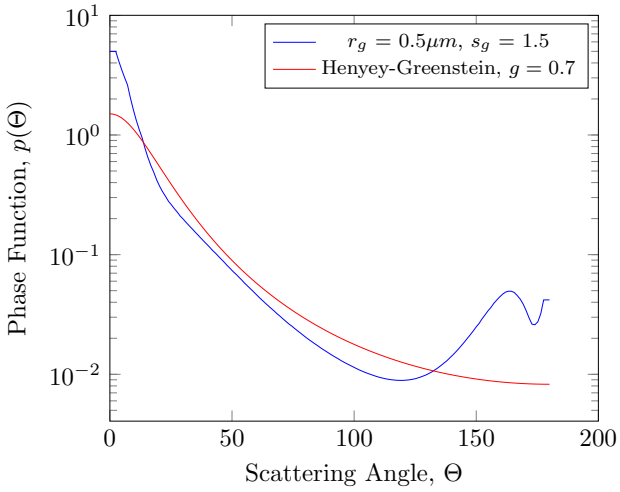

Figure 3.6: Plot of the calculated phase function of an aerosol with mode radius $r_g = 0.5\ \mu m$and mode width $s_g = 1.5$ compared with the Henyey-Greenstein approximation. Note the strong peak in the forward scattering direction. For an explanation of the parameters for calculating the first (more accurate) Mie phase function (Bourassa, 2007).

where g is the asymmetry factor is typically 0.7 for stratospheric aerosols. The full phase function is determined in a more exact way by examining the distribution of radii of a given type of aerosol - typically a log-normal distribution - defined by the parameters r_g (mode radius) and s_g (mode width). A full explanation can be found in Bourassa (2007).

3.3.2 Emission

The last main source to consider is thermal emission by molecules. So long as the material is in local thermodynamic equilibrium (LTE) - that is, it has a well-defined temperature - the material will emit radiation according to a blackbody spectrum. Assuming this property - which is valid for altitudes below 60 km in the earth's atmosphere - the source function, ignoring scattering, is,

$$J(s) = B[\lambda, T(s)], \tag{3.30}$$

where $B_\lambda[\lambda, T(s)]$ is the blackbody function,

$$B_\lambda[\lambda, T(s)] = \frac{2\,\mathrm{h}\,\mathrm{c}^2}{\lambda^5} \frac{1}{e^{hc/k_B \lambda T} - 1} \left[\frac{\text{photons}}{\mathrm{s} \cdot \mathrm{cm}^3 \cdot \mathrm{nm} \cdot \mathrm{sr}} \right]. \tag{3.31}$$

Here, h is Planck's constant, c is the speed of light in vacuum, k_B is Boltzmann's constant, T is the temperature at some path position s, and λ is the wavelength. Figure 3.7 shows the blackbody intensity as a function of wavelength for a number of different temperatures. Note how the peaks shift in wavelength for different temperatures. The details of absorption, emission, and LTE will discussed in a later section.

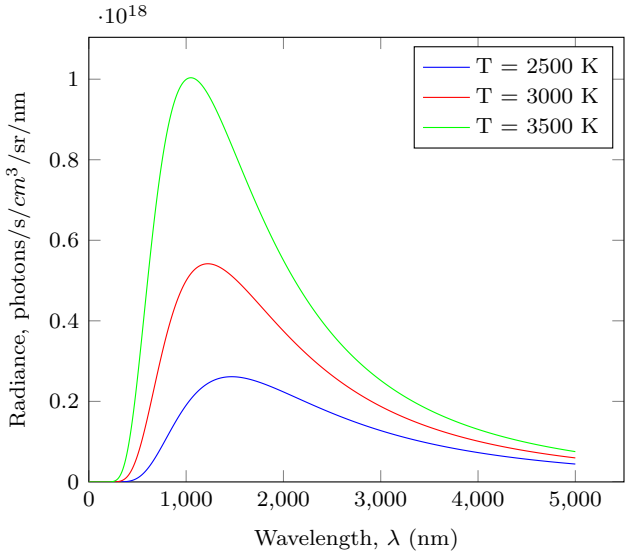

Figure 3.7: Blackbody intensity curves for a number of different emitting temperatures. Notice how the maximum for each curve both shifts in wavelength and increases in intensity with changing temperature.

3.3.3 The Full Radiative Transfer Equation

Assuming an atmosphere where absorption, scattering, and emissions are all significant, the full radiative transfer equation becomes,

$$I(0,\hat{\Omega}) = I(s,\hat{\Omega})e^{-\tau(s)} + \epsilon B[T(s)]e^{-\tau(s)} + \int_s^0 J(s',\hat{\Omega})e^{-\tau(s')}ds', \tag{3.32}$$

$$J(s',\hat{\mathbf{\Omega}}) = k_{abs}(s')B[T(s')] + \int_{4\pi} I(s',\hat{\Omega}')p(\hat{\Omega}';\hat{\Omega})k_{scat}(s')d\Omega'. \tag{3.33}$$

The first two terms, $I(s,\hat{\Omega})e^{-\tau(s)}+\epsilon B[T(s)]e^{-\tau(s)}$, in equation 3.32 are radiance contributions from the end of the line of sight. The first term is non-zero in the case of staring straight at the sun – an **occultation** measurement – the solar irradiance is attenuated by absorption and scattering by the total line of sight transmission $e^{-\tau_{LOS}}$, and all other terms in equation 3.32 become negligible. The first term is also non-zero if the observer is looking at the ground, as radiation diffusely scattering from the ground (either directly from the sun or having already been scattered) will be observed. In this case, we can still put $I(s,\hat{\mathbf{\Omega}})$ in terms of the solar flux. The *flux density*, $F(s,\hat{n})$, in some direction $\hat{\mathbf{n}}$, is defined as the projection of the radiance along $\hat{\mathbf{n}}$ and integrated in solid angle around the half-sphere,

$$F(s,\hat{n}) = \int_{2\pi} I(s,\hat{\mathbf{\Omega}}')\hat{\mathbf{\Omega}}\cdot\hat{\mathbf{n}}\,d\Omega' \quad \left[\frac{\text{photons}}{\text{s}\cdot\text{cm}^2\cdot\text{nm}}\right]. \tag{3.34}$$

To simplify this problem, the ground is often assumed to be a *Lambertian surface*, meaning that the energy emitted/reflected from a surface area element varies with the cosine of the angle from the surface normal. This results in the radiance being the same from all viewing directions. For a Lambertian surface, the radiance in equation 3.34 can come outside the

integral, and the upward reflected flux is,

$$\begin{aligned} F(s,\hat{n}) &= I(s) \int_{2\pi} \hat{\mathbf{\Omega}} \cdot \hat{\mathbf{n}} \, d\Omega', \\ &= I(s) \int_0^{2\pi} \int_0^{\pi/2} \cos\theta' \sin\theta' \, d\theta' \, d\phi', \\ &= \pi \, I(s), \end{aligned} \tag{3.35}$$

where θ' is the angle between $\hat{\mathbf{n}}$ and $\hat{\mathbf{\Omega}}'$. The *albedo* is a ratio that quantifies how much incident downard flux (F_{down}) is relected upwards (F_{up}) from a surface,

$$a = \frac{F_{up}}{F_{down}}, \tag{3.36}$$

and can depend on wavelength. Then for a Lambertian surface, the radiance coming off of the surface is a simple function of the downward flux,

$$I(s) = \frac{a}{\pi} F_{down}. \tag{3.37}$$

The second term $\epsilon \, B[T(s)] \, e^{-\tau(s)}$ in equation 3.32 is the radiance from a blackbody at the end of the line of sight - naturally this would really only occur if the observer was looking at the ground, which has emissivity ϵ. The emissivity is a ratio of how much radiance an object emits compared to a blackbody. The emissivity of the ground only varies slightly, as given in table 3.1.

Material	Emissivity
Ice and snow	0.94-0.99
Vegetation	0.94-0.99
Soil	0.75-0.99
Seawater	0.98-0.99
Grassland	0.95
Barren Land	0.93
Forest	0.96
Urban	0.95

Table 3.1: Emissivities of common geographical features (Zhang, 1999)

The integral in equation 3.32 takes the source function $J(s', \hat{\mathbf{\Omega}})$ at each point along the observer's line of sight and attenuates it back to the origin by the transmission, $e^{-\tau(s')}$. The source function itself is composed of the blackbody emission at the point s' and the incoming radiance from all directions scattered into the look direction $\hat{\mathbf{\Omega}}$. Upon inspection, it is obvious that the full general solution to this system of equations is challenging, due mostly to the scattering of the radiance $I(s, \hat{\mathbf{\Omega}})$. Luckily, the recursive nature of this system of equations can be exploited.

3.3.4 Solution of the Equation: Successive Orders

The full radiative transfer equation 3.32 can be re-written in a form that is more applicable to atmospheric observation. Referring to Figure 3.1, an observer at point $\mathbf{r}_0$ and $s = 0$ with look direction $\hat{\mathbf{\Omega}}$ and end point $s = s_1$ will see radiance given by,

$$I(\mathbf{r}_0, \hat{\mathbf{\Omega}}) = \int_{s_1}^{0} J(s, \hat{\mathbf{\Omega}})\, e^{-\tau(s)}\, k(s)\, ds + \tilde{I}(s_1, \hat{\mathbf{\Omega}})\, e^{-\tau(s_1)} + \tilde{B}[T(s_1)]\, e^{-\tau(s_1)} \tag{3.38}$$

This equation can apply to an observer inside or outside the atmosphere. The end point will either be the top of the atmosphere or the ground. Due to this, the solar radiance and blackbody radiance at the end of the line of sight are denoted as $\tilde{I}$ and $\tilde{B}$, respectively. The source term $J(s, \hat{\mathbf{\Omega}})$ is defined in equation 3.32. The solution of the equation is not readily attainable when scattering is significant in the atmosphere. The source term $J(s, \hat{\mathbf{\Omega}})$ consists of light that has been scattered from elsewhere in the atmosphere, which itself could have been scattered multiple times off the atmosphere and/or ground. The same can be applied to the ground term $\tilde{I}$ at the end of the line of sight, as it consists of multiple-scattered light that is being scattered back up. In addition, thermal emissions within the atmosphere can be scattered multiple times into the line of sight. A general picture is shown in Figures 3.8 and 3.9.

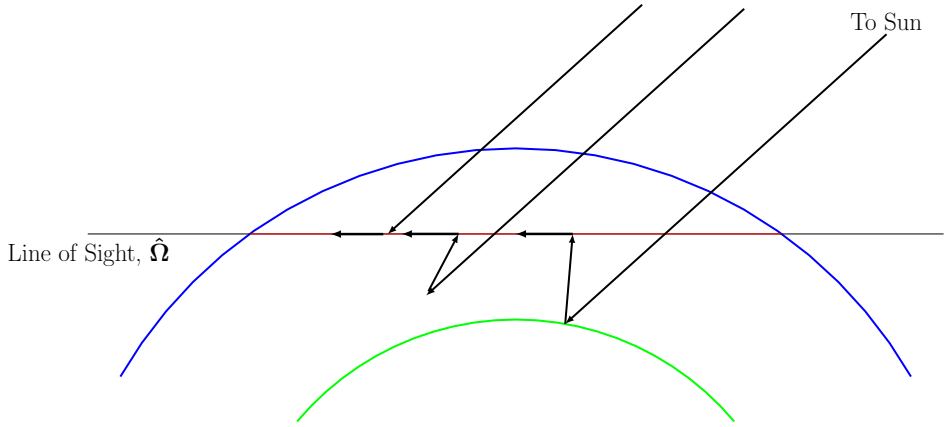

Figure 3.8: Single and multiple scattering of sunlight and within the atmosphere for a typical satellite limb-viewing geometry.

This complexity can be properly handled via the method of *successive orders* - subdividing the source terms (including the ground radiance) by their scattering order. Using this idea, equation 3.38 can be re-written as,

$$\begin{aligned} I(\mathbf{r}_0, \hat{\mathbf{\Omega}}) = \int_{s_1}^{0} \left[J_1(s, \hat{\mathbf{\Omega}}) + J_2(s, \hat{\mathbf{\Omega}}) + \sum_{i=3}^{\infty} J_i(s, \hat{\mathbf{\Omega}}) \right] e^{-\tau(s)}\, k(s)\, ds \\ + \left[\tilde{I}_1(s_1) + \tilde{I}_2(s_1) + \sum_{i=3}^{\infty} \tilde{I}_i(s_1) \right] e^{-\tau(s_1)}. \end{aligned} \tag{3.39}$$

Since light that has been scattered zero (LOS thermal emissions), once, and twice are the most important to the final radiance, they are handled separately from higher order terms and can be dealt with to a higher precision. The i-th order source term $J_i(s, \hat{\mathbf{\Omega}})$ is given by the previous $(i-1)$-th order radiance field $I_{i-1}(\mathbf{r}, \hat{\mathbf{\Omega}}')$,

$$J_i(s, \hat{\mathbf{\Omega}}) = k_{abs}\, B[T(s)] + \omega_0(s) \int_{4\pi} I_{i-1}(s, \hat{\mathbf{\Omega}}')\, \bar{p}(s, \hat{\mathbf{\Omega}}, \hat{\mathbf{\Omega}}')\, d\Omega', \tag{3.40}$$

where $\omega_0(s)$ is the *single-scatter albedo* at point s – a unit-less ratio of the scattering coefficient divided by the extinction coefficient,

$$\omega_0(s) = \frac{k_{sca}(s)}{k_{ext}(s)}. \tag{3.41}$$

This says the source function at any point into a given look direction is given by the blackbody emission at that point plus the radiance from all lower-order scattered radiation scattered at that point into the look direction. The i-th radiance field is determined by,

$$I_i(\mathbf{r}_0, \hat{\mathbf{\Omega}}) = \int_s^0 k(s)\, J_i(s, \hat{\mathbf{\Omega}})\, e^{-\tau(s)}\, ds + \tilde{I}_i(s_1)\, e^{-\tau(s_1)} + \epsilon \tilde{B}[T(s_1)]\, e^{-\tau(s_1)}. \tag{3.42}$$

This says the i-th order radiance seen at the origin of a line of sight with look direction $\hat{\mathbf{\Omega}}$ is calculated by summing the i-th order source functions at each point along the look direction and attenuating them by $e^{-\tau(s)}$ back to the observation point. Also included is multiple-scattered light that has been reflected off the ground ($\tilde{I}_i(s_1)$) and blackbody radiation from the ground $\epsilon \tilde{B}[T(s_1)]$, both of which are attenuated by the transmission function to the ground, $e^{-\tau(s_1)}$.

Figures 3.8 and 3.9 show the general scheme of light emission and scattering in the atmosphere. Figure 3.8 shows the scattering of sunlight directly into the line of sight, off the

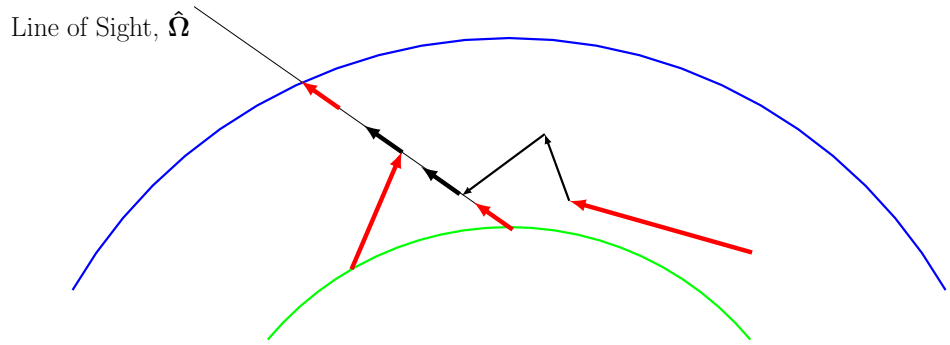

Figure 3.9: Direct and scattered thermal emissions for an arbitrary off-nadir viewing geometry. Direct thermal emissions occur directly along the line of sight, either originating at the ground or in the air. Thermal emissions elsewhere in the atmosphere and ground can also contribute to the line of sight radiance through multiple scattering.

ground and then into the line of sight, and multiply scattered in the atmosphere and ground into the line of sight. Figure 3.9 shows how thermal emissions occur directly along the line of sight in the atmosphere and at the ground. Thermal emissions occurring elsewhere in the atmosphere and on the ground can also contribute to the thermal radiation seen by the observer by scattering, but the contribution is generally quite small in a clean atmosphere, since Rayleigh scattering drops off as $1/\lambda^4$ and thermal radiation is only significant at longer wavelengths. However, the effects of clouds and aerosols may be much larger since their scattering cross-sections may not be insignificant at infra-red wavelengths.

First Order Scattered Light

In the case of sunlight that has been scattered once and thermal emissions that have not yet been scattered (they will always differ by “one order", due to their source existing inside the atmosphere!), the source term in equation 3.40 becomes,

$$J_1(s,\hat{\mathbf{\Omega}}) = \omega_0(s)\, F_0(\hat{\mathbf{\Omega}}_0)\, e^{-\tau(sun,s)}\, \bar{p}(s,\hat{\mathbf{\Omega}},\hat{\mathbf{\Omega}}_0) + B[T(s)] \tag{3.43}$$

where $F_0(\hat{\mathbf{\Omega}}_0)$ is the solar beam irradiance in the direction $\hat{\mathbf{\Omega}}_0$, and $\tau(sun, s)$ is the optical depth from the top of the atmosphere in the direction of $\hat{\mathbf{\Omega}}_0$ to the scattering point s. The ground term in equation 3.42 is given by making use of equation 3.35,

$$\tilde{I}_1(s_1) = \frac{a}{\pi} F_0(\hat{\mathbf{\Omega}}_0)\, e^{-\tau(sun,s_1)}\, \cos(\theta_{sza}), \tag{3.44}$$

where the optical depth is calculated from the top of the atmosphere to the scattering point on the ground, and θ_{sza} is the solar zenith angle at the ground point s_1. Thus the total radiance seen at the observer (located anywhere in or outside the atmosphere at position $\vec{r}_0$) due to all light that has been scattered once, plus thermal emissions along the line of sight, is given by,

$$\begin{aligned} I_1(\mathbf{r}_0, \hat{\mathbf{\Omega}}) = &\int_{s_1}^{0} \Big[\omega_0(s)\, F_0(\hat{\mathbf{\Omega}}_0)\, e^{-\tau(sun,s)}\, \bar{p}(s, \hat{\mathbf{\Omega}}, \hat{\mathbf{\Omega}}_0) + k_{abs}(s)\, B[T(s)]\Big]\, ds \\ &+ \frac{a}{\pi} F_0(\hat{\mathbf{\Omega}}_0)\, e^{-\tau(sun,s_1)}\, \cos(\theta_{sza})\, e^{-\tau(s_1)} + \epsilon\, B[T(s_1)]\, e^{-\tau(s_1)}, \end{aligned} \tag{3.45}$$

where the blackbody radiance emitted by the ground is taken into account. If the LOS does not intersect the ground, the last two terms in equation 3.45 go to zero.

Second Order Scattered Light

The source function at some point s from equation 3.40 that characterizes light that has been scattered twice, $J_2(s, \hat{\mathbf{\Omega}})$, is found by taking all light that has been scattered once and using it as the input light into the point s. This light is integrated in solid angle on the unit sphere and scattered again. Also included is the blackbody emission at the point, s, giving,

$$J_2(s, \hat{\mathbf{\Omega}}) = \omega_0(s) \int_{4\pi} I_1(s, \hat{\mathbf{\Omega}}')\, \bar{p}(s, \hat{\mathbf{\Omega}}, \hat{\mathbf{\Omega}}')\, d\Omega' \tag{3.46}$$

Where $I_1(s, \hat{\mathbf{\Omega}}')$ is given by equation 3.45, representing the lines of sight into the single point at s over the solid angle of the unit sphere. The second-order ground term is given scattering all first order radiances from equation 3.45 at the ground about the upwelling hemisphere:

$$\tilde{I}_2(s_1) = \frac{a}{\pi} \int_{2\pi} I_1(s_1, \hat{\mathbf{\Omega}}') \, \cos(\theta') \, d\Omega' \tag{3.47}$$

Thus the full second order radiance at the observer is determined by taking the line integral along the line of sight of the source function at each point and attenuating it back to the observer located at $\vec{r}_0$, plus the second-order scattered radiance,

$$I_2(\mathbf{r}_0, \hat{\mathbf{\Omega}}) = \int_{2\pi}^{0} J_2(s, \hat{\mathbf{\Omega}}) \, e^{-\tau(s)} \, k(s) \, ds + \tilde{I}_2(s_1) \, e^{-\tau(s_1)} \tag{3.48}$$

Note that there is no blackbody function in either equations 3.48 nor 3.46, as the blackbody function is already contained in the first order radiance terms and is being scattered. Including it in these equations would be erroneously re-emitting radiation!

Higher Order Scattering

All higher order terms can be determined in the same fashion. The i-th source term $J_i(s, \hat{\mathbf{\Omega}})$ is determined by integrating $i-1$-th order incoming radiances, $I_{i-1}(s, \hat{\mathbf{\Omega}}')$, from all directions about the unit sphere and scattering it into the direction $\hat{\mathbf{\Omega}}$,

$$J_i(s, \hat{\mathbf{\Omega}}) = \frac{k_{scat}(s)}{k(s)} \int_{4\pi} I_{i-1}(s, \hat{\mathbf{\Omega}}') \, \bar{p}(s, \hat{\mathbf{\Omega}}, \hat{\mathbf{\Omega}}') \, d\Omega' \tag{3.49}$$

The i-th order radiance seen at some observer located at $\mathbf{r}_0$, $I_i(\mathbf{r}_0, \hat{\mathbf{\Omega}})$, is given by attenuating each source function to the observer by $e^{-\tau(s)}$ and performing the line integral over the entire

line of sight,

$$I_i(\mathbf{r}_0, \hat{\mathbf{\Omega}}) = \int_{s_1}^{0} J_i(s, \hat{\mathbf{\Omega}})\, e^{-\tau(s)}\, k(s)\, ds + \tilde{I}_i(s_1)\, e^{-\tau(s_1)}, \tag{3.50}$$

where the general ground term is determined using Lambertian scattering of the $i-1$-th radiance at the ground,

$$\tilde{I}_i(s_1) = \frac{a}{\pi} \int_{2\pi} I_{i-1}(s_1, \hat{\mathbf{\Omega}}')\, \cos(\theta')\, d\Omega'. \tag{3.51}$$

Equations 3.51, 3.50, and 3.49 constitute a recursive definition of the radiance seen by an observer looking into a multiply-scattering atmosphere. We'll look in a later chapter as to how this is implemented in the SASKTRAN radiative transfer model.

This chapter presented the general equation of radiative transfer for radiation in a material. The general equation was solved for an atmosphere that scatters, emits, and absorbs radiation, including boundary conditions of the top of the atmosphere and ground which also scatters, emits, and absorbs radiation. Using the successive orders of scattering approach, the solution was separated into single and multiple scattering solutions, and the sources of radiation were separated into solar or thermal in origin. A distinction between light scattered and/or emitted from the ground and light scattered and/or emitted from the atmosphere was also made in the system of equations. In the next chapter, the underlying physics of absorption and emission of radiation by molecules will be examined in detail.

Chapter 4

Microphysics of Radiative Processes

> Life is infinitely stranger than anything which the mind of man could invent.
>
> Arthur Conan Doyle

This chapter examines the microscopic details of the absorption and emission of electromagnetic radiation by matter in the atmosphere. Absorption in a general sense will be introduced in the classical and quantum mechanical regimes, and the focus will then be shifted to absorption and emission in the infrared region of the spectrum.

4.1 The Classical View of Absorption

At the most basic level, absorption involves radiation incident on a molecule, and increasing the energy of that molecule. The important part is *how* this radiation is absorbed by the molecule. Classically, molecules are treated as mechanical oscillators and rigid rotators, and thus will have a resonance frequency based on the nature of the "spring" in the oscillator and the moment of inertia of the rotator. Naturally, there is more than one resonance frequency

for the system. These resonance frequencies are the so-called **absorption lines** where the molecule absorbs the incident radiation.

The permittivity ϵ, the permeability μ, and the conductivity σ are the primary quantities that determine how electromagnetic radiation propagates through a material. In a non-conducting material like air, the electrons are bound to specific molecules, and so can be approximated as being bound to the end of an imaginary spring, of which the force is proportional to the electron's velocity,

$$F_{binding} = -m\,\omega_0^2\,x, \tag{4.1}$$

where ω_0 is the natural oscillation frequency of the "spring" and x is the position of the electron. Also present is a damping force on the electron proportional to the velocity. The cause of this damping is unimportant here - energy losses can result from collisions with other molecules, and from the very nature of a classically radiating electron. The damping force is,

$$F_{damping} = -m\gamma\frac{dx}{dt}, \tag{4.2}$$

where γ is a proportionality constant characterizing the damping. When an electromagnetic wave of frequency ω is incident on the molecule, it is polarized in the x direction and feels a driving force,

$$F_{driving} = q\,E_0\,\cos(\omega\,t), \tag{4.3}$$

where q is the charge of the electron, and E_0 is the amplitude of the electric field. Using

these forces, Newton's second law gives,

$$m\frac{d^2x}{dt^2} + m\gamma\frac{dx}{dt} + m\,\omega_0^2\,x = q\,E_0\cos(\omega\,t). \tag{4.4}$$

This equation is easier to handle by regarding it as the real part of a complex equation, $x = \Re[\tilde{x}]$,

$$\frac{d^2\tilde{x}}{dt^2} + \gamma\frac{d\tilde{x}}{dt} + \omega_0^2\tilde{x} = \frac{q}{m}E_0\,e^{-i\omega\,t}. \tag{4.5}$$

The electron oscillates at the same frequency as the incident electric field, but with a difference in phase. The solution is,

$$\tilde{x}(t) = \frac{q/m}{\omega_0^2 - \omega^2 - i\gamma\omega}E_0\,e^{-i\omega\,t}. \tag{4.6}$$

This result can be generalized to account for a material with N molecules per unit volume. In this material, f_j electrons will have resonant frequency ω_j and damping γ_j. Thus the total complex polarization $\tilde{P} = N\,q\tilde{x}(t)$ is,

$$\tilde{\mathbf{P}} = \frac{N\,q^2}{m}\left(\sum_j \frac{f_j}{\omega_j^2 - \omega^2 - i\gamma_j\omega}\right)\tilde{\mathbf{E}}. \tag{4.7}$$

The complex polarizability in equation 4.7 can be expressed as,

$$\tilde{\mathbf{P}} = \epsilon_0\tilde{\chi}_e\tilde{\mathbf{E}}, \tag{4.8}$$

where $\tilde{\chi}_e$ is the *complex susceptibility*. Thus we can obtain the complex permittivity $\tilde{\epsilon} =$

$\epsilon_0(1+\tilde{\chi}_0)$, which gives relative complex dielectric constant $\tilde{\epsilon}_r = \tilde{\epsilon}/\epsilon_0$,

$$\tilde{\epsilon}_r = 1 + \frac{N\,q^2}{m\epsilon_0}\sum_j \frac{f_j}{\omega_j^2 - \omega^2 - i\gamma_j\omega}. \tag{4.9}$$

Since the wave number, k, is defined as ω/c, where c = $1/\sqrt{\epsilon_0\mu_0}$, using the complex permittivity we obtain a complex wave number, which can be written in terms of its real and imaginary parts,

$$\tilde{k} = \sqrt{\tilde{\epsilon}\mu_0}\,\omega \equiv k + i\,\kappa. \tag{4.10}$$

Thus the solution of the wave equation for the propagating electric field (in the z-direction) given by equation 3.2 becomes,

$$\tilde{\mathbf{E}}(z,t) = \tilde{\mathbf{E}}_0\, e^{-\kappa\, z}\, e^{i(k\,z-\omega\,t)}, \tag{4.11}$$

resulting in a wave that is attenuated (or absorbed, if you prefer) in the propagation direction, z. Since intensity is proportional to the square of the electric field, the intensity drops off as $e^{-2\kappa\, z}$, so the quantity $\alpha = 2\kappa$ is called the **absorption coefficient**, with units of inverse length. Approximating the square root in 4.10 as the first two terms in the binomial expansion, $\sqrt{1+\epsilon} \approxeq 1 + \frac{1}{2}\epsilon$, then

$$\alpha(\omega) = \frac{n\,e^2\,\omega^2}{m\,\epsilon_0\,c}\sum_j \frac{f_j\gamma_j}{(\omega_j^2-\omega^2)^2 + \gamma_j^2\omega^2}, \tag{4.12}$$

where n is the molecular number density, and e is the electron charge. This is the absorption at some frequency ω, from the summation of all spectral lines centered at resonant frequencies ω_j with damping coefficients γ_j, derived with a classical approach. Notice how absorption lines at monochromatic frequencies can contribute to absorption at frequencies where there

may be no actual absorption lines - this is the broadening of spectral lines. Equation 4.12 is the case of *natural broadening*. This equation is exactly the same absorption coefficient as k_{abs} found equation 3.14, and has units of inverse length.

Considering only one resonant frequency, $\omega_j = \omega_0$, at a time, the expression can be reduced to a function of frequency $\nu = \omega/2\pi$, assuming that the frequency ω is relatively close to the resonant frequency ω_0 so that $\omega + \omega_0 \approx 2\omega$,

$$\alpha(\nu) = \frac{n\, e^2\, f_{ij}}{16\pi\, m\, \epsilon_0\, c} \frac{\frac{\gamma}{4\pi}}{\pi} \frac{1}{(\nu_0 - \nu)^2 - (\frac{\gamma}{4\pi})^2}. \tag{4.13}$$

The second and third fractions gives the normalized probability distribution of the contribution of a spectral line located at ν_0 to the current frequency ν - this yields the **Lorentz broadening function** $\phi(\Delta\nu)$,

$$\phi(\nu - \nu_0) = \frac{1}{\pi} \frac{\frac{\gamma_L}{4\pi}}{(\nu - \nu_0)^2 + (\frac{\gamma_L}{4\pi})^2} \quad \left[\frac{1}{\text{Hz}}\right]. \tag{4.14}$$

Here, γ_L is the half-width of the spectral line at half-maximum (HWHM) of the central oscillator strength. We will now delve into a more rigorous examination of the absorption coefficient, using quantum mechanics to look at the details of the oscillator strength at ν_0, the location of absorption lines, and the broadening function.

4.2 The Semi-classical View of Absorption

In the previous section, it was assumed in the derivations that the our microscopic oscillators could absorb a continuous spectrum of energy. However, upon Bohr's investigation of the hydrogen spectrum in 1913, it was evident that this was not the case. Absorption and emission of radiation only occurs when the atom makes a transition from one state with

energy E_k to a state with different energy E_j if the difference between the two levels is equal to the energy of the photon absorbed/emitted,

$$|E_k - E_j| = h\nu, \tag{4.15}$$

where h is the Planck constant, and ν is the frequency of the absorbed/emitted photon. The quantity $h\nu$ thus represents the quantum of energy carried by this photon. The lowest energy is called the *ground state* of the atom. When an electron of an atom absorbs energy and jumps into a more energetic orbit, the atom is said to be in an *excited state* (**absorption** -figure 4.1a). The atom can then collapse to a lower energy state due to a "push" from an incident photon (**stimulated emission** - figure 4.1b) or on its own (**spontaneous emission** - figure 4.1c). *These are the three main processes involved in the interaction between matter and radiation.*

Bohr also determined that the angular momentum, L, of the electron in the hydrogen atom can only take on discrete values,

$$L = n\hbar \ \Big[\mathrm{J}\cdot\mathrm{s}\Big]. \tag{4.16}$$

With this selection rule, and using the equations of motion for the electron, Bohr found that the total energy of the hydrogen atom is given by,

$$E_n = -\frac{m_e e^4}{2\hbar^2 n^2}. \tag{4.17}$$

Folllowing this and equation 4.15, the frequency of an emitted photon from the transition of a hydrogen atom from n = j to n = k is given by,

$$\nu = \frac{m_e e^4}{4\pi\hbar}\Big(\frac{1}{j^2} - \frac{1}{k^2}\Big), \tag{4.18}$$

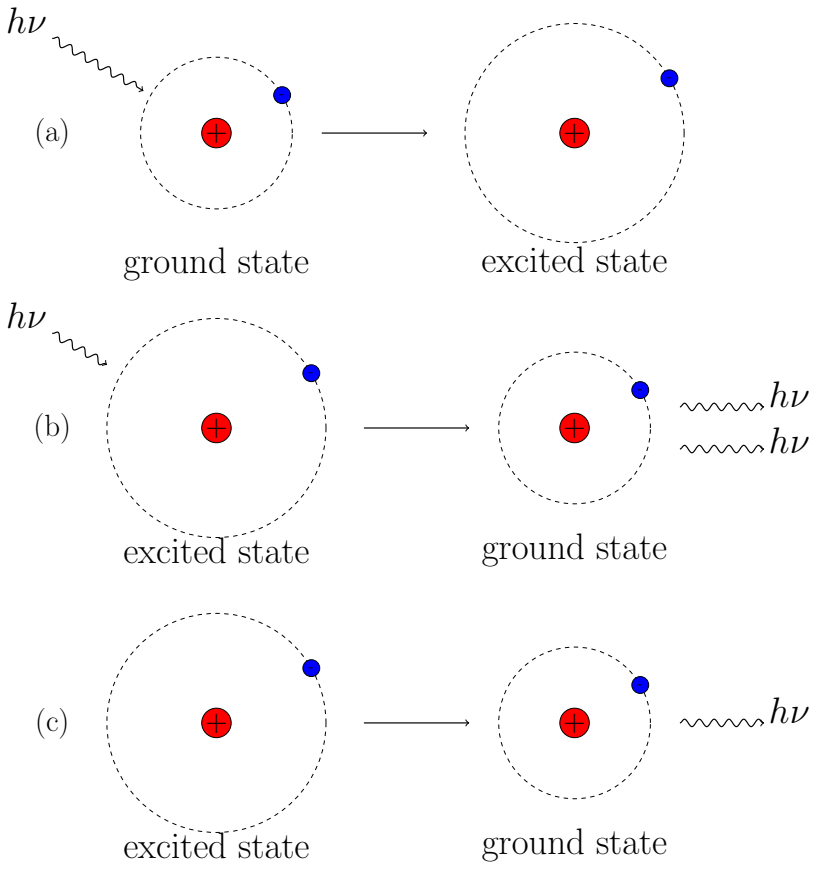

Figure 4.1: Conceptual illustration of the microscopic processes behind absorption (a), stimulated emission (b), and spontaneous emission (c) for a hydrogen atom. In the simplest case of a hydrogen atom alternating between the n=1 and n=2 states, the radius of the orbit simply increases , where r = $n^2 \times 0.53$Å, where n is the quantum number, and 1 Å = $10^{-8} cm$.

which yields all possible frequencies a hydrogen atom can absorb or emit radiation. This basic model for emission and absorption in hydrogen can be expanded to larger atoms and molecules, and though the equations become more complicated, the simple idea remains that *only specific transitions are allowed*. Each of these quantum jumps give way to emission or absorption at a characteristic frequency. These appear as absorption/emission lines in the spectrum of the molecule, and can be quite complex for molecules such as water vapour, carbon dioxide, ozone, and methane, although the spectrum for hydrogen (figure 4.2) is quite simple and follows from equation 4.18.

Figure 4.2: The hydrogen absorption spectrum (top) and emission spectrum (bottom) (Robbins, 2014).

4.2.1 Spectral Line Strengths and Einstein Coefficients

This section goes into the detail of how the *strength* of a molecule's absorption line is determined. As defined in the previous section, when matter and radiation interact, there is a transition of the matter between its upper (u) and lower (l) energy states - the direction of which depends on if it is an absorbing or emitting process. Collisional transitions, involving a radiating molecule and a colliding molecule, can raise or lower the vibrational energy (*b-coefficients*). Interactions between a radiating molecule and a photon can lead to absorption or induced emission, meaning transitions in both directions between the upper and lower energy states (the *C coefficients*). Lastly, radiative transitions can occur spontaneously, though the transition is only in one direction from upper to lower (*A coefficients*).

The prime device which determines the difference between the upper and lower energy states in a molecule is vibration of the bonds between atoms, where the upper state is the more energetic of the vibrations. As mentioned before, these vibrations are modelled as simple harmonic oscillators. Molecules also have energy based on their rotation and velocity, though usually orders of magnitude less than the vibrational energies. Thus within each vibrational state there is a rotational-translational fine structure, ultimately giving rise to the appearance of a vibration-rotation absorption/emission band (see 4.2.3). It is at this point that we need to make an important assumption - the states forming this fine structure are in **local thermodynamic equilibrium** (LTE). This says that a local temperature can be defined such that the kinetic energy of the gas is in equilibrium with the incoming/outgoing radiation

field, and thus the radiation it emits can be defined by the Planck blackbody spectrum. In other words, incident radiation is redistributed among molecules as kinetic energy in such a way that the thermal temperature, T_{therm}, of the molecules is the same as the blackbody temperature, T_{planck}, of the radiation. Likewise, the outgoing radiation from molecules at a given temperature T_{therm} has an equivalent blackbody temperature, T_{planck}, assuming local thermodynamic equilibrium. This concept will be addressed in more detail following this section.

Since the states are in LTE, their relative populations may be integrated into a fixed structure factor, $f(\nu-\nu_0)$, where ν is the frequency of the radiation, and ν_0 is the vibrational transition frequency. f is normalized to 1,

$$\int_{-\infty}^{\infty} f(\nu-\nu_0)\, d(\nu-\nu_0) = 1. \tag{4.19}$$

If we now consider an element of matter with populations $n(l)$ and $n(u)$ per unit volume, interacting with a radiation field with energy density u_ν, and between frequencies ν and $\nu + d\nu$. Since the matter is assumed to be in thermodynamic equilibrium with the radiation, the energy density is defined by,

$$u_\nu = \frac{8\pi\nu^2}{c^3}\frac{1}{e^{\frac{h\nu}{kT}}-1} \quad \left[\frac{\text{photons}}{\text{m}^3\cdot\text{Hz}}\right], \tag{4.20}$$

where the usual expression for u_ν has been divided by $h\nu$ to express the quantity in terms of number of photons per unit volume per unit frequency, instead of energy per unit volume per unit frequency. This will also be applied to the blackbody radiance, B_ν, and radiance, I_ν in the derivations in this section. For a derivation of the energy density of radiation in a cavity, see Appendix A. Using these terms and the Einstein coefficients defined at the beginning of this section, the radiative transitions per unit volume per unit frequency range can now be specified.

Rate of spontaneous emission

$$= n(u)\, A(u,l)\, f_s(\nu - \nu_0) \quad \left[\frac{1}{\mathrm{s}}\right]; \tag{4.21}$$

rate of induced emission

$$= n(u)\, u_\nu\, C(u,l)\, f_i(\nu - \nu_0) \quad \left[\frac{1}{\mathrm{s}}\right]; \tag{4.22}$$

and the rate of absorption

$$= n(l)\, u_\nu\, C(l,u)\, f_a(\nu - \nu_0) \quad \left[\frac{1}{\mathrm{s}}\right]. \tag{4.23}$$

The subscripts on the f's denote different fixed structure factors for each type of radiative transition. In thermal equilibrium, Boltzmann's law states that the distribution of molecules between two states, u and l, is given by,

$$\frac{n(u)}{n(l)} = \frac{g_u\, \exp(-\frac{E_u}{k\,T})}{g_l\, \exp(-\frac{E_l}{k\,T})} = \frac{g_u}{g_l} \exp\Big(- \frac{h\nu_0}{k\,T}\Big), \tag{4.24}$$

where E_u and E_l are the energies of the upper and lower states, g_u and g_l are the degeneracies of the states, and ν_0 is the photon associated with the transition between the u and l states according to Planck's quantum relationship in equation 4.15.

In equilibrium, the rate of molecules making upward transitions (4.23) is equal to the rate of molecules making downward transitions (4.22 and 4.21). Therefore, equating the sum of equations 4.22 and 4.21 with equation 4.23 and rearranging, we can obtain another expression

for the ratio of the upper and lower states,

$$\frac{n(u)}{n(l)} = \frac{C(l,u)\,u_\nu\,f_a}{A(u,l)\,f_s + C(u,l)\,u_\nu\,f_i}. \tag{4.25}$$

Equating 4.24 and 4.25, we obtain relation between the Einstein coefficients, such that,

$$A(u,l)\,f_s = \frac{8\pi\nu^2}{c^3} C(u,l)\,f_i, \tag{4.26}$$

$$C(l,u)\,f_a = \frac{g_u}{g_l} C(u,l)\,f_i. \tag{4.27}$$

Considering the same differential volume of length ds as in Chapter 2 (Radiative Transfer), with radiance I_ν incident, the rate of gain of photons by the radiation field is $[dI_\nu/ds]\,d\Omega$, and the energy density of the field is $I_\nu\,d\Omega/c$. Thus using the rates defined in equations 4.21, 4.22, and 4.23, the rate of gain of photons to the radiation field is,

$$\begin{aligned}\frac{dI_\nu}{ds}d\Omega = &- n(l)\frac{I_\nu\,d\Omega}{c}C(l,u)\,f_a \\ &+ n(u)\frac{I_\nu\,d\Omega}{c}\frac{g_l}{g_u}C(l,u)\,f_a \exp\Big(-\frac{h(\nu-\nu_0)}{k\,T}\Big) \\ &+ n(u)\frac{g_l}{g_u}C(l,u)\,f_a \exp\Big(-\frac{h(\nu-\nu_0)}{k\,T}\Big)\frac{8\pi\nu^2}{c^3}\frac{d\Omega}{4\pi},\end{aligned} \tag{4.28}$$

where the Einstein coefficients were reduced in terms of $C(l,u)$ via relations 4.26 and 4.27. The factor $d\Omega/4\pi$ arises in the third term because spontaneous emission is isotropic (distributed evenly around 4π steradians of the unit sphere), while absorption and stimulated emission occur in the same solid angle direction as the incident radiation. Comparing equation 4.28 to the equation of transfer,

$$\frac{dI_\nu}{ds} = k_\nu(J_\nu - I_\nu),$$

we can find expressions for the source function, J_ν, and the absorption extinction coefficient, k_ν,

$$k_\nu = \frac{C(l,u)\, f_a\, n(l)}{c}(1 - e^{-\frac{h\nu}{k\,T}}), \tag{4.29}$$

$$J_\nu = \frac{2\nu^2}{c^2}\frac{1}{e^{\frac{h\nu}{k\,T}} - 1} = B_\nu. \tag{4.30}$$

To emphasize, equations 4.29 and 4.30 were derived on the assumption of LTE between energy levels of the molecules and the radiation field. Non-thermodynamic equilibrium requires adjusting the equations by the ratio of the population levels at equilibrium to the population levels at non-thermodynamic equilibrium,

$$k_\nu = \frac{C(l,u)\, f_a\, n(l)}{c}(1 - \frac{n(u)}{\bar{n}(u)}\frac{\bar{n}(l)}{n(l)}e^{-\frac{h\nu}{k\,T}}), \tag{4.31}$$

$$J_\nu = B_\nu \frac{n(u)}{\bar{n}(u)}\frac{\bar{k}_\nu}{k_\nu}, \tag{4.32}$$

where the bar indicates that the quantity is at thermodynamic equilibrium. To simplify equations 4.29 and 4.30, ν can be replaced by ν_0, assuming that the radiative transition occurs in frequencies close to the vibrational transition. Thus with this simplifying assumption and equation 4.29, the *integrated line strength*, $S_\nu(l,u)'$, can be obtained,

$$S_\nu(l,u)' = \int_{-\infty}^{\infty} k_\nu\, d\nu = \frac{n(l)\, C(l,u)}{c}\Big[1 - \exp\Big(-\frac{h\nu_0}{k\,T}\Big)\Big] \ \ \Big[\frac{\text{Hz}}{\text{cm}}\Big]. \tag{4.33}$$

We obtain the **spectral line intensity** by dividing 4.33 by the number density N and speed of light c, expressing the frequency in terms of the wavenumber $\tilde{\nu} = \nu/c$, and multiplying by the energy unit per photon, $h\,c\,\tilde{\nu}$, we obtain,

$$S_\nu(l,u) = \frac{n(l)\, C(l,u)\, h\tilde{\nu}}{N\, c}\Big[1 - \exp\Big(-\frac{h\,c\,\tilde{\nu}_0}{k\,T}\Big)\Big] \ \ \Big[\text{cm}^2 \cdot \text{cm}^{-1}\Big], \tag{4.34}$$

which describes the intensity of the "line" of a molecule's absorption spectrum, as seen for hydrogen in figure 4.2. Obviously, $S_\nu(l,u)$ is dependent on the temperature, due to the exponential term and the lower energy state population $n(l)$. A *spectral line database* stores absorption line parameters for molecules, most importantly the wavenumbers and intensities of vibrational transitions. One such database is HITRAN (Rothman et al., 2013), with its most recent release containing 7,400,447 spectral lines for 47 different molecules. The spectral line strength is obviously temperature dependent - the ratio of the same spectral line at different temperatures is as follows,

$$\frac{S_\nu(T_1)}{S_\nu(T_2)} = \frac{\frac{n(l)\,C(l,u)\,h\tilde{\nu}}{N\,c}\left(1-\exp\left(-\frac{h\,c\,\tilde{\nu}_0}{k\,T_1}\right)\right)}{\frac{n(l)\,C(l,u)\,h\tilde{\nu}}{N\,c}\left[1-\exp\left(-\frac{h\,c\,\tilde{\nu}_0}{k\,T_2}\right)\right]} = \frac{n_l(T_1)}{n_l(T_2)}\frac{1-\exp\left(-\frac{h\,c\,\tilde{\nu}_0}{k\,T_1}\right)}{1-\exp\left(-\frac{h\,c\,\tilde{\nu}_0}{k\,T_2}\right)}, \tag{4.35}$$

where the temperature dependent quantities – including the level populations, $n_l(T)$ – were retained and other coefficients cancelled. Since HITRAN stores its spectral lines at a reference temperature, T_{ref}, we can find the spectral line intensity at any temperature,

$$S_\nu(T) = S_\nu(T_{ref})\frac{n_l(T)}{n_l(T_{ref})}\frac{1-exp(-\frac{h\,c\tilde{\nu_0}}{k\,T})}{1-exp(-\frac{h\,c\tilde{\nu_0}}{k\,T_{ref}})} \tag{4.36}$$

Equation 4.36 describes the temperature dependence of a spectral line, based on population levels (n_l) and the Boltzmann distribution. Essentially, the higher the temperature, the more energy readily available to be transferred to molecules from the gas or from molecules to the gas, and the more tendency to absorb/emit radiation. It is worthwhile to note one more time that these equations are derived with the assumption of a local thermodynamic equilibrium (LTE). The details of LTE, and why it is a valid assumption for standard atmospheric conditions, is discussed in the later portions of this chapter.

4.2.2 Quantum Mechanical Broadening

Monochromatic absorption/emission is practically never observed - spectral lines always undergo some sort of broadening effect. This broadening is caused by (a) vibrational damping of the oscillators resulting in a loss of energy - natural broadening, (b) perturbations in energy caused by collisions with other molecules - collisional or Lorentz broadening, and (c) variation in thermal velocities of molecules resulting in a shift in the frequency of emitted/absorbed radiation - Doppler broadening. The effects of (a) are practically negligible in comparison with (b) and (c). In the upper atmosphere, there is a combination of Doppler and Lorentz broadening, and in the lower atmosphere from the surface to the lower portions of the stratosphere (roughly 20 km), Lorentz broadening dominates due to the higher pressures. Above 50 km, Doppler broadening dominates due to the "thin air".

Natural Broadening

The Heisenberg uncertainty principle relates the uncertainty in the energy, ΔE, to the uncertainty in the time, Δt, spent in that excited state,

$$\Delta E \Delta t \geq \frac{\hbar}{2\pi} \tag{4.37}$$

$$\Delta\nu = \frac{\Delta E}{h c} \tag{4.38}$$

$$= \frac{1}{2\pi t_n c}, \tag{4.39}$$

where t_n is the time spent in the excited state. In the thermal infra-red region of the electromagnetic spectrum, an isolated molecule will have a lifetime of $t_n = 0.1$ to $10s$, therefore the uncertainty in wavenumber is,

$$\Delta\tilde{\nu} \approx 10^{-11}\, cm^{-1}, \tag{4.40}$$

which is negligible when compared to Lorentz and Doppler broadening effects.

Lorentz Broadening

Lorentz broadening occurs due to collisions between molecules, greatly reducing the lifetimes of molecules existing in their excited state. With a decrease in excited state lifetime, comes an increase in wavenumber uncertainty.

A more classical view of this is as follows. Imagine a molecule isolated from collisions, and emitting radiation in an excited state. The electromagnetic wavetrain propagating from the molecule will have a distinct frequency – that is, taking the Fourier transform of the wavetrain would result in a single frequency, assuming the molecule has been emitting "forever". However, if we expose our emitting molecule to a collision with another molecule, the wavetrain gets temporarily interrupted, as the collision briefly forms a joint quantum-mechanical system, which will not emit radiation in the same way as before, if at all. This interruption truncates the wavetrain of the radiation in time, so that the Fourier transform of the wave will no longer have a singular frequency – additional frequencies will be introduced, giving way to the "uncertainty" in the absorption line position.

A rough approximation to determine the time between collisions is obtained by taking the average velocity for particles in an ideal gas, treating the molecules as hard spheres of a certain radius, and computing the volume they sweep out in their motion and the likelihood of interacting with another hard sphere. For molecules at STP, the time between collisions is roughly $1.6 \times 10^{-10} s$, giving a line halfwidth of roughly $0.03\, cm^{-1}$ (Goody and Yung, 1989).

The mean velocity, $\bar{v}$ of molecules in an ideal gas follow the Boltzmann distribution,

$$\bar{v} = \sqrt{\frac{8\, k_B\, T}{\pi\, m}}, \tag{4.41}$$

where m is the mass of the molecule, and T is the temperature of the gas. If we assume the molecules to be hard spheres of radius r, a travelling molecule will have a collision if another molecule is within $2r$ of its flight path. The volume of space per unit time, V′, swept out by a molecule moving at $\bar{v}$ where it has a chance of having a collision is,

$$V' = \pi(2r)^2\bar{v}. \tag{4.42}$$

For a gas with n molecules per unit volume, the number of collisions per unit time would be $n\,V'$, and the average time between collisions, t_C, would be,

$$t_C = \frac{1}{nV'} = \frac{1}{4\pi\, r^2\, n\bar{v}}, \tag{4.43}$$

so that the average time between collisions is dependent on the size of molecule, its mass, the temperature, and the number density of molecules. Now the probability of occurance of a collision in a time interval t is $\frac{t}{t_C}$. Dividing the time interval into N equal subintervals, $\Delta t = \frac{t}{N}$, the probability of *no* collisions over the whole time interval is then,

$$p(t) = \lim_{N\to\infty}\left(1 - \frac{t}{N\,t_C}\right)^N = e^{-t/t_C}. \tag{4.44}$$

Normalizing this function from $t = 0$ to $t = \infty$, we obtain the Poisson distribution,

$$P(t) = \frac{1}{t_C}e^{-t/t_C} \tag{4.45}$$

The Poisson distribution probability distribution occurs under conditions of spontaneous emission, with transitions taking place about a mean time interval t_C, and under conditions of collisions where the absorption/emission takes place about some mean time interval t_C. The resulting electromagnetic wavetrain resulting from an energy transition will thus, on the

average, be attenuated by the Poisson distribution,

$$E(t) \propto \frac{1}{t_C} e^{-t/t_C} e^{2\pi\, j\nu_0\, t}. \tag{4.46}$$

Converting to frequency space by taking the Fourier transform, one obtains,

$$E(\nu) \propto \frac{1}{t_C} \frac{1}{1/t_C + 2\pi\, j(\nu - \nu_0)}, \tag{4.47}$$

and the intensity, as a function of frequency, is a proportional to the square of the electric field,

$$I(\nu) \propto E(\nu)E^*(\nu) \propto \frac{1}{(2\pi\, t_C)^2} \frac{1}{(\frac{1}{2\pi\, t_C})^2 + (\nu - \nu_0)^2}, \tag{4.48}$$

where $E^*(\nu)$ is the complex conjugate of the electric field. This intensity as a function of wavelength describes the spread of intensity of radiation from a *single* transition over frequency. It shows how for any realistic energy transitions, there is no such thing as monochromatic radiation. After normalizing the intensity function from $\nu = 0$ to $\nu = \infty$, we obtain,

$$\phi(\nu - \nu_0) = \frac{\alpha/\pi}{(\nu - \nu_0)^2 + \alpha^2}, \tag{4.49}$$

where $\alpha = (2\pi\, t_C)^{-1}$, the width of the absorption line. This is *Lorentz broadening*, and subbing in $\alpha = \gamma_L/4\pi$ we can obtain the same Lorentz broadening equation as we did in the classical oscillator approach, equation 4.14.

Doppler Broadening

For an ideal gas, the fraction of molecules of mass m with speeds between v and $v + dv$ is given by the Boltzmann distribution of velocities,

$$\frac{dN(v)}{N} = \sqrt{\frac{m}{2\pi\, k_B\, T}} e^{-\frac{mv^2}{2k_B T}}\, dv. \tag{4.50}$$

For an electromagnetic source moving at velocity $v << c$, the frequency of light emitted undergoes a **Doppler shift**. The shift in frequency of a molecule emitting radiation and moving at v is,

$$\begin{aligned} \nu &= \nu_0(1 - \frac{v}{c}), \\ v &= \frac{c(\nu - \nu_0)}{\nu_0}, \\ \therefore \left|\frac{dv}{d\nu}\right| &= \frac{c}{\nu_0}, \end{aligned} \tag{4.51}$$

where ν_0 is the *actual* frequency of the radiation observed by an observer moving at the same velocity as the molecule, and ν is the observed shifted frequency as seen be a stationary observer. Substituting these expressions into equation 4.50 yields,

$$\frac{dN(v)}{N} = \frac{1}{\sqrt{2\pi}\sigma} \exp\left(- \frac{(\nu - \nu_0)^2}{2\sigma^2} \right) d\nu, \tag{4.52}$$

where the quantity σ is given by,

$$\sigma = \sqrt{\frac{\nu_0^2\, k_B\, T}{m\, c^2}}. \tag{4.53}$$

Equation 4.52 is a Gaussian and has been normalized. It thus can describe the intensity at ν of a spectral line centred at ν_0. The half width at half maximum (HWHM), γ_D, is the wavenumber distance from the line centre where the intensity is half of its maximum,

$$\begin{aligned} I &= I_0\, e^{-\frac{\gamma_D^2}{2\sigma^2}}, \\ &= \frac{1}{2} I_0, \\ \therefore \sigma &= \frac{\gamma_D}{\sqrt{2\ln 2}}. \end{aligned} \tag{4.54}$$

Since most spectral line databases store γ_D to describe this broadening due to molecular motion, we arrive at the final form of the *Doppler broadening*,

$$\phi_D(\nu - \nu_0) = \sqrt{\frac{\ln 2}{\pi}} \frac{1}{\gamma_D} \exp\Big(- \frac{\ln 2\,(\nu - \nu_0)^2}{\gamma_D^2} \Big). \tag{4.55}$$

Essentially, Doppler broadening arises because of shifts in the frequency (or an "uncertainty") due to the Doppler effect from molecular motion at a certain temperature. This uncertainty in frequency is translated to a blurring of the spectral line centre, resulting in the above Doppler broadening equation.

Voigt Broadening

Realistically, a combination of Doppler and Lorentz broadening occur in the atmosphere. At low altitudes where the pressure is high, the broadening is dominated by Lorentz, but at mid and high altitudes where the pressure is lower, Doppler and Lorentz broadening both play an important role. The combination of the two processes is determined through a convolution

of the functions, resulting in the **Voigt** function,

$$\begin{aligned}\phi_V(\Delta\nu) &= \int_{-\infty}^{\infty} \phi_D(\Delta\nu')\,\phi_L(\Delta\nu - \Delta\nu')d\Delta\nu', \\ &= \sqrt{\frac{\ln 2}{\pi}}\frac{\gamma_L}{\gamma_D}\frac{1}{\pi}\int_{-\infty}^{\infty} \frac{\exp(-\ln 2\,(\Delta\nu')^2\,/\,\gamma_D^2)}{\gamma_L^2 + (\Delta\nu - \Delta\nu')^2}d\Delta\nu'. \end{aligned} \tag{4.56}$$

While both broadening effects occur at the same time, they have different influences on the molecule. Lorentz broadening is the primary process responsible for "deciding" the wavenumber of the emitted/absorbed photon. Once that photon has been emitted/absorbed, it experiences a Doppler shift based on the molecule's velocity. The combined effect of these two types of broadening is equivalent to taking the convolution of the two functions. The Voigt function is the subject of much study, as radiative transfer models require fast and accurate computation of this function for thousands of wavenumbers and numerous altitudes. Making a few changes of variable, the integral expression is equal to the real part of the complex error function,

$$\phi_V(\Delta\nu) = \sqrt{\frac{\ln 2}{\pi}}\frac{1}{\gamma_D}\,k(x,y), \tag{4.57}$$

where $k(x,y)$ is given by,

$$k(x,y) = \Re[e^{-z^2}(1 - erf(-iz))], \tag{4.58}$$

and x, y, and z are given by,

$$x = \frac{\Delta\nu}{\gamma_D}\sqrt{\ln 2}, \tag{4.59}$$

$$y = \frac{\gamma_L}{\gamma_D}\ln 2, \tag{4.60}$$

$$z = x + i\,y. \tag{4.61}$$

Local Thermodynamic Equilibrium and the Principle of Detailed Balance

When it is stated that a body is in thermodynamic equilibrium, it is a way of saying that the source function, J_ν, depends only upon temperature, frequency, and the speed of light - i.e. the Planck function. This simplifies the problem of radiative transfer to such a degree that it is worth our time to investigate the conditions where Planck's blackbody function is an adequate approximation to the source function. Thermodynamic equilibrium is defined when the distribution of molecules between two energy states can be defined by Boltzmann's law,

$$\frac{n(1)}{n(2)} = \frac{g_1}{g_2}\exp(-\frac{E_1 - E_2}{k_B\,T}) = \frac{g_1}{g_2}\exp(-\frac{h\nu_{1,2}}{k_B\,T}), \tag{4.62}$$

where $\nu_{1,2}$ the frequency of the photon associated with the transition between state 1 and 2 according to Planck's law. For complete equilibrium, equation 4.62 is obeyed for all energy states. Obviously, complete thermodynamic equilibrium is an idealization, equivalent to the inside of a constant-temperature enclosure which cannot be accessed and nothing changes inside. Instead we consider *local* thermodynamic equilibrium, where Boltzmann's law applies to certain groups of energy levels, but not all levels. A good example of this is the resonant fluorescence of sodium vapour at room temperature - while the translational energies of the

atoms will be in LTE with the room, the gas glows as if it were at a blackbody temperature of several thousand Kelvin (Goody and Yung, 1989). That is to say, the translational energy of molecules is what we interpret as "temperature" - i.e. the kinetic energy of the molecules causing pressure on a sensor (the skin is likely the most familiar temperature sensor to most people), while radiative energy transitions are defined in terms of the blackbody function. *Thermodynamic equilibrium occurs when the radiative energy is re-distributed among the molecules such that the kinetic temperature of the gas is the same as the blackbody temperature of the radiation.*

Einstein showed that if equation 4.62 is obeyed for the energy levels under consideration, Planck's source function arises, thus Planck's and Boltzmann's laws are interchangeable (Goody and Yung, 1989). It is known that a gas with no incident radiation upon it will arrive at a Boltzmann distribution through collisions alone, and thus will yield a Planck source function. However, collision-less media could have any distribution of energy levels, since there is no direct way for molecules to "communicate" their energy to one another, and as a result Planck's law need not be obeyed. Thus the rate of collisions, $1/\eta$, where η is the relaxation time, and natural lifetime of radiative transitions, ϕ, will adjust the state populations. When $\eta/\phi \ll 1$, LTE will occur and Planck's law is valid, as molecules will collide and redistribute their energy gained from radiation before re-radiating; when $\eta/\phi \gg 1$, a different source function is likely required.

We will primarily be concerned with vibrational, rotational, and translational energy levels of molecules. Electronic energy states are not considered simply because their radiative lifetimes are far too short, always resulting in $\eta/\phi \gg 1$ for normal atmospheric conditions. For translational states, every collision between molecules makes some adjustment to the translational energy states, and disturbance of the equilibrium is caused by molecules arriving from levels with different kinetic temperatures. In all altitudes below the exosphere, the collision rate among molecules is high enough that the translational energy states are all in equilibrium, and thus have a Boltzmann distribution and a well-defined temperature. For

vibrational transitions, at high pressures the vibrational relaxation time is short, and the collisional rate is very high, so that $\eta/\phi \ll 1$. However, with increasing altitude η/ϕ gets larger. For instance, the CO_2 band at 15 μm yields η/ϕ of unity at 76 km above the earth's surface (Goody and Yung, 1989). What's more, a collision with a vibrating molecule will not necessarily transfer all vibrational energy into translational energy - that is, the molecule may keep vibrating. Thus LTE is not always assumed for the vibrational states of molecules - but the disequilibrium of vibrational states is handled much easier than the other energy states. Rotational levels, on the other hand, have a much shorter collisional relaxation time than vibrational levels, and thus $\eta/\phi \ll 1$ is obeyed for rotational energy levels for all altitudes below 150 km.

LTE can be more rigorously defined through the principle of detailed balance. The problem of radiation in full thermodynamic equilibrium inside an enclosure is a well-understood one - through arguments with the Planck distribution and Maxwell's equations, it is determined that the radiation inside the enclosure at some frequency, ν, is dependent *only* on the temperature, T, inside the ideal enclosure Reif (1965). This is obviously a useful result, as it lets one define the radiation emitted by a body at thermal equilibrium by its temperature alone - but is it justified to use this principle for general bodies when it was originally derived for an ideal insulated enclosure? For instance, a light bulb filament is certainly not at the same temperature as the surrounding walls of the room it is enclosed in. The work-around to this apparent problem is to imagine the radiating body to be in an equilibrium situation inside an enclosure containing radiation at its temperature, and then looking at the necessary conditions to maintain this equilibrium.

This is where **detailed balance** is required - if the body is to maintain equilibrium, then each process of emission by the body must be balanced by an inverse process of absorption of incident radiation. Thus we can describe the radiation simply by its temperature, instead of computing the *vastly* more complicating problem of how a collection of interacting atoms in the body emit radiation! The principle of detailed balance essentially says that the power

radiated by a body at any wavelength is equivalent to the power absorbed by the body at the same wavelength. This statement can be made much stronger by doing the following thought experiment. Imagine that the body is surrounded by a shield which absorbs all radiation except that in one small element of area it is completely transparent to radiation in one direction, one polarization, and a narrow frequency range. The shield cannot affect the nature of the radiation inside the enclosure, nor affect the nature of the body's emissivity/absorptivity. Since equilibrium can exist in the presence of the shield, the energy balance must hold for this particular arrangement. In fact, it follows that the power radiated and absorbed by the body must be equal for *any* particular polarization, area element of the body, and frequency range. The microscopic reasons for this go beyond the scope of this thesis, but detailed balance essentially follows from the reversibility of emission and absorption - i.e. emission of a photon with wave vector κ is the same as reversing the sign of time t, and absorbing a photon with wave vector $-\kappa$.

4.2.3 Vibrational and Rotational Spectra

What determines the resonance frequencies that molecules absorb radiation? We showed the simplest case of how a hydrogen atom absorbs radiation - now it is necessary to look at more complex molecules and how they interact with radiation at different frequencies. Due to a molecule's shape and molecular bonds, incident radiation at specific frequencies will cause the molecule to change both vibrational energy and rotational energy - the resulting absorption features of these molecules are referred to as *vibration-rotation bands*.

Molecular vibrations in bonds between atoms are approximated as those of a harmonic oscillator, where the vibrational energy is determined from quantum mechanics as,

$$E_v = \sum_k h\nu \, (v_k + \frac{1}{2}), \tag{4.63}$$

where E_v is the total vibrational energy of the molecule, ν is the resonant frequency of vibration, and $v_k = 0, 1, 2, ...$ is the vibrational quantum number, and k denotes the normal modes. To determine the resonant frequency of vibrations, analysis of the wavefunction of the molecule using Schröedinger's equation is necessary. The result for hydrogen was shown in equation 4.18, as the derivation is comparatively simple to other more complex molecules.

Diatomic molecules, such as O_2 and CO, only have one normal mode, the v_1 stretching mode. Triatomic molecules, such as CO_2 and H_2O, have more options - in addition to atoms stretching in the direction of the bond (**stretching mode**), the whole molecule can bend (**bending mode**). Linear triatomic molecules like CO_2 have four normal modes, but two orthogonal bending modes (v_{2a} and v_{2b}) are degenerate. Non-linear triatomic molecules like H_2O exhibit three bending modes. Energy levels for triatomic molecules are listed as a triad of integers in the form $(v_1 v_2 v_3)$. See figures 4.3 and 4.4. Methane (CH_4) has five nuclei, has nine normal modes, but due to spherical symmetry, only four of these modes are independent.

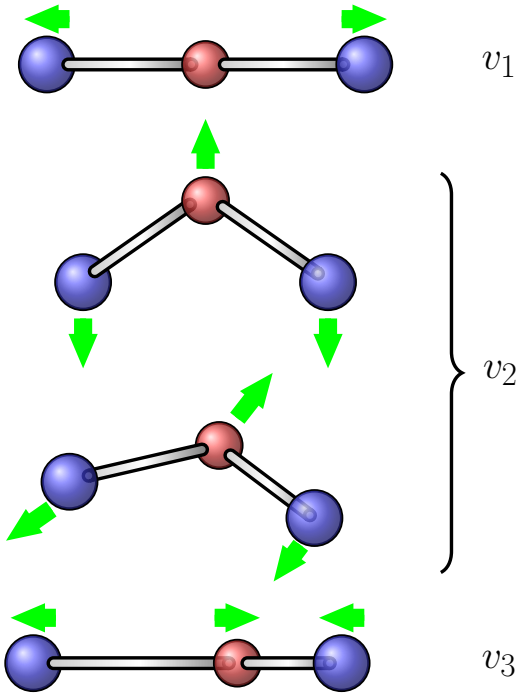

Figure 4.3: Normal vibrational modes of CO_2, a linear triatomic molecule. The v_2 mode is degenerate since the orthogonal modes are indistinguishable from one another

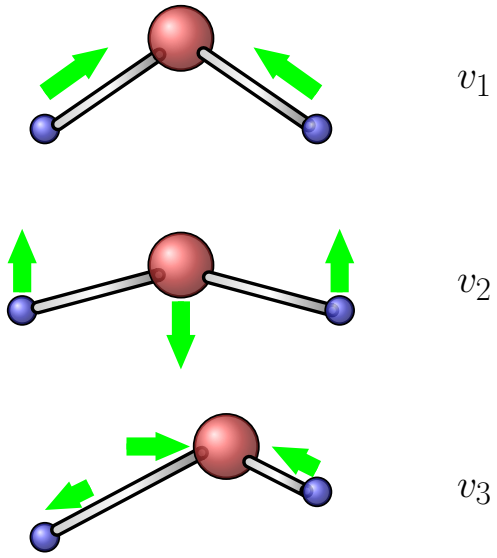

Figure 4.4: Normal vibrational modes of H_2O, a non-linear triatomic molecule.

Through analysis of the wavefunction and dipole moment operator, it can be shown that the only allowed vibrational transitions are where the vibrational quantum number changes by one,

$$\Delta v_k = \pm 1. \tag{4.64}$$

This is the selection rule for a harmonic oscillator. Combined with the energy levels in equation 4.63 and Planck's relation (4.15) that limits the change in energy of the molecule as proportional to the frequency of the absorbed or emitted photon, this yields the frequencies at which a molecule will absorb/emit radiation. Put another way, in the case of absorption, if the incident radiation has a frequency that is equal to the energy difference between vibrational levels separated by one quantum number, then the radiation will be absorbed by the molecule. This determines the strongest absorption bands of the molecule - the *fundamentals*. However, not all of the normal modes may be active (Goody and Yung, 1989).

Rotational energy of the molecule, just like vibrational energy, is quantized. The molecule's

	Fundamental Vibrational Modes			
Molecule	$\nu_{\mathbf{1}}$ (cm^{-1})	$\nu_{\mathbf{2}}$ (cm^{-1})	$\nu_{\mathbf{3}}$ (cm^{-1})	$\nu_{\mathbf{4}}$ (cm^{-1})
H_2O	3650	3750	1600	N/A
CO_2	1388	667	2349	N/A
O_3	1103	701	1042	N/A
CH_4*	2917	1534	3019	1306
N_2O	1298.3	596.3	2282.2	N/A

Table 4.1: Fundamental vibrational modes for common IR-active greenhouse gases.

rotations are modelled as those of a rigid rotor, along the three primary rotational axes A, B, and C. The energy of a rotation is thus,

$$E_r = h\,c\,B\,J(J+1) + h\,c\,(A-B)\,K^2, \tag{4.65}$$

where J = 0, 1, 2, ... is the rotational quantum number, K is another quantum number describing the component of angular momentum along a unique axis of symmetry (if there is one), and the rotational constants A and B are defined by,

$$B, A = \frac{1}{8\pi^2 I_{B,A}} \tag{4.66}$$

and $I_{B,A}$ is the moment of inertia of the molecule in the A and B directions.

Rigid rotors come in four different types: spherical top ($I_A = I_B = I_C \neq 0$, e.g. CH_4), symmetric top ($I_A \neq 0$, $I_B = I_C \neq 0$, e.g. NH_3), linear ($I_A = 0$, $I_B = I_C \neq 0$, e.g. CO_2), and asymmetric top ($I_A \neq I_B \neq I_C$, e.g. H_2O). For spherical tops, A = B, and for linear molecules K = 0, and the energy reduces to,

$$E_r = h\,c\,B\,J\,(J+1), \tag{4.67}$$

for both types of molecules. The apparent similarity between spherical and linear molecules is resolved by noting that spherical tops have a high degree of degeneracy, leading to different rotational spectra. Energy levels for asymmetric tops are a little more complicating, and will not be discussed in detail here. The selection rule for absorbing or emitting photons for rotational states is given by,

$$\Delta J = 0, \pm 1, \text{ but not } J = 0 \text{ to } J = 0, \tag{4.68}$$

For a molecule to change rotational energies due to incident radiation, the molecule needs to exhibit a dipole moment with at least a small component in the same direction as the incident electric field. Thus molecules like water are very rotationally active, particularly in the far infrared and microwave regions of the spectrum. However, most molecules in the atmosphere exhibit no dipole moment at rest, yet they display rotational absorption features. The reason for this resides in vibration-rotation coupling. When a molecule such as carbon dioxide is in the v_2 bending mode, it will gain a momentary dipole, making it weakly rotationally active. Thus most absorption lines in the infra-red region of the electromagnetic spectrum are a combination of vibration and rotation effects.

To find the energy a vibration-rotation transition from J to $J' = J \pm 1$,

$$\begin{aligned}
\Delta E =& h\nu_k + h\,c\,B\,[J'(J'+1) - J(J+1)], \\
\nu =& \nu_k + c\,B\,[(J+1)(J+2) - J(J+1)], \text{ or} \\
\nu =& \nu_k + c\,B\,[J(J-1) - J(J+1)], \\
\therefore\ \nu =& \nu_k \pm 2\,B\,c\,(J+1).
\end{aligned} \tag{4.69}$$

Note that the resulting frequency of absorbed or emitted radiation is shifted from the vibrational mode frequency. The shape of the resulting spectrum is shown in figure 4.6, consisting

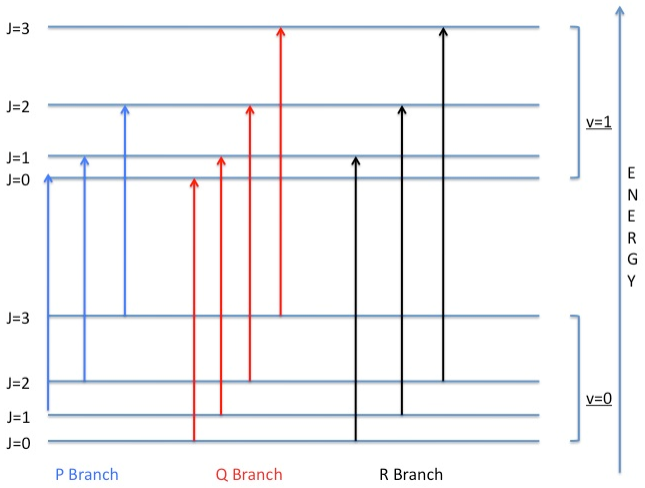

Figure 4.5: Generic energy level diagram showing the different branches associated with a vibrational-rotational energy transition (Lin and Lu, 2014).

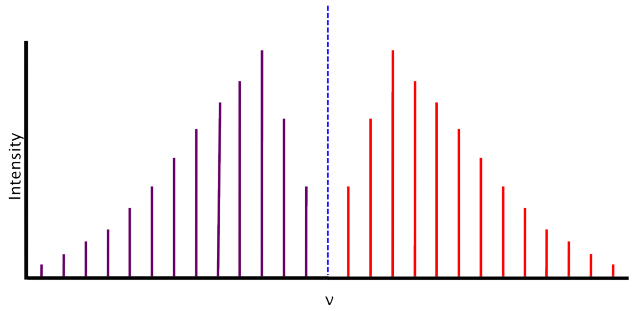

Figure 4.6: Idealized rotation spectrum centred about vibrational frequency ν_k. Initially the intensities of the lines increase as they get farther away from the central frequency, but as the distance increases, the intensity drops off due to the Boltzmann distribution of energy levels - very few transitions will occur where the rotational quantum number changes by a large amount (Lin and Lu, 2014).

of absorption lines equidistant from one another by a value of 2B. As shown in previous sections, the intensity of each line depends on the populations of the ground states for rotational transitions.

The group of lines to the right of the centre frequency, resulting from $\Delta J = 1$, is the R-branch (in French, *riche*, or rich), and the group of lines to the left, resulting from $\Delta J = -1$, is the P-branch (in French, *pauvre*, or poor). The centre frequency, if the $\Delta J = 0$ transition is

allowed, is called the Q-branch (this one is less interesting - it is simply the letter between P and R). In reality, line spectra more closely resemble figure 4.7, before broadening effects are considered.

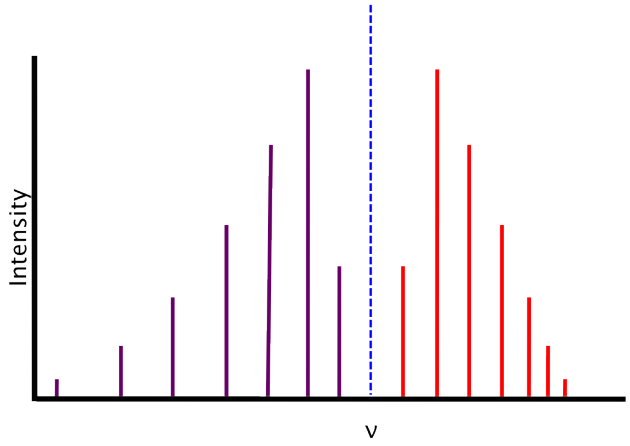

Figure 4.7: Realistic rotational absorption lines centred about vibrational frequency ν_k - before undergoing broadening. The R-branch lines become closer together as frequency increases, and P-branch lines become sparser as frequency decreases, primarily due to centrifugal distortion of the atom increasing the moment of inertia at higher frequencies of incident radiation (Lin and Lu, 2014).

As the energy (frequency) increases, the R-branch lines become increasingly similar in energy (i.e. the spacing decreases between the lines), and as the energy decreases, the P-branch lines become increasingly dissimilar in energy from each other (i.e. the spacing increases). This is due to two phenomena: rotational-vibrational coupling and centrifugal distortion. Coupling occurs essentially because the vibrations of the molecule change the lengths of the bonds between the atoms, and this in turn affects the rotational inertia. Centrifugal distortion is exactly what one would imagine - as a molecule rotates faster, the lengths of its bonds increases, thus increasing the overall moment of inertia. This decreases the B-coefficient, meaning that as frequency increases, B decreases, and the distance between lines gets smaller.

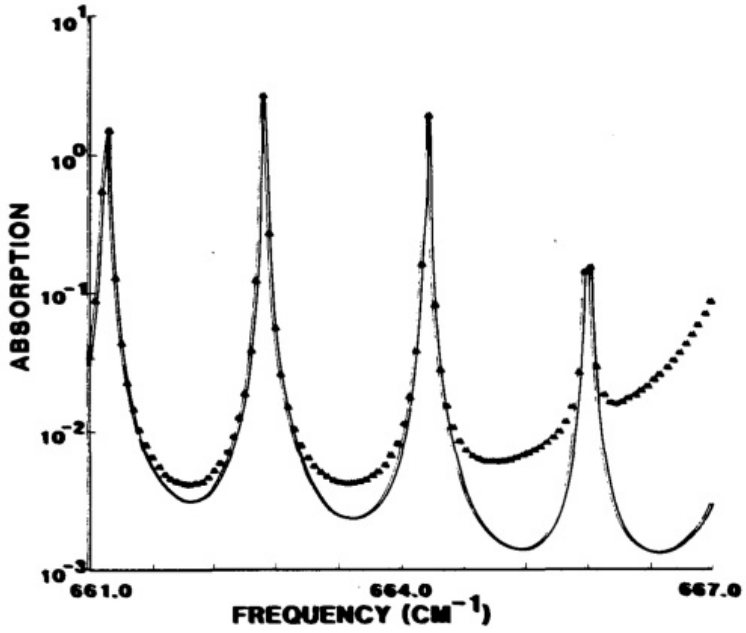

Figure 4.8: Model simulations showing the effects of line mixing in the CO_2 Q-branch around 664 cm^{-1}. The absorption coefficient was computed without line-mixing (dots) and with line-mixing (solid line). Note the over-estimation of the absorption when line-mixing is ignored. Source: (Armstrong, 1982)

A Note on Line Coupling

When the spectral lines of a molecule are very close together, a phenomenon known as line coupling occurs. Line coupling occurs when the a molecule's rotational lines overlap and collisions induce transitions between different rotational states which yield Q-branch lines. These collisions are the main cause of pressure broadening for an isolated transition. But when lines overlap, the collisions can transfer intensity from one line to another; when the cross sections are calculated from these coupled lines, the result is smaller than if the lines were considered separately (Strow and Reuter, 1988). That is, model calculations neglecting line-coupling often result in over-estimation of the absorption coefficients. This is illustrated in figure 4.8,

To explain this process, a simple picture can be given by considering only two optical transitions: f $\leftarrow$ i and f' $\leftarrow$ i' at frequencies ν_{fi} and $\nu_{f'i'}$, respectively. For single photon absorption,

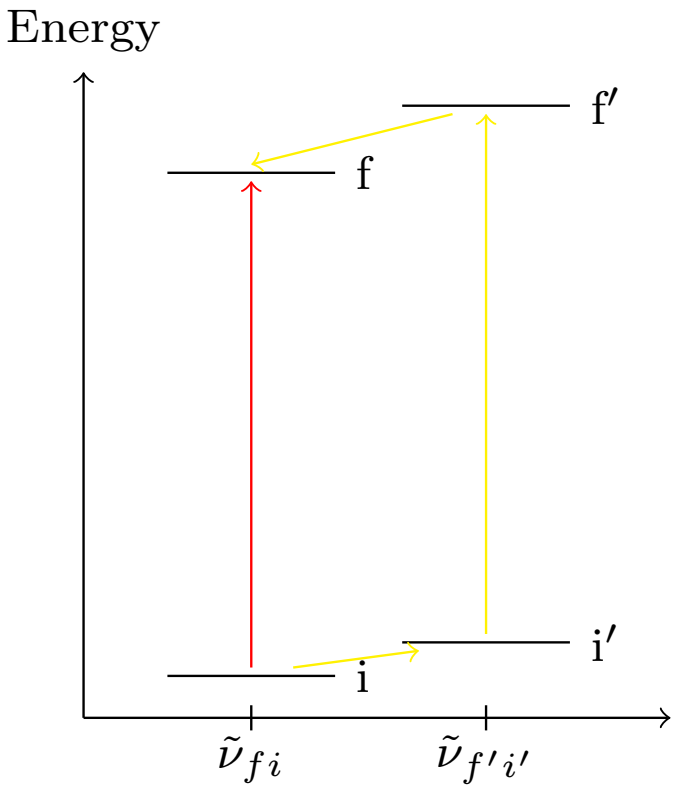

Figure 4.9: Illustration of the overlap of two energy level transitions between two pressure-broadened spectral lines – the so-called line-coupling or line-mixing. A direct transition from i to f′ can be made by absorbing a photon of frequency ν_{fi} (red path). The same path can occur if the molecule at level i is transferred via collision to i′, absorbs a photon of frequency $\nu_{f'i'}$, and is again collisionally transferred from f′ to f.

the process is shown in Figure 4.9. In the presence of radiation, a molecule at level i can be excited to level f by absorbing a photon of frequency ν_{fi}, giving a spectral absorption line at wavenumber $\tilde{\nu}_{fi}$ = (E_f - E_i)/hc. It can also be excited by collision from i to i', then be excited to level f' by absorbing a photon of frequency $\nu_{f'i'}$, and finally relax by collision from f' to f. This second path from i to f *via* i' and f' shows that a molecule initially on level i can contribute to the absorption line at wavenumber $\tilde{\nu}_{f'i'}$, through population transfers induced by collisions. The reverse path is also possible.

The importance of line-mixing is still a subject of significant study. The most noticeable effects of line-coupling are observed in the Q-branches of CO_2 in the far infra-red, between 4 and 17 μm (Strow and Reuter, 1988; Rodrigues et al., 1999). This band has been the primary focus of line-coupling studies due to CO_2's presence in the atmospheric window and its importance to the overall radiative balance of the earth. It has been shown that neglecting line-mixing in strong CO_2 absorption bands leads to significantly erroneous calculations of the absorption coefficients (Strow and Reuter, 1988; Rodrigues et al., 1999). Thus for accurate modelling in the infra-red using the updated SASKTRAN model, it is of primary interest to incorporate line-coupling effects into the spectral line calculations. However, this lies beyond the scope of this thesis.

Studies from Kochel et al. (1997) and Hartmann et al. (2009) have shown the necessity in including line-coupling when in the vicinity of CO_2 branches. Using only pure Voigt line shapes was shown to result in a factor of 2 overestimation of absorption coefficients in the Q-branch wing near 721.7 cm^{-1} (Kochel et al., 1997). In the retrieval of CO_2 densities from measurements at 1.6 and 2.1 μm, it was unambiguously demonstrated that line coupling *has* to be included to achieve accuracy better than 1% on retrieved CO_2 amounts.

This chapter went into significant detail on the principles underlying the physical process of absorption and emission of radiation. The classical derivation of absorption and natural broadening was examined. The remainder of the chapter focussed on absorption from a semi-classical/quantum-mechanical perspective, looking at the processes which determined absorption line positions, strengths, and broadening. The major assumption of LTE and the principle of detailed balance, used in the SASKTRAN model, was justified for typical atmospheric conditions. Lastly, rotational-vibrational spectra of atmospheric molecules were examined. The following chapter will cover the implementation of thermal emissions within the current SASKTRAN model. It will give a high-level description of the computer code involved.

Chapter 5

Implementation of Thermal Emissions in the SASKTRAN Model

> Imagination is the beginning of creation. You imagine what you desire, you will what you imagine, and at last you create what you will.
>
> George Bernard Shaw

The purpose of this chapter is to illustrate the methodology of the SASKTRAN model in solving the full radiative transfer equation. The implementation of the successive orders approach to the solution of the radiative transfer equation will briefly be examined, and the structure of the current release of SASKTRAN will be summarized. With this background, the addition of thermal emissions into the SASKTRAN framework – the bulk of this thesis project – will be discussed in detail.

5.1 The Current SASKTRAN Model

SASKTRAN is a large body of C/C++ object-oriented code, with the primary purpose of using the successive orders approach to solve the radiative transfer equation in a spherically symmetric atmosphere. This code is almost exclusively the result of effort at the University of Saskatchewan Due to the intensity of the calculations, there are many optimizations written into the structure of the code. One of the primary features of the SASKTRAN code structure is the separation of wavelength-dependent and wavelength-independent calculations. Another main feature is the organization of most atmospheric properties into tables, usually dependent on solar zenith angle (SZA) and solar longitude, at a given geographical location and time. The last primary feature of the code is the use of *rays* throughout the code.

This section will provide details of the calculations performed by SASKTRAN and the assumptions and approximations used in its implementation. The main assumptions in the code are,

- approximating the oblate spheroid of the earth using an osculating sphere coordinate system;
- horizontal homogeneity of the atmosphere's properties in spherical shells;
- neglecting refraction and performing straight line tracing through the atmosphere (although curved rays have been added recently to the model);
- the existing code was used primarily for UV-Vis calculations - therefore thermal emissions were neglected, and the only source of radiation was from scattered sunlight.

All final equations listed in chapter §3 are discretized and solved numerically, as no analytical solutions exist for realistic atmospheric conditions.

5.1.1 Ray Tracing and Geometry

Since the model ignores refraction, all geometry and ray-tracing calculations are wavelength-independent, and thus only need to be completed once before moving on to the wavelength-dependent calculations. Since the scattering of solar radiation is the only source in the current model, SASKTRAN traces out roughly 10 000 rays to discretize all possible scattering paths in a given region of the atmosphere. While this is a taxing calculation, it is only performed once per model run, so any number of wavelengths can be examined without having to re-trace photon paths. With each new wavelength, all absorption and scattering coefficients are updated at each spatial grid point. These results are stored in an *optical properties table*.

Osculating Sphere Grid and Climatology

Given an observer and a line of sight (LOS), the SASKTRAN model approximates the oblate spheroid of the earth using spherical geometry. The best choice of sphere is the one that closest matches the curvature of the IAU1976 reference geoid (the SASKTRAN default) at the reference point on the earth. The reference point is determined from the latitudinal/longitudinal average of points along the LOS. The local zenith direction is defined as the unit vector that points from the centre of the sphere through the reference point.

Once the osculating sphere is chosen, the atmosphere is defined by spherical cells of variable thickness that are concentric with the original osculating sphere. *Cells* are defined as the layers of finite thickness, whereas *shells* are the spherical boundaries of the cells. While the cells can be any thickness, the default is to define the atmospheric cells as 1000 m thick from 0 to 100 km. In each spherical cell, all atmospheric properties are assumed homogeneous regardless of their absolute position. This essentially creates a one-dimensional atmosphere. However, source terms in the same cell do *not* have to be the same, as the solar geometry is different at each point in a cell. Thus the geometry of the model remains fully three-dimensional.

The model's user interface allows input of height profiles of atmospheric temperatures and molecular densities. With no input, SASKTRAN defaults to neutral density and temperature profiles obtained from the European Centre for Medium-Range Weather Forecasts (ECMWF) (Woods, 2006). The input of height profiles again relies on the assumption of horizontal homogeneity, which for most circumstances, is a reasonable assumption, as the atmosphere is typically well-mixed horizontally. Situations where this fails would be in limb geometry measurements where the satellite is looking into the ozone hole - development is under way to address this problem.

Horizontal homogeneity allows for many optimizations within the model. With this assumption, it has been shown that the multiple scatter source term varies smoothly with solar zenith angle at a constant altitude (Griffioen and Oikarinen, 2000). This fact can be utilized by computing the multiple scatter source terms on a discrete grid spanning the range of solar zenith angles, and interpolating the source term along each ray when necessary, as opposed to computing the multiple scatter source term at every point along each ray, which would be very computationally intensive. This will be explained in detail in section §5.1.3.

Paths Through Spherical Cells

Rays are traced using simple sphere-ray intersection geometrical calculations. These intersections are computed at each cell boundary, thus dividing each ray up into segments within each cell. These segments represent the numerical discretization of the line integral in equation 3.32, each segment having length $ds \rightarrow \Delta s$. Each segment has uniform atmospheric properties - all height-dependent quantities are stored for the centre of the cell. Varying the cell thickness thus has an effect on the accuracy of the computed integrals - however, for most situations, the default value of 1000 m is sufficient.

5.1.2 Calculation of Optical Properties

All optical properties of the SASKTRAN model are wavelength-dependent. The optical properties for each calculation are stored in a top-level class, the *optical properties table*. Conceptually, any number of atmospheric species can be added to this table. Each molecular species is of the class type *skOpticalProperties_**MoleculeName***, and is completely customizable in its absorption and scattering properties, and requires a corresponding climatology to compute its correct effect on the atmosphere.

Optical Depth

The optical depth defined in equation 3.17 is approximated using the LOS segments through each cell,

$$\tau(s_2, s_1) = \int_{s_2}^{s_1} k(s)\, ds \approx \sum_{i=0}^{n} k_i\, \Delta s_i. \tag{5.1}$$

Here, the optical depth of a given LOS is measured from s = s_1 to s = s_2, and the LOS intersects n atmospheric cells. Each i-th cell has path length Δs_i, and uniform extinction k_i. In limb geometry, the line of sight will intersect a spherical cell twice - thus Δs_i is the total path length through the cell.

The calculation of extinction in each cell is performed as a sum of the scattering and absorption cross sections and the density at that altitude,

$$k_i = \sum_{j=0}^{N} n_{ij}\, (\sigma_{abs_{ij}} + \sigma_{sca_{ij}}), \tag{5.2}$$

where the summation is over all N molecules at the i-th altitude. The model employs symmetry wherever possible to reduce the number of computations - the optical depth at some

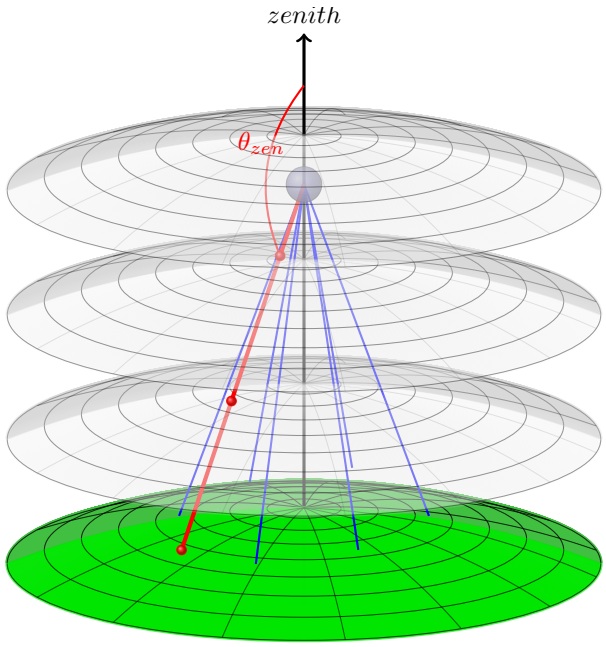

Figure 5.1: The optical depth of some point in the atmosphere at a given zenith angle. Symmetry in the azimuth about the zenith direction can be utilized to avoid re-computation of this optical depth for all azimuth angles. Here, the optical depth of the red ray is calculated through the spherical shells, and re-used for all azimuthally-distributed rays at the same zenith angle (blue).

point in the atmosphere at a given zenith angle is azimuthally symmetric about the zenith, assuming the horizontal homogeneity of the atmosphere and ground (see Figure 5.1).

The calculation of the absorption and scattering cross sections is dependent on the type of molecule. For example, the Rayleigh scattering cross section is simply calculated using the formula in equation 3.24. Other calculations – such as those of the ozone absorption cross section – are much more complex, and often make use of data tables to parametrize things like temperature,pressure, and wavelength dependence.

The optical depth of a ray segment through a given cell is derived assuming a linear variation of the extinction from the bottom cell boundary to the top cell boundary. This is an important improvement in accuracy of the numerical integral.

Scattering Calculations

The most complex calculations lie in calculations of the scattering cross sections and phase functions. Mie scattering cross sections (equation 3.26) and numerous ice-crystal cross-sections are computationally intensive, and make use of legacy Fortran code to compute their scattering coefficients. The phase function requires additional computation - for polarized light, this means calculating a 4×4 tensor and performing numerous matrix multiplications. Fortunately, SASKTRAN's default capabilities are for unpolarized light, drastically reducing computation time.

5.1.3 Source Terms and Instrument Line of Sight Radiance

Once all the optical properties of each shell are calculated for a particular wavelength, the radiance along a line of sight can be determined by finding the value of the source function, $\mathrm{J}_i(\mathrm{s})$ (equation 3.33) at each ray segment and integrating them according to equation 3.32,

$$I(0, \hat{\Omega}) = I(s, \hat{\Omega}) e^{-\tau(s)} + \epsilon B[T(s)] e^{-\tau(s)} + \int_s^0 J(s', \hat{\Omega}) e^{-\tau(s')} ds', \tag{5.3}$$

where s is the end of the line of sight, either terminated at the end of the atmosphere or at the ground. Since the line of sight is divided up into segments, each segment contributes to the final line of sight radiance. The radiance contribution ΔI from a segment running from $\mathrm{s} = \mathrm{s}_0$ to s_1 is then,

$$\Delta I = \int_{s_0}^{s_1} J(s)\, e^{-\tau(s)}\, ds, \tag{5.4}$$

and expressing the optical depth as a sum of the optical depth from the observer to the shell plus segment optical depth, $\tau = \tau(s_0) + \Delta\tau(s)$, and substituting $l = s_1 - s_0$, we obtain,

$$\Delta I = e^{-\tau(s_0)} \int_0^L J(s)\, e^{-\Delta\tau(l)}\, dl, \tag{5.5}$$

where L is the length of the segment. For the given assumption of homogeneous optical properties in a cell, we can assume the both the extinction, $\bar{k}$, and the source function, $\bar{J}$, are constant along the segment path. Thus the radiance from a particular cell segment is easily determined,

$$\Delta I = \bar{J}\, e^{-\tau(s_0)} \left[\frac{1 - e^{-\bar{k}\, L}}{\bar{k}}\right], \tag{5.6}$$

where we utilized $\Delta\tau = \bar{k}\, l$ to easily perform the integration. SASKTRAN currently chooses the mid-path-length value of J and k to represent the homogeneous cell values $\bar{J}$ and $\bar{k}$. The real difficulty of the calculations lies in determining the value of the source function. The successive orders approach taken by SASKTRAN attempts to simplify the integrals by dividing the sources into light that has been scattered once, scattered twice, and scattered three or more times (see section §3.3.4). Recent developments allow the source term to vary in a quadratic fashion, thus altering equation 5.6, and improving accuracy in the overall radiance term.

Single Scatter Source Terms

The source terms for one scattering event are calculated at each point in the atmosphere defined by the solar zenith angle table. The table is fully configurable by the user, but defaults to 0.5^o spacings based on the horizontal span of the instrument line of sight, with profiles from 0 to 100 km in 1000 m steps. At each of the points in this grid, the optical

depth to the top of the atmosphere in the solar direction is calculated, to determine the attenuation of the solar flux, initially given a value of 1.0, to each atmospheric scattering point. The exponent of the optical depth, the *transmission*, is the resulting quantity stored in the *solar transmission table*.

Once a line of sight passes through the atmosphere, the attenuated solar flux at each ray segment is multiplied by the phase function and the single scattering albedo. This value now forms the single scatter source function for this cell as defined in equation 3.43. Figure 5.2 illustrates this table.The single scatter source function is also computed at the ground without approximation, with the assumption of Lambertian scattering (see equation 3.44).

Source Terms from Light that has Been Scattered Twice

The problem of multiple scattering is a bit more difficult to handle. The recursive nature of equations 3.33 and 3.32, even with medium spatial resolution, becomes very computationally intensive. As mentioned before, SASKTRAN takes advantage of the linear variation of the multiple scatter source function at a given altitude with solar zenith angle. Thus the *diffuse point table* consists of a small number of profiles (with points from 0 to 100 km by default) varying in solar zenith angle of points that calculate the multiple scattering of light. Typically the profiles are distributed evenly with the cosine of the solar zenith angle, although this is configurable.

For second-order scattering events, each point in the diffuse table traces rays in all zenith and azimuth directions through the atmosphere. The wavelength-independent part of SASKTRAN stores indexes relating each point to the next, to avoid having to re-trace the rays every wavelength iteration. There is an important distinction between incoming and outgoing rays for the diffuse points. The incoming rays represent the discretization of the equation 3.46 - the computation of all light that has already been scattered once into a particular point. The incoming rays are distributed according to the configuration in Figure 5.4 with

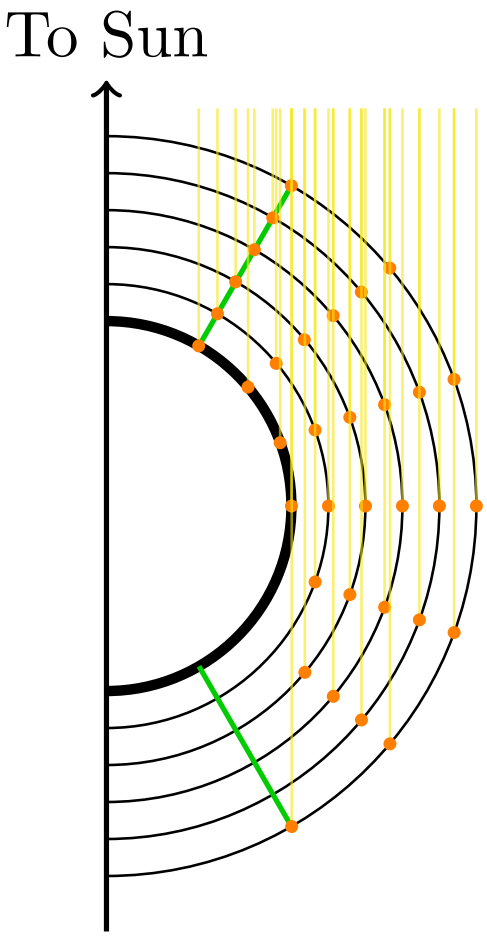

Figure 5.2: First order scattering in SASKTRAN. The table is configured with a maximum and minimum solar zenith angle (green profiles). Light from the sun is attenuated from the atmospheric entry point to the table point. If the solar zenith angle is too large, some portions of the table will be in shadow, and the solar transmission is 0 at those points (the bottom portion of the figure). The model configures the direction to the sun as the global z-axis.

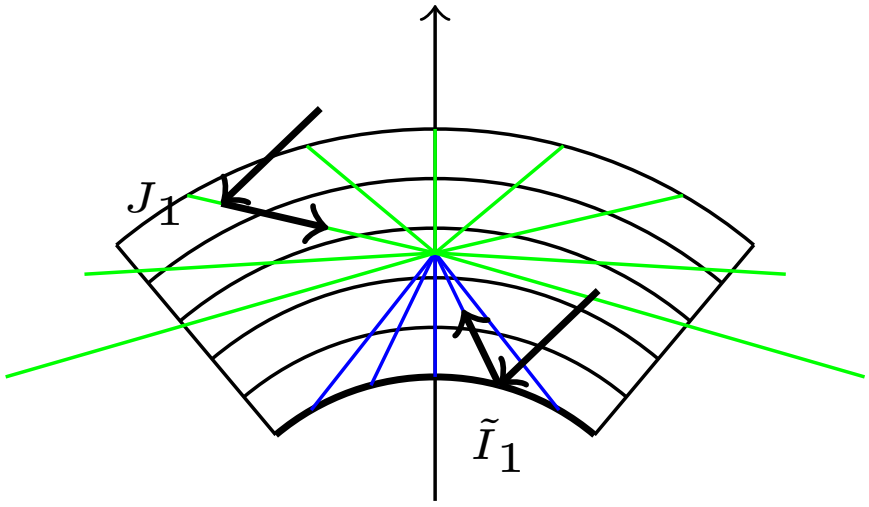

Figure 5.3: Calculation of the second order source term $J_2(s, \hat{\Omega})$. Rays are traced out over the unit sphere; blue rays strike the ground, while green rays exit the top of the atmosphere. At each point along each ray, the incoming radiance from a single scattering event, $J_1(s, \hat{\Omega})$, is computed and attenuated back to the origin. If the ray strikes the ground, $\tilde{I}_1(s, \hat{\Omega})$ is also attenuated back to the ray origin. The total incoming radiance is computed at the ray origin, scattered in all directions, and integrated over solid angle. This is repeated for all incoming rays.

a larger concentration of rays around the local horizon of the point. This is necessary since the radiance field is changes by several orders of magnitude at the local horizon. The reason for this is that the majority of scattered sunlight reaching an atmospheric point has been scattered off of the ground and/or the much thicker lower atmosphere. Once an incoming ray to the point doesn't intersect the ground or lower portion of the atmosphere, there is a much lower probability that sunlight has scattered into the diffuse point. A single incoming ray computes the total single-scatter radiance at the diffuse point, as defined by equation 3.45. This radiance is then scattered in all directions according to the diffuse point's single scatter albedo and phase function. This is repeated for all incoming rays, and results in the outgoing diffuse field at the diffuse point, for second order scattered sunlight. This is illustrated in Figure 5.6. The summation and scattering of input radiances, when repeated for numerous diffuse points, quickly exhausts computing power and memory. Thus the model is typically used with 1-5 diffuse profiles - although 1 is "good enough" for most applications.

Source Terms from Light that has Been Scattered Three or More Times

Calculation of higher order source functions is very similar to the second order scattering term, in that equations 3.49 and 3.50 are used. However, the higher order source functions are *not* calculated by tracing rays and performing the line integrals of the previous-order source function. In the wavelength-independent portion of the model, rays traced between points were catalogued, and the necessary interpolation weights between points was stored, all in a class type called *JIndex*, making for quick access to every point in the table.

Depending on the requested order of scattering, the model iteratively computes the scattering contribution in the diffuse points table. On the first pass, the diffuse points table is initialized with the single scatter table as described in the previous section. That is, when performing the source function line integral in equation 3.38 for each incoming ray to the diffuse point, the only source along the ray is from the single scatter table, as all diffuse points are presently zero (and blackbody emissions are ignored). On the next pass, each diffuse point in the table

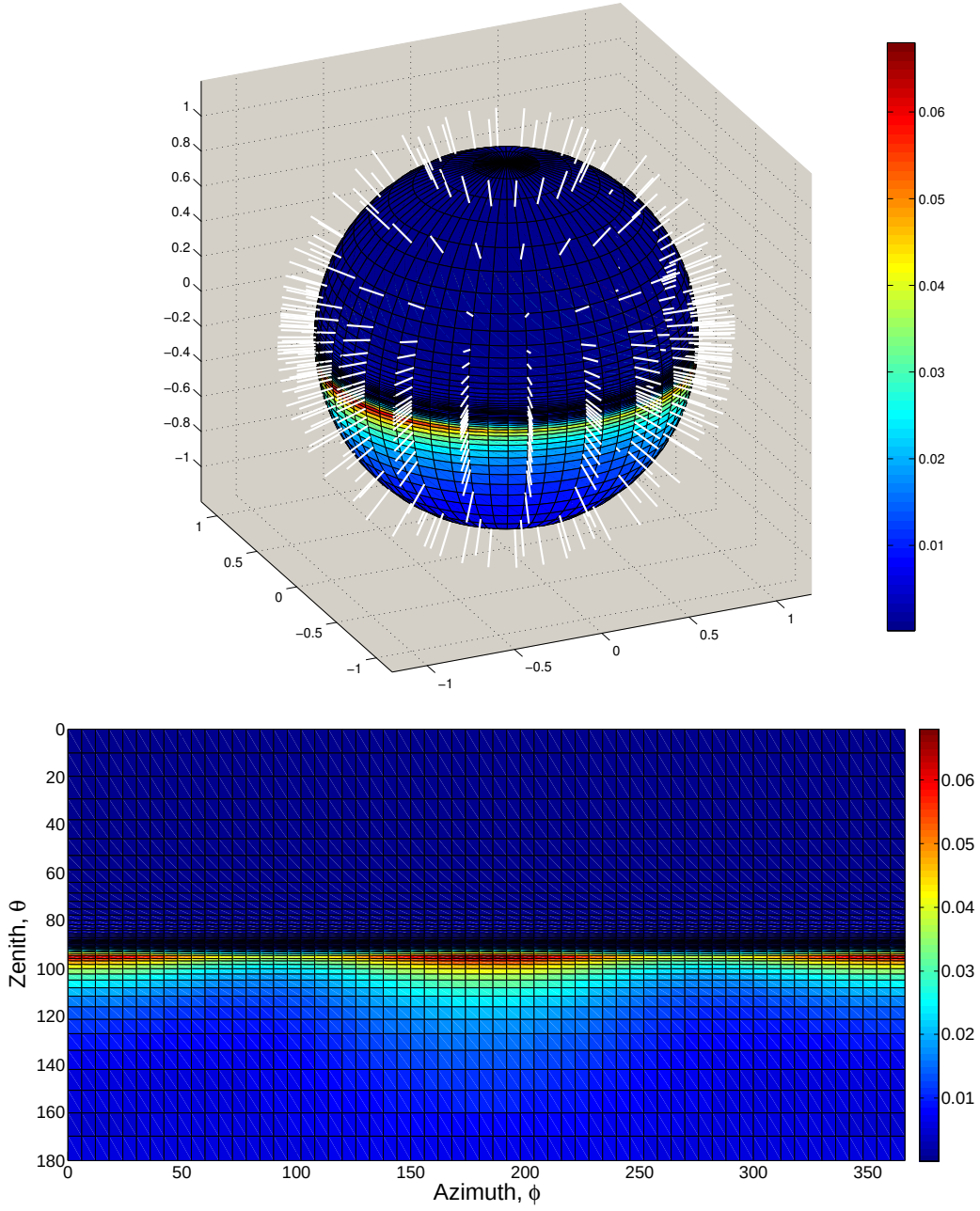

Figure 5.4: [Left] The incoming radiance field coming into a typical diffuse atmospheric point at 25 km altitude and 500 nm wavelength, and albedo of 0 (no ground scatter). Most of the radiation is coming from scattering on the lower portion of the atmosphere. The white lines denote where SASKTRAN samples the incoming diffuse radiance field at - a higher concentration of rays are located around the horizon due to the orders of magnitude change. [Right] The full diffuse field in the figure on the left.

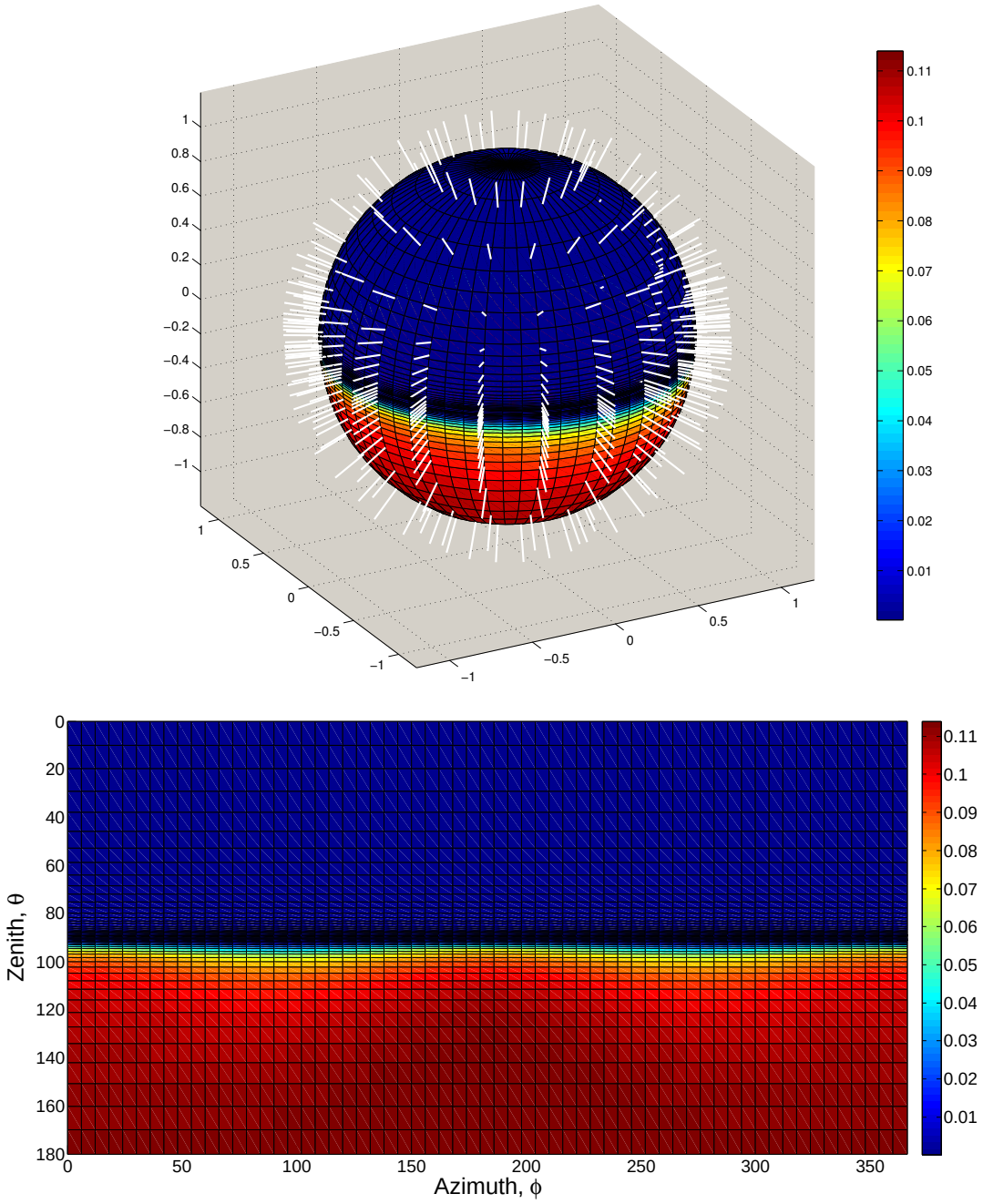

Figure 5.5: [Left] The same diffuse point at 500 nm and 25 km altitude as in Figure 5.4, but with albedo of 1.0. This results in a much larger signal from below entering the point, as there is now a significant signal from ground scattering. [Right] The full diffuse field.

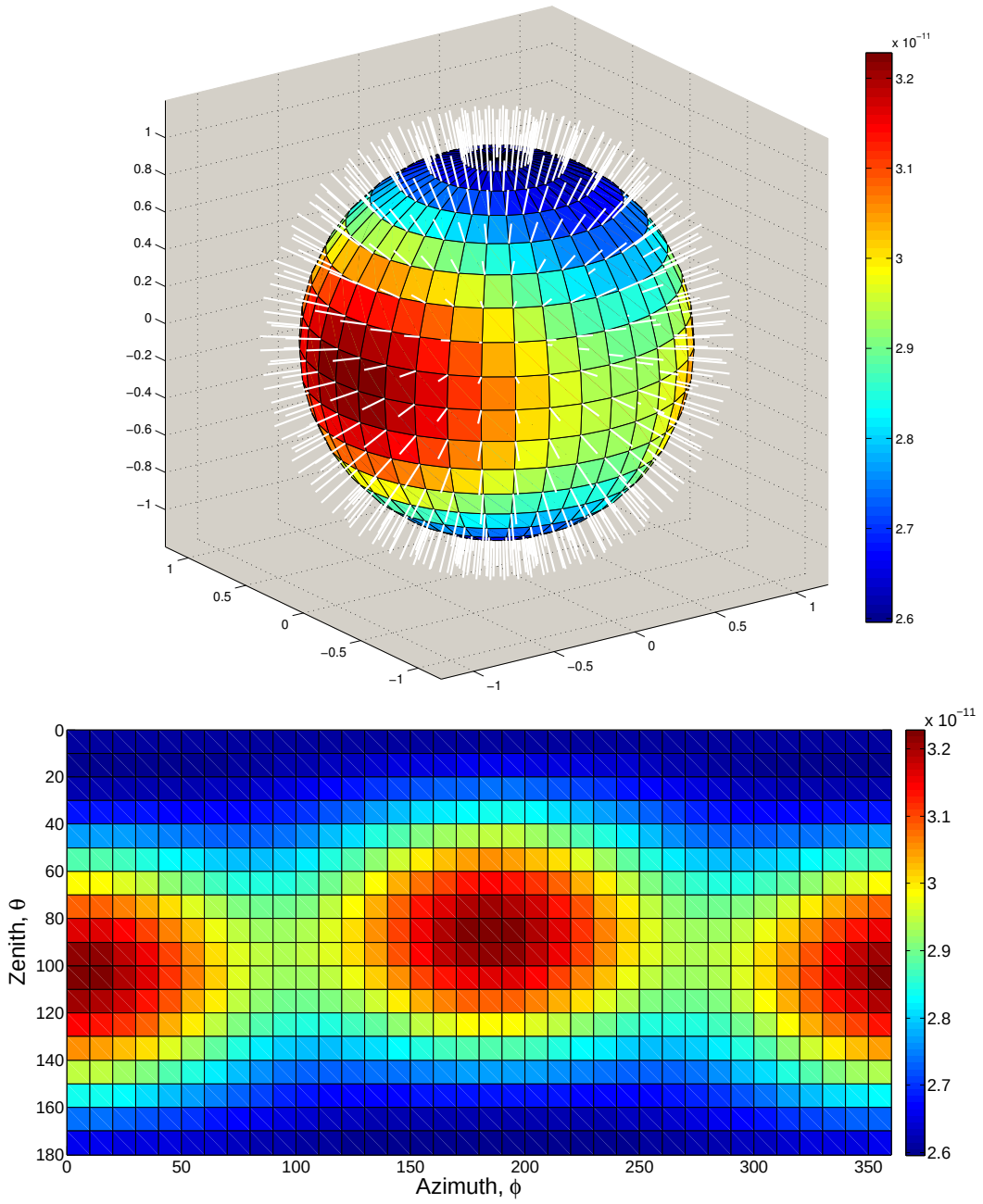

Figure 5.6: [Left] Outgoing diffuse radiance field for the diffuse incoming field of Figure 5.4, at 500 nm wavelength and 25 km altitude. Note the even distribution of outgoing rays. [Right] The full outgoing diffuse field of the left figure.

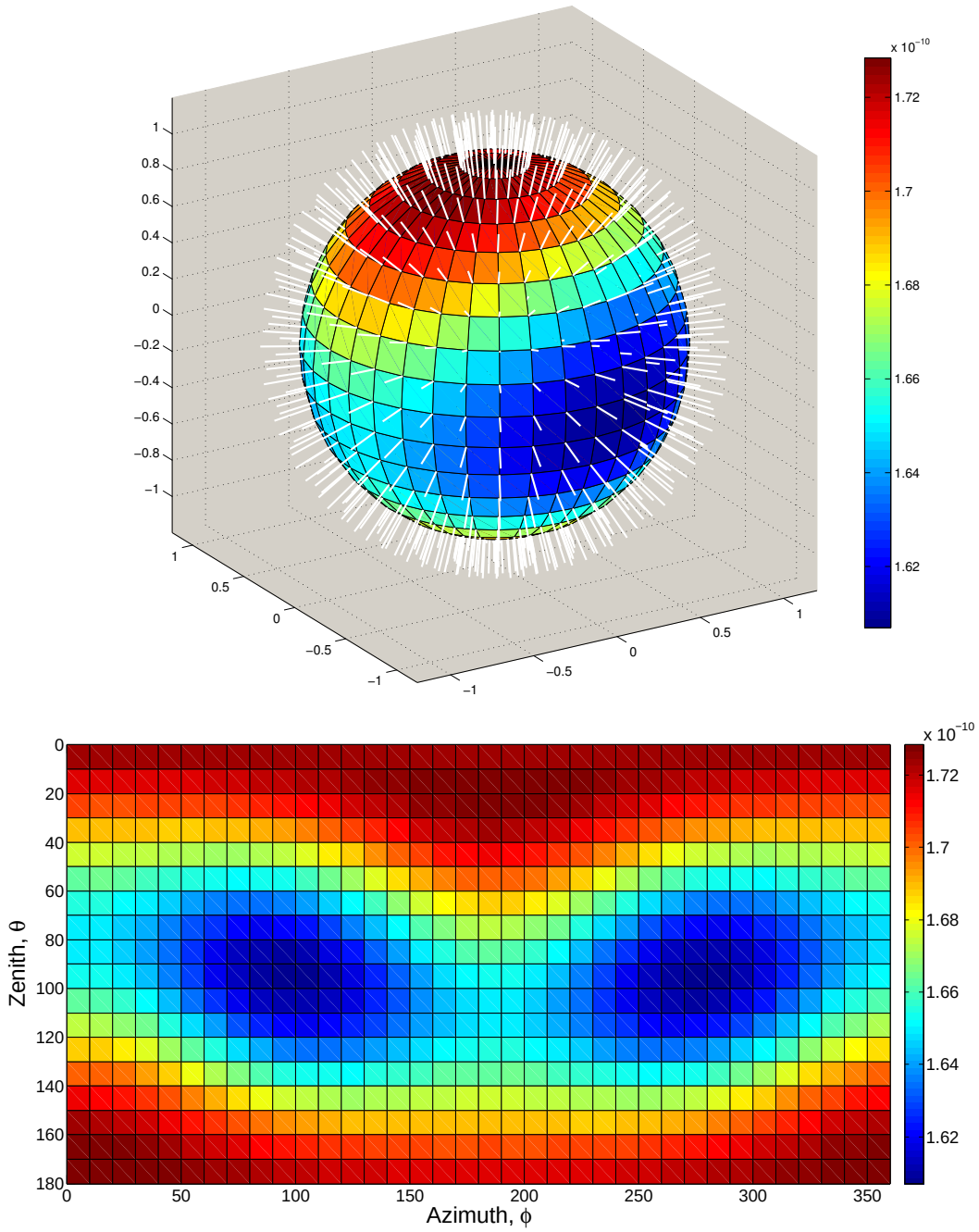

Figure 5.7: [Left] Outgoing diffuse radiance field for the diffuse incoming field at 500 nm wavelength and 25 km altitude with albedo of 1. [Right] The full outgoing diffuse field.

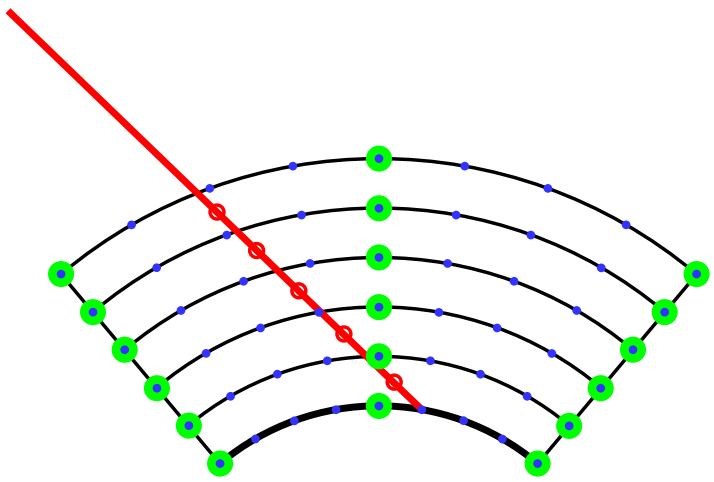

Figure 5.8: Calculation of the final observer line of sight radiance. The single scatter source function (blue) and multiple scatter diffuse source function (green) is interpolated by four nearest neighbours at the centre of each ray segment (red circles) on the line of sight (red), and attenuated back to the observer. It should be noted that the actual grid points are distributed uniformly in cosine of solar zenith angle, not uniformly in solar zenith angle.

has each incoming ray re-evaluated, performing the source function line integral again, but this time in addition to the single scatter sources, their are non-zero diffuse sources along the ray (the computations from the last pass, representing the light that has been scattered twice). This results in source functions of light that has been scattered three times. This process is continued for as many orders of scatter as is necessary for convergence.

The Final Observed Radiance

The final observed radiance is obtained by taking all observer lines of sight provided by the user, and performing the source function line integral (equation 3.38) for each. By this point, the model has calculated the diffuse points table for the necessary order of scatter, and the single scatter table, so all that is necessary is to determine the value of each source function at each segment of the ray. This is shown in Figure **??**.

5.2 The Addition of Thermal Emissions

The model described in the previous sections does not account for thermal radiation from the ground nor the atmosphere. To include this in the model, we had to make one important assumption - *the entire atmosphere is in local thermodynamic equilibrium.* This is a reasonable assumption, though typically only accurate up to roughly 60 - 70 km altitude. Above this altitude, energy levels of molecules are not in equilibrium with the surrounding radiation field, and the assumption of thermodynamic equilibrium breaks down. However, in typical satellite geometry, most measurements are made so that the majority of the signal originates below 50 km altitude, so our assumption is fairly safe - very little radiation originates at high altitudes.

In keeping with the structure of the SASKTRAN model, it was decided to produce a table of the same dimensions as the solar transmission table, into a *thermal emissions table.* The reasoning behind this is that the raw calculation of the blackbody function is simple enough to use a high-resolution table without impacting the calculation time much. All that is needed for the calculation of the thermal emission table is a temperature profile. The table is configured to allow for geographical variation in temperature. Since the blackbody function (equation 3.31) is isotropic, each point in the table only requires one value (in comparison with the diffuse points, which require numerous rays to characterize the directionality of the radiation field), and interpolation between points is accomplished relatively simply.

The fundamental calculation quantity in SASKTRAN is the ray, which is used to integrate all the source functions along its path. With the thermal emissions table in place, it was a simple matter to interpolate the blackbody function at each segment of the ray, multiply it by the absorption coefficient (see equation 5.10), and add it into the integral calculation. The elegance of this is that it allows for the thermal emissions to be scattered multiple times along with the sunlight. Very few radiative transfer models are built to handle the scattering of thermal radiation. Thermal radiation from the ground is handled similarly. The ground

temperature is taken from the temperature profile's value at 0 km, and the emissivity of the ground is provided by the user via text file.

At the beginning of this thesis, the optical properties classes in SASKTRAN were not capable of computing absorption coefficients for most greenhouse gas molecules. Previous work in ISAS was done to utilize the HITRAN spectral database to compute these necessary absorption coefficients.

5.2.1 HITRAN Calculations of Absorption Cross-Sections

The HITRAN (HIgh-resolution TRANsmission) spectral database, in its most recent release in 2012, contains 7 400 447 spectral lines for 47 different molecules. Molecules are also divided into their different isotopes with typical atmospheric abundances. HITRAN stores spectral line strengths as a function of wavenumber. Some molecules, like water vapour, have hundreds of thousands of lines. Given that spectral line strength is a function of temperature (see equation 4.36), the values in HITRAN are stored at a reference temperature of 296 K. To calculate spectral line strengths at any temperature, we utilize equation 4.36. The lower state populations, $n_l(T)$, at some temperature can be determined using the partition function, $Z(T)$, for a molecule,

$$n_l(T) = \frac{N\, g_l\, e^{-\frac{E_l}{k_B T}}}{Z(T)}, \tag{5.7}$$

where E_l is the lower state energy (also stored in the HITRAN database), and g_l is the degeneracy of the lower energy state. With this equation, the fraction $n_l(t)\,/\,n_l(T_{ref})$ in equation 4.36 can be reduced to,

$$\frac{n_l(T)}{n_l(T_{ref})} = \frac{\exp\left(-\frac{E_l}{k_B T}\right)}{\exp\left(-\frac{E_l}{k_B T_{ref}}\right)} \frac{Z(T_{ref})}{Z(T)}. \tag{5.8}$$

HITRAN also stores the values of $Z(T)$ for (almost) all isotopologues, for temperatures ranging from 70 to 3000 K. Thus the value of a spectral line at any atmospheric temperature can be computed from the reference spectral line in the database,

$$s_{lu}(T) = s_{lu}(T_{ref})\,\frac{Z(T_{ref})}{Z(T)}\,\frac{\exp\left(-\frac{E_l}{k_B\,T}\right)}{\exp\left(-\frac{E_l}{k_B\,T_{ref}}\right)}\,\frac{1-\exp\left(-\frac{h\,c\,\nu}{k_B\,T}\right)}{1-\exp\left(-\frac{h\,c\,\nu}{k_B\,T_{ref}}\right)}. \tag{5.9}$$

Because of the sensitivity of the spectral line strength to temperature, it is necessary in the SASKTRAN model to re-compute the spectral line strengths at each altitude. For bands dense in spectral lines, this can significantly increase computation time.

As outlined in section §4.2.2, there is no such thing as monochromatic absorption - there are always some processes at play in the real world to "broaden" the spectral line. Thus, even at wavenumbers where there are no nearby spectral lines, the sum of the wings of far-away broadened lines will cause a certain amount of absorption there (this is actually one of the biggest challenges in molecular spectroscopy - quantifying the effects of spectral lines in their far wings without brute-force computation of broadening of every single line (Ma and Tipping, 1991)). The SASKTRAN model uses Voigt broadening as its default (see equations 4.57 through 4.61).

The real part of the complex error function, k(x,y), is pre-computed and placed into a lookup table. Since x and y represent the wavenumber distance, temperature, and pressure dependence, calculation of broadening effects, even with a lookup table, are extremely slow. To calculate the cross section at any wavenumber, ν, the code is given a wavenumber range of lines that can contribute to the absorption – 25.0 cm^{-1} is typically used. For most applications this is sufficient, but the cumulative effect of further dense spectral line regions sometimes cannot be ignored, especially when near water vapour bands (Ma and Tipping, 1991; Liou, 1980). Figure 5.9 illustrates the basic broadening calculation. For each line located at ν_{0i} within the window, the broadening, $\phi_V(\Delta\nu)$, is computed for the wavenumber distance, $\Delta\nu = |\nu - \nu_{0i}|$, and the temperature and pressure. To compute the total absorption cross

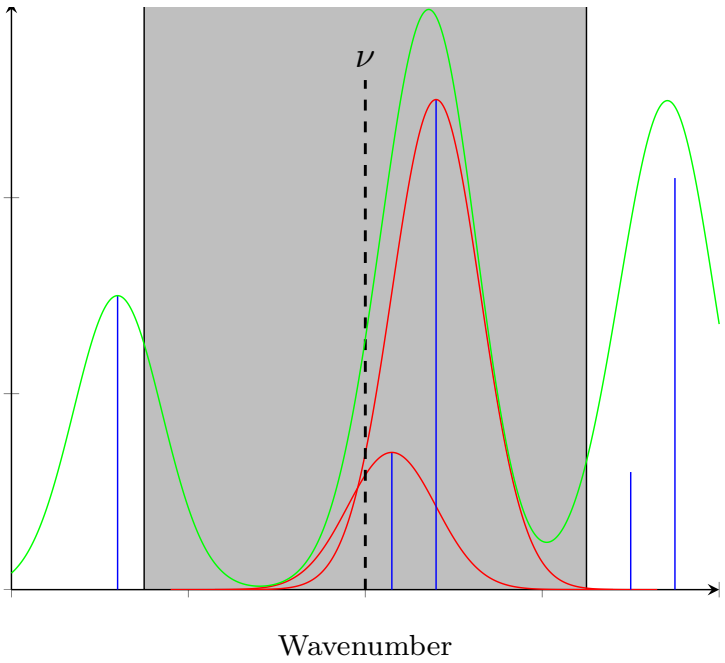

Figure 5.9: Cross section calculation at wavenumber ν from the spectral lines in the window (shaded gray). All lines outside the window are ignored. The resulting cross section calculated over all wavenumbers is shown in green. Notice the low point on the graph to the left of ν - even though there are no spectral lines near it, the cross section is still non-zero.

section at ν, the contribution from all N spectral lines in the window is summed,

$$\sigma_{abs}(\nu) = \sum_{i=0}^{N} s_{lu,i}(T)\, \phi_V(\Delta\nu, T, p), \tag{5.10}$$

where the temperature and pressure dependence was listed in the arguments for clarity, and the temperature-modified spectral line strength was used (equation 5.9). For thousands of lines within a spectral window, and 50 - 100 altitudes with varying temperature and pressure, the computations can be very intensive.

Figure 5.10 illustrates the effects broadening has at different altitudes on the cross sections. At low altitudes, the spectral lines are much wider - as they are dominated by Lorentz (pressure) broadening. At higher altitudes, the lines are much narrower, due to a combination of Lorentz and Doppler broadening.

This chapter summarized the inner workings of the current SASKTRAN model in its goal of solving the radiative transfer equation. The assumptions made by the model to optimize the calculation were summarized. The method for calculating thermal emissions within the model was introduced - while the calculations of the blackbody function were shown to be very simple, calculation of the absorption cross sections of molecules from the HITRAN database was shown to carry a heavy computational load. In the next chapter, calculations from the updated SASKTRAN model with thermal emissions will be compared both with satellite measurements and other radiative transfer model calculations, in the near infra-red (below 2 μm) and mid-to-far infra-red (above 5 μm).

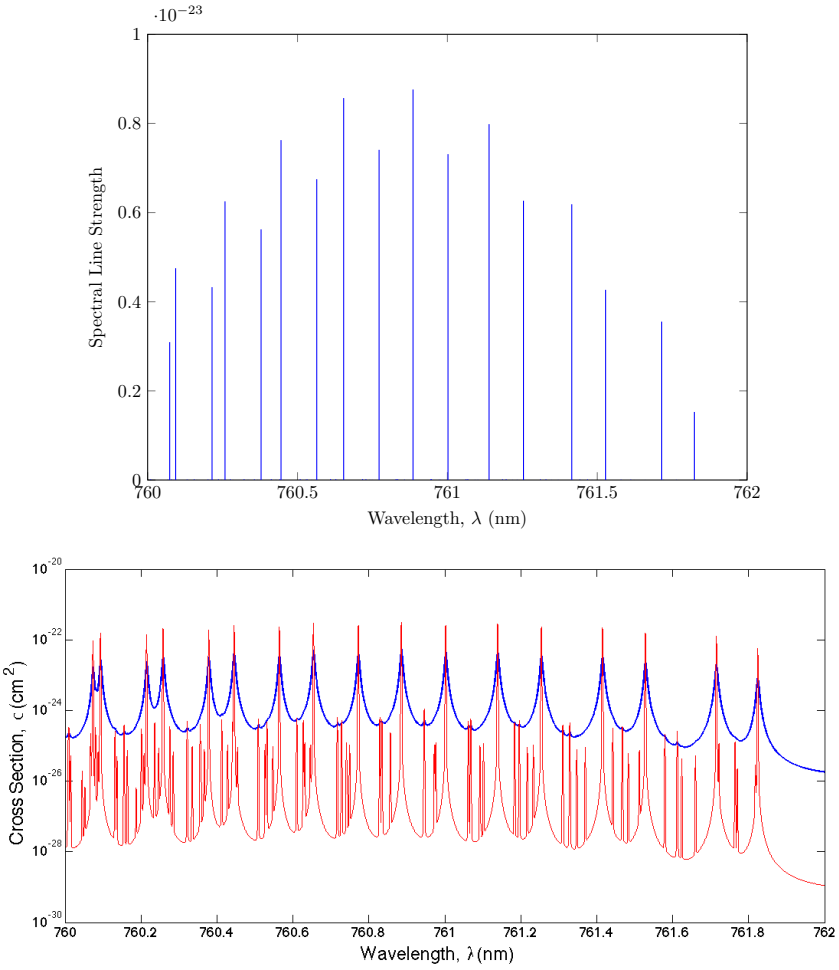

Figure 5.10: Raw un-broadened spectral lines for O_2 from 760 - 762 nm (left), and the corresponding cross-sections at 0 km (blue) and 50 km (red) altitude, using typical atmospheric temperature and pressure profiles. The cross sections at lower altitudes are much broader, while cross sections at high altitudes are narrow, but have higher magnitude peaks.

Chapter 6

Verification

> The great tragedy of science - the slaying of a beautiful hypothesis by an ugly fact.
>
> Thomas Huxley

The purpose of this chapter is to verify that the SASKTRAN model, with the addition of thermal emissions, remains capable of accurately modelling atmospheric radiance. Since SASKTRAN has been shown to model atmospheric radiance in the UV-Vis region accurately in previous work (Bourassa, 2007), it remained to show that the addition of thermal emissions did not affect SASKTRAN's accuracy in the UV-Vis region, while accurately modelling the infra-red region. By verifying the model's ability in both regions, SASKTRAN's ability to model the mid infra-red region – where solar and thermal contributions are approximately equal – is shown.

Verifications are made by quantitative comparisons with another well-verified radiative transfer model, LBLRTM (Clough et al., 2005). Comparisons against satellite measurements from GOSAT and IASI, and with the ground-based instrument, E-AERI (Mariani et al., 2012) are also made with SASKTRAN, although due to the difficulty in matching the exact measurement conditions, they remain strictly qualitative.

6.1 Preliminary Modelling

Before any attempt at modelling satellite measurements or other radiative transfer model calculations was made, it was necessary to look at a number of cases that were easier to model. The first was a simple test case with a single absorbing/emitting species present in the atmosphere. The second made use of measurements from a ground-based Fourier transform spectrometer, E-AERI, located in Eureka, Canada. This instrument operated purely in the infra-red, and only looked straight up in the air, meaning there was very little radiation from the ground entering the instrument, so the measurements are very sensitive to atmospheric conditions. In addition, the measurements included pressure, temperature, and water vapour profiles on a twice-per-day basis, allowing precise modelling of the radiance.

6.1.1 Simple Test Case

A simple case was set up with only one absorbing molecule, carbon monoxide, present in the atmosphere at a constant temperature, T_A, while the ground was at another constant temperature, T_G. The observed radiance for a nadir-viewing observer at 40 km altitude was performed in the wavenumber range 2050 - 2056 cm^{-1}, an area of strong CO absorption. This calculation was performed for two regimes – (i) where the ground temperature T_G = 288.2 K is higher than the atmospheric temperature T_A = 250 K, and (ii) T_G = 250 K is lower than T_A = 288.2 K. The results are shown in Figure 6.1.

The radiation emitted by the ground is modelled as a pure blackbody spectrum, whereas radiation in the atmosphere only is absorbed/emitted at frequencies of molecular spectral lines (neglecting broadening effects). Therefore if the ground is at a higher temperature than the atmosphere, we will observe a blackbody spectrum at the ground temperature with decreased radiance at the spectral line frequencies of the molecules present – this is an **absorption spectrum**. For a warmer atmosphere, the blackbody spectrum of the ground

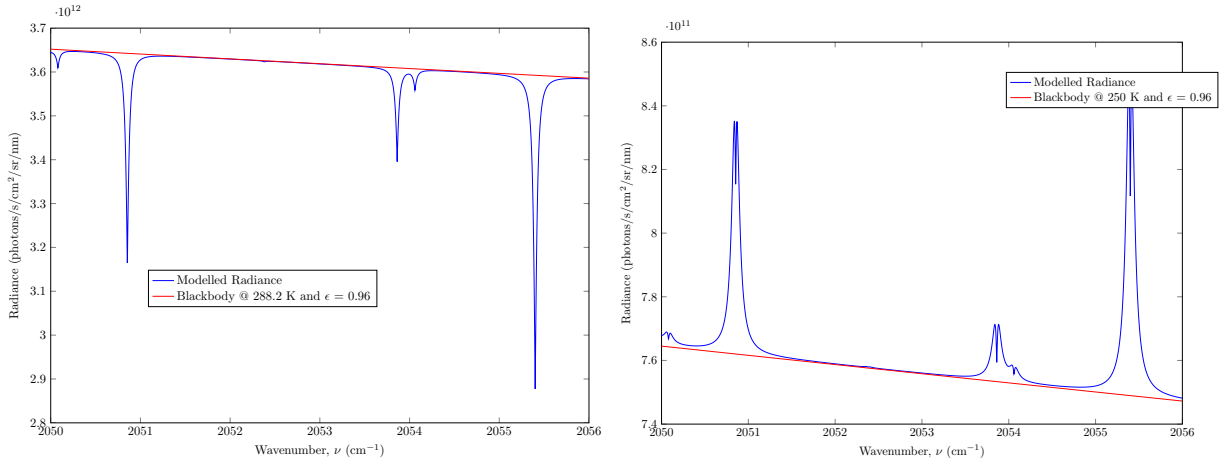

Figure 6.1: [Left] Absorption spectrum of a CO band for when the ground was warmer than the air. The blue line is the spectrum, and the red line is an equivalent black body spectrum at the ground temperature of 288.2 K. [Right] Emission spectrum of a CO band for when the ground, at 250 K, is cooler than the air. Here, emission by the atmosphere at the spectral lines is observed on top of the ground radiance, which is a black body spectrum at 250 K. Notice that some absorption still occurs at the centre of the emissions, since this is where the spectral line has its strongest absorption.

is still observed, but at the spectral line frequencies there is increased radiance – this is an **emission spectrum**. In a real atmosphere with multiple atmospheric layers of different temperatures, pressures, and molecular content, the situation is more complicated, but the principle remains the same.

When $T_G > T_A$, the radiation from the ground "washes out" any emission from the atmospheric CO, and we only see the blackbody spectrum of the ground, with absorption features at the CO spectral lines. However, if $T_G < T_A$, we still see the blackbody spectrum of the ground, but since its emission is lower, we now see emission from the atmosphere *on top* of the ground spectrum, at the CO lines. The absorption and emission spectrums occur just as expected – in areas where there is no molecular absorption, the radiance follows the blackbody spectrum of the ground temperature (shown in red). The results of the calculations are shown in Figure 6.1.

6.1.2 E-AERI Ground-Based Measurements

More rigorous verification of the SASKTRAN model began with comparing against detailed ground-based measurements from the Extended-range Atmospheric Emitted Radiance Interferometer (E-AERI) (Mariani et al., 2012), a Fourier transform spectrometer based in Eureka, Canada. The instrument provided a good first comparison for SASKTRAN's thermal emissions capabilities, as the instrument solely measures infra-red radiation emitted by the atmosphere between 400 and 3000 cm^{-1}, allowing us to ignore solar contributions. In addition, the instrument's upward viewing in this region means that there is little to no radiation from the ground scattered into the instrument. Therefore, it provided an excellent base to verify accurate modelling of molecular radiation.

Also provided with the day-by-day radiance measurements were twice-daily measurements of water vapour and temperature from 0 to 30 km in 10 m steps (an example is shown in Figure 6.2). The reason for the ultra-fine grid is due to the sensitivity of the signal – the radiance emitted by the atmosphere is relatively small since there is no strong ground emission visible, and fine changes in temperature or pressure at certain altitudes have significant effects on the observed radiance. Thus the measurements would be a good test of SASKTRAN's accuracy.

Simulations for December 8, 2008 were made for a ground instrument looking straight up at an altitude of 610 m, due to the altitude of the E-AERI station. Water vapour and temperature profiles were utilized from the E-AERI data for the same day, pressure was derived from ECMWF data, and all other profiles (such as CO_2 and CH_4) were obtained from atmospheric data in the MODTRAN report (Kneizys et al., 1996) for high latitude winter.

As an exercise of the sensitivity of the modelled radiance to the water vapour and temperature profiles, the instrument altitude was varied between 0 km and 20 km. The motivation for this is two-fold. Firstly, varying the instrument height will cause the observer to see either an

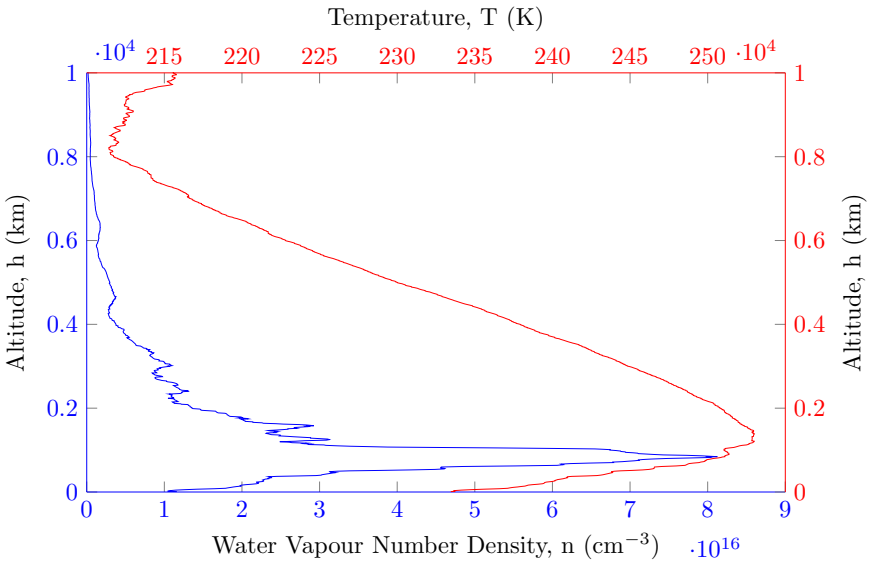

Figure 6.2: Typical water vapour density and temperature profile used with E-AERI. This particular measurement set was for December 08, 2008. Notice the low-altitude temperature inversion, and a water vapour peak at 800 m below the temperature peak at 1.3 km.

absorption or emission spectrum, depending on if the air immediately above the instrument is warmer than air at a greater altitude. Secondly, it gives insight into the optical thickness of the atmosphere at each altitude. Figures 6.3 and 6.4 show initial comparisons with the E-AERI data.

Figures 6.3 and 6.4 show – in addition to the agreement between the model and measurement – the effect of varying the altitude of the instrument. With the instrument at 20 km, the atmosphere is very thin, and the background radiance is essentially zero since the temperature decreases with altitude, so a very weak emission spectrum is observed. This occurs in both bands.

In the 6 μm water vapour band, placing the instrument at its correct altitude of 610 m shows a very good qualitative agreement with the E-AERI measurement. The precision of the model is revealed when the instrument is moved down 110 m to 500 m altitude – the radiance is reduced considerably. This shows that the atmosphere at this altitude up to the

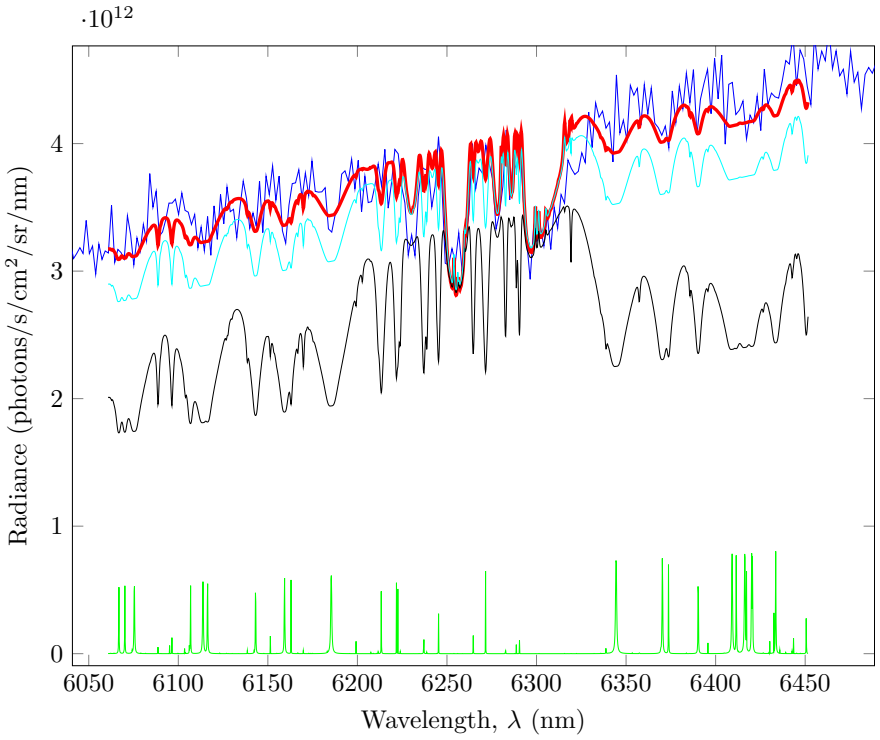

Figure 6.3: Comparison of modelled radiance around 6 μm to E-AERI radiance on December 8, 2008. The height of the station was varied to observe different emission and absorption spectra. Blue - measurement, red - 610 m, cyan - 500 m, black - 10 m, green - 20 km.

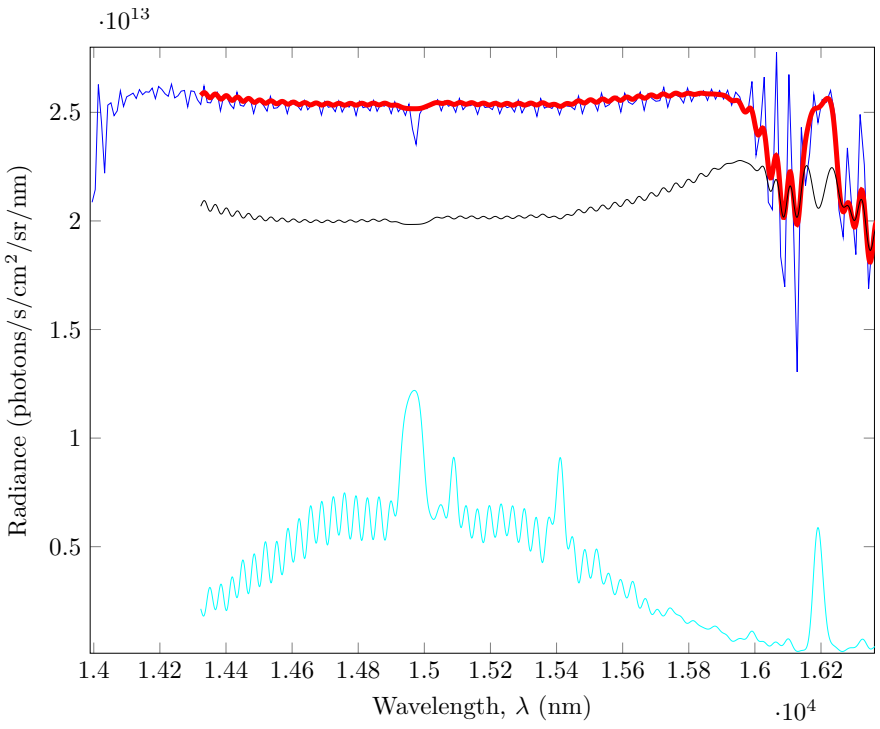

Figure 6.4: Comparison of modelled radiance around 15 μm to E-AERI radiance on December 8, 2008. The height of the station was varied to observe different emission and absorption spectra. Blue - measurement, red - 610 m, black - 500 m, cyan - 20 km, blue - measurement.

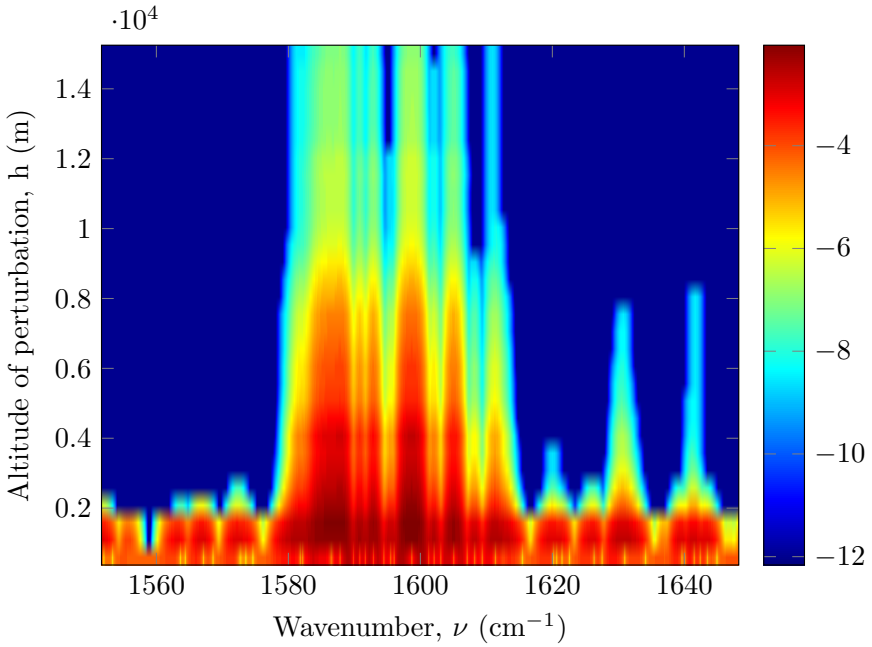

Figure 6.5: Sensitivity of radiance to change in water vapour density at various altitudes. The scale is $\log_{10}$ of the relative difference (test - base)/base.

water vapour/temperature peaks is optically thick, and the strongest emissions around this peak quickly become absorbed.

When the instrument is placed at 10 m altitude, below the low-altitude temperature and water vapour inversions between 100 and 150 m (see Figure 6.2), an emission spectrum is observed. This is because the atmosphere through which the instrument is looking is optically thin compared to the temperature/water vapour peak at 100-150 m. Thus the radiative emissions from the peak reach the observer without getting attenuated significantly by the absorbing atmosphere.

The next study performed was on the effect of height resolution within the radiative transfer model. The provided data for temperature and water vapour profiles were given in 10 m height steps, corresponding to balloon instrument measurements taken twice daily (Mariani et al., 2012). Different grid resolutions within the model were used, ranging from 1 m to 1 km - better grid resolutions leading to more accurate interpolation of the data when called

upon by the optical properties table in the radiative transfer calculation. Best results were obtained for grid resolutions between 20 m and 50 m. Decreasing the step size below 20 m gave no significant return in accuracy when comparing the modelled radiance against the E-AERI measurement. The 20-50 m optimal step size thus makes a statement about the minimum thickness where the atmosphere becomes optically thick.

Given the geometry of the calculation, the necessity of a high vertical resolution makes sense. Looking straight up from a ground location means the observer sees the densest portion of the atmosphere first, so the atmosphere quickly becomes optically thick. If the grid resolution is too large, the lower portions of atmosphere will be calculated as optically thick, and radiance from higher layers will not be seen. By reducing the spacing, optically thick and thin regions of the atmosphere become apparent, and the overall radiance is increased. This was more apparent in the water vapour band at 6 μm than the CO_2 band at 15 μm, owing to the more "interesting" vertical structure of water vapour. Increasing the resolution in the CO_2 band reveals no fine vertical structure, as CO_2 is well-mixed in the atmosphere.

Water vapour, on the other hand, has a great deal of lower atmosphere structure, and is very sensitive to the grid spacing. Given this sensitivity, as well as the sensitivity to observer altitude (see Figure 6.3), it was deemed valuable to perform a perturbation test on the water vapour band. The order-of-magnitude study was performed by increasing the water vapour density by 10 % at a single altitude ranging from 0 to 20 km, and observing the resulting change in radiance from the baseline calculation.

The result is displayed in Figure 6.5, which illustrates sensitivity around the spectral lines of water, and peaking between 1 and 2 km. Given that the altitude of the station was at 610 m, and the temperature peak and water vapour peak were 1300 m and 800 m, respectively, it makes sense that a change in density at these altitudes affects the radiance the most. Radiance from altitudes above are mostly absorbed as the atmosphere is optically thick to the atmosphere at the 1-2 km range to the instrument.

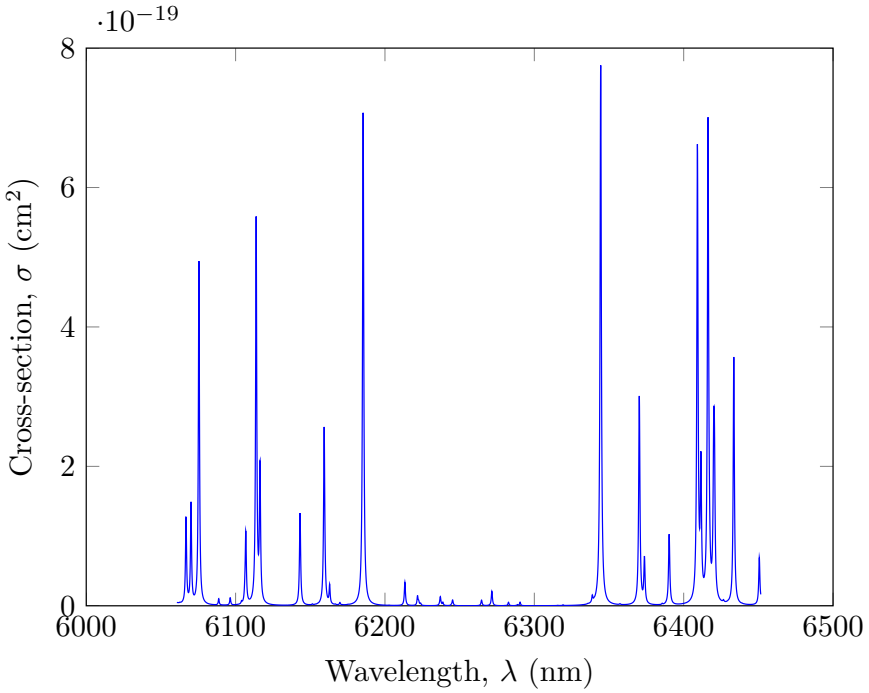

Figure 6.6: Spectral absorption lines of H_2O in the 6 μm band. Notice the gap of no absorption lines.

Another interesting test of the sensitivity of the model was to observe the effects of additional isotopes and spectral window width. Molecules have various naturally occurring isotopes, each with their own absorption characteristics. For instance, water vapour's primary isotope, $H_2{}^{16}O$, accounts for 99.7317% of all natural water vapour, while its second most abundant isotope, $H_2{}^{18}O$, accounts for 0.199983%. Excluding less-abundant isotopes from a calculation can increase speed, but may be costly to the accuracy of the calculation, depending on the frequency band analyzed. Spectral window width – graphically shown in Figure 5.9 – determines how many broadened absorption lines are "seen" at a given wavenumber. The default is 25 cm^{-1} width is the default, but in dense spectral absorption bands, this is not always sufficient, as the cumulative effect of hundreds of thousands of broadened lines beyond 25 cm^{-1} leads to an underestimation of the absorption coefficient at a given wavenumber.

Figure 6.7 illustrates the cumulative effect of including more lines into a band where there are few absorption lines, but many outside the band (refer to figure 6.6). The default calculation of this band (blue) used the primary isotope of water vapour and 50 cm^{-1} on either side of

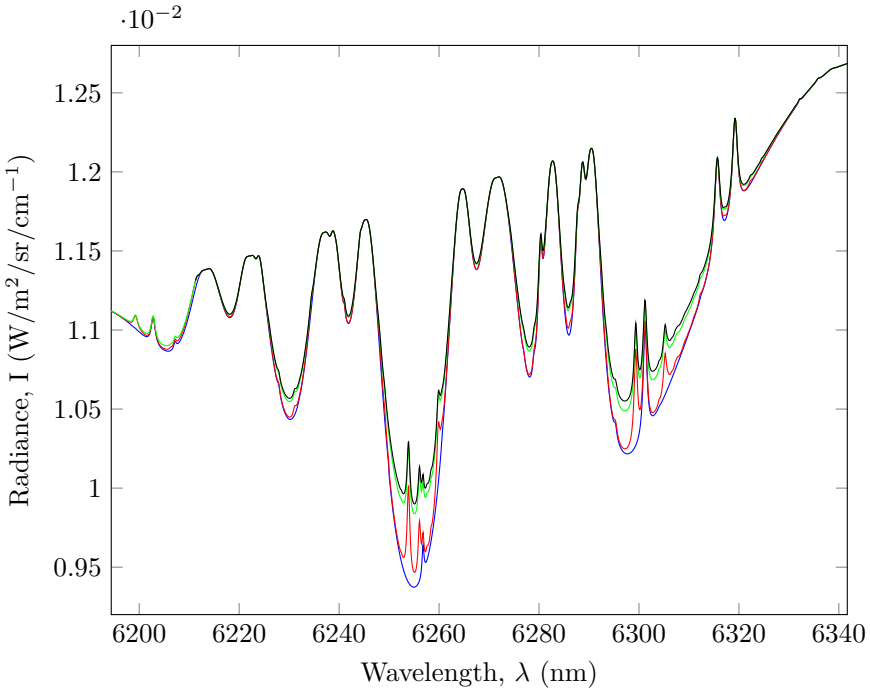

Figure 6.7: Varying isotopes of water and spectral window width. Blue - 50 cm^{-1} width, main isotope; red - 50 cm^{-1}, all isotopes; green - 100 cm^{-1}, all isotopes; black - 200 cm^{-1}, all isotopes.

each wavenumber in the cross-section calculation.

By including all isotopes in the calculation (and the same spectral window, red line) several new features appear where there weren't any features before, as there are weak isotope spectral lines here. Increasing the spectral window to 100 cm^{-1} (green line) had a fairly dramatic effect – the radiance was increased significantly in a few regions, illustrating the cumulative effect of the far wings of spectral lines. Increasing the window further to 200 cm^{-1} (black line) had a less noticeable effect – at this wavenumber distance the broadened lines far wings are diminished significantly, and contribute very little to the absorption.

Lastly, a calculation was made on a separate date – August 29, 2009 – to compare ozone emission centred at 9.6 μm. The exact ozone concentration profile was unknown, but even with a rough estimate the model worked quite well. The results are shown in Figure 6.8.

A final third measurement band was analyzed and modelled. Measurements from a separate

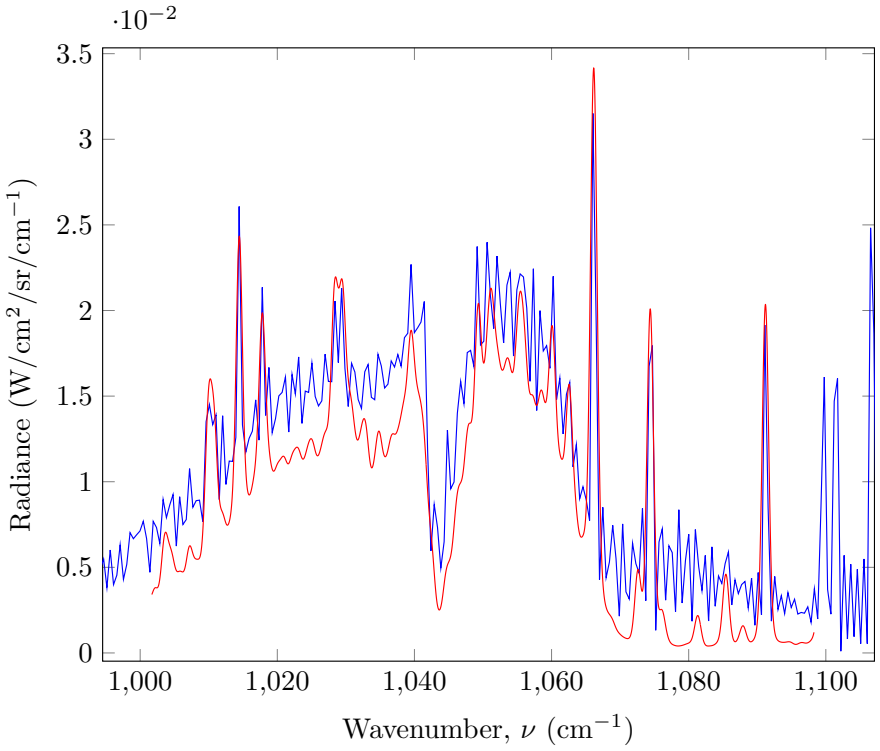

Figure 6.8: Comparison of E-AERI measurement of emission primarily from O_3 (blue), and the SASKTRAN simulation (red).

date – August 29, 2009 – were used to model the ozone emission band centred at 9.6 μm. The exact ozone concentration profile was unknown for the date, so a reasonable estimate was used based on the US Standard atmosphere. The comparison is shown in Figure 6.8, and shows good qualitative agreement, despite having an inaccurate ozone profile. The broad features of absorption and emission coincide very well, but fine spectral features differ to a certain degree. Much of the high frequency structure on the measurement is attributable to the instrument noise, so it is reasonable to assume the model and measurement agree within error.

Sources of Error

The primary source of error in these calculations was the unknown exact pressure/neutral density profile. While ECMWF is relatively accurate, it cannot compete with the resolution needed in the temperature and water vapour profiles, so some accuracy was lost in the line broadening calculations for water vapour. This had a more adverse effect on band calculations where water vapour wasn't present, where the neutral density was used to determine the quantity of CO_2, O_3, etc. from concentration profiles given in PPMV.

The other main source of error is in not knowing the exact instrument line shape function. The calculated spectrum was convolved with a sinc function (characteristic of Fourier transform spectrometers (see Appendix C), but without knowing the exact characteristics of the instrument, error will be introduced into the final low-resolution spectrum.

6.2 Near Infra-red Nadir Calculations

To validate SASKTRAN's ability to still model scattered sunlight accurately, radiance calculations were made in the near infra-red (NIR) where thermal emissions are negligible and the sun is the primary source of radiation. The NIR spans roughly 800 nm - 2500 nm. Comparisons were made to nadir measurements from GOSAT for June 9, 2010, over North Africa. This date and location was chosen due to its relatively uniform land surface and clear-sky conditions determined from cloud flags included with the GOSAT data product. As a study, both the nadir and limb radiance for 2.0 - 2.1 μm was calculated for a variety of solar zenith angles, using a standard atmosphere.

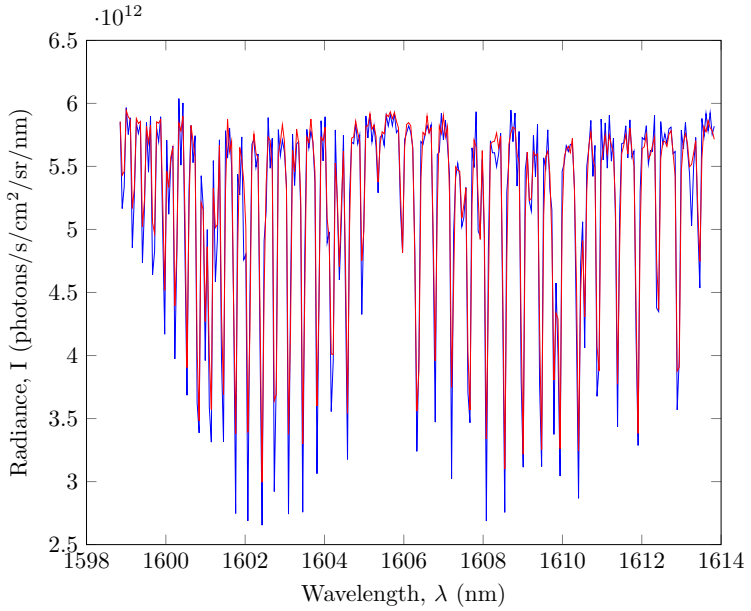

Figure 6.9: Comparison of GOSAT band 2 (weak CO_2)nadir radiance and SASKTRAN model for arbitrary 380 ppm concentration.

6.2.1 Comparison with GOSAT Nadir Measurements

The Greenhouse gases Observing SATellite (GOSAT) is a Fourier transform spectrometer that observes up-welling radiation from the earth with nadir view. It has four bands: 758 - 775 nm, 1560 - 1720 nm, 1920 - 2080 nm, and 5560 - 14300 nm. All but the last band are in the NIR, with the last band being in the far/thermal infra-red (FIR). The first band measures O_2 absorption, which is used for calibration of the instrument and determining cloudy scenes. Scans on June 9, 2010 over Northern Africa were used for comparison, as they were determined, from the GOSAT data product, to be relatively cloud-free, and provided a relatively high ground albedo, giving good signal-to-noise. The weak CO_2 absorption band from 1598.8 μm to 1613.8 μm in band 2 was used, as was the strong CO_2 absorption band from 1980 μm to 2040 μm.

Figures 6.9 and 6.10 show the SASKTRAN model versus the GOSAT measurements of radiance in their respective bands. Both band calculations compare qualitatively very well with

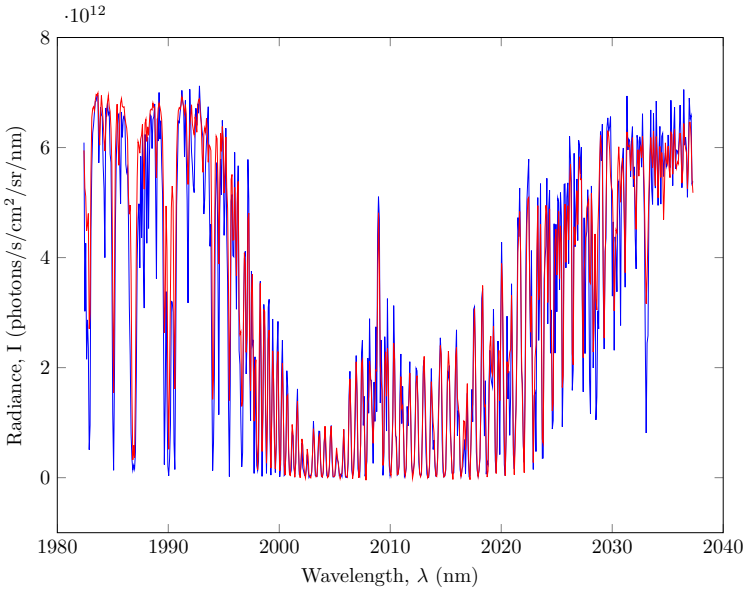

Figure 6.10: Comparison of GOSAT band 3 (strong CO_2) nadir radiance and SASKTRAN model for arbitrary 380 ppm concentration.

the band measurements - absorption troughs are roughly equivalent and line up. However, when comparing on a per-wavelength basis, large differences surfaced.

While the radiances compare well qualitatively, actual residuals between the model and measurement were quite large. Reasons for this discrepancy are discussed in the *Sources of Error* section.

Sources of Error

The primary source of error is unknown profiles for temperature, pressure, and CO_2. This is evident from the absorption troughs in the model and measurement having very different widths. Different widths of the same absorption features is a result of incorrect broadening calculations, which can arise because of incorrect temperature, or pressure, or CO_2 density, or a combination of all three, at any altitude.

The other main source of error is the unknown instrument line shape function (ILS) for the

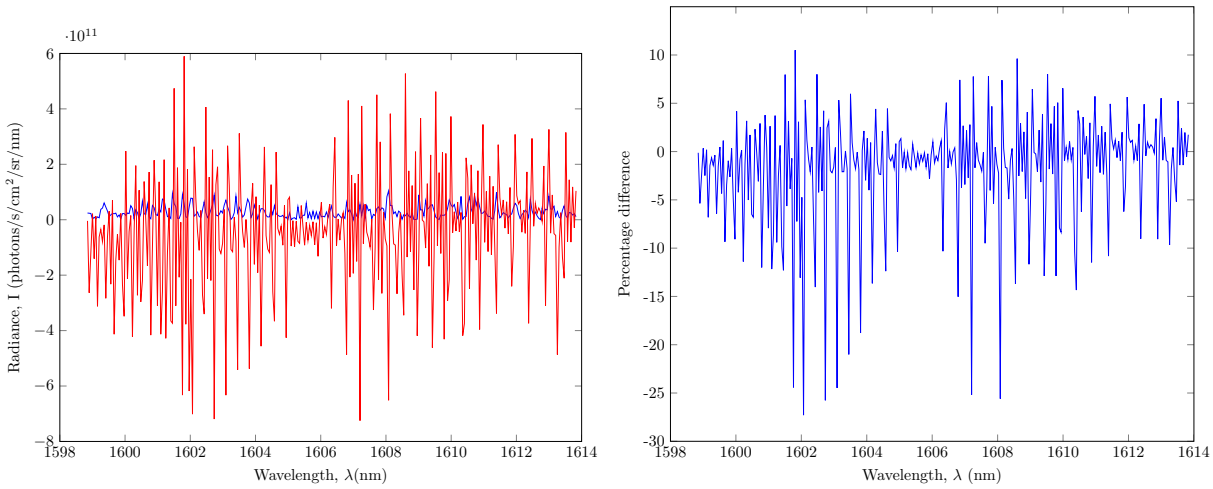

Figure 6.11: [Left] Residual difference between SASKTRAN and GOSAT for band 2 (weak CO_2) radiance, with instrument noise levels in blue, and [Right] Percentage difference for the same band.

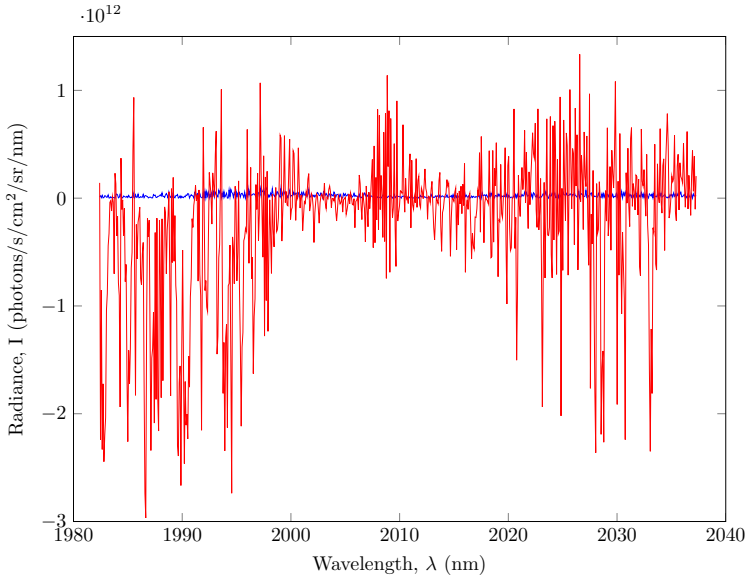

Figure 6.12: Residual difference between SASKTRAN and GOSAT for band 3 (strong CO_2) radiance, with instrument noise levels in blue. Percentage difference is not shown due to overly large error.

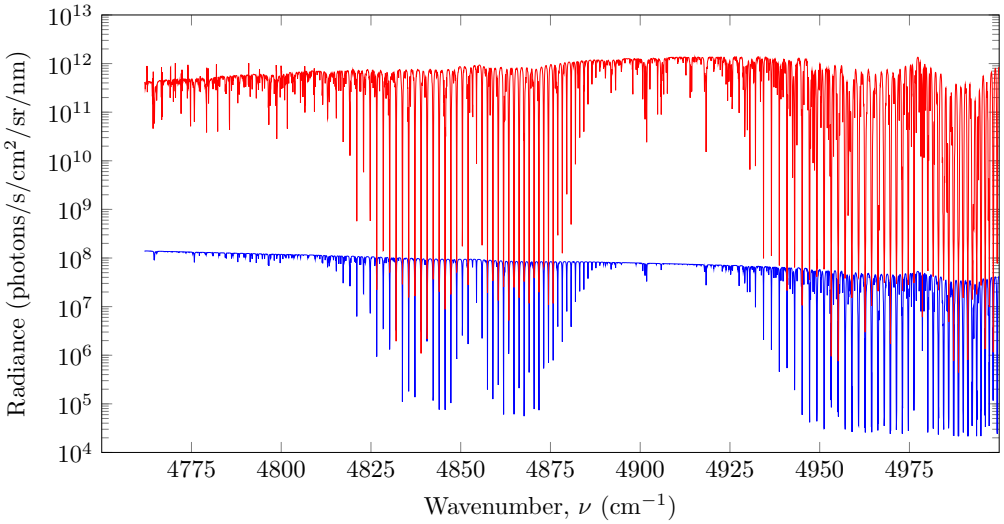

Figure 6.13: Comparison of solar (red) and thermal (blue) contributions for nadir geometry and 15^o solar zenith angle for 2.0 - 2.1 μm.

GOSAT instrument. GOSAT, being a Fourier transform spectrometer, has a boxcar function in the space domain due to the limited optical path difference introduced by the moving mirror. This leads to a sinc function in the frequency domain (see §C). However, dispersion (among other effects) introduced by the instrument optics can produce significant asymmetry and/or shift the ILS, and the sinc function is no longer truly accurate (Galli et al., 1999; Hase et al., 1999; Desbiens et al., 2002). Due to this, it would be of interest to compute the sensitivity of the radiance to temperature, pressure, and CO_2 concentration in these bands.

6.2.2 Additional Studies

Order-of-magnitude studies were obtained for 2.0 - 2.1 μm by calculating the nadir radiance for a variety of solar zenith angles, using a "standard" atmosphere (Sissenwine and Teweles, 1976). The contribution from solar radiation and thermal radiation is compared, and shown in Figure 6.13 for an SZA of 15^o.

The overall effect of varying the SZA for nadir scans from 0^o to 80^o is shown in Figure 6.14,

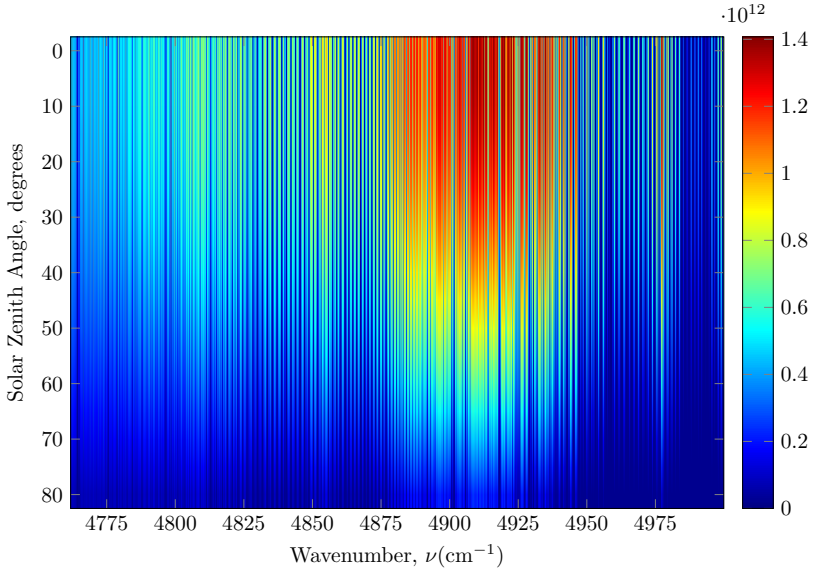

Figure 6.14: Effects of varying the solar zenith angle from 2.0 - 2.1 μm for a nadir viewing geometry on the **solar** radiance - thermal emissions were not included. As the solar zenith angle approaches 90, thermal emissions would become a larger portion of the signal.

where only solar radiation was included. This figure shows the importance of using small SZA's when in NIR bands. If the SZA is too large – especially as it approaches 90^o – thermal radiation will play a much larger role in the overall measured signal, as the solar signal diminishes.

6.3 Far Infra-red Nadir Calculations

6.3.1 GOSAT Comparisons

To verify the abilities of the model to calculate radiance in the far infra-red (FIR), comparisons were made with GOSAT's measurements in band 4 (thermal) and SASKTRAN model calculations. The chosen band of interest was from 9200 nm to 9900 nm, a region of strong O_3 absorption/emission.

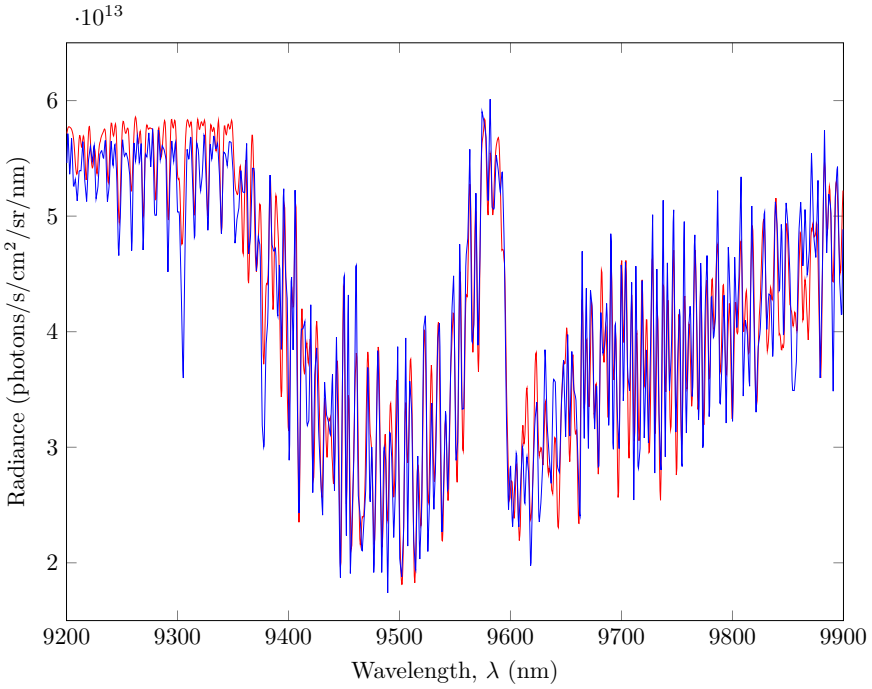

Figure 6.15: Comparison of O_3 absorption region centred around 9.6 μm. SASKTRAN (red) and GOSAT (blue).

Temperature and pressure profiles were obtained from ECMWF data for June 9, 2010 over North Africa as with the NIR measurements. Ozone profiles were obtained from OSIRIS level 2 data product (Adams et al., 2012) for the same date and location. Like the band 2 and 3 comparisons, the measurement and model compare quite well qualitatively (Figure 6.15). However, when compared on a per-wavelength basis, large relative difference occur (Figures 6.16 and 6.17). Again, this is most likely due to uncertainty in the pressure and temperature profiles, and the unknown ILS. Another source of error that would have had a noticeable effect in the model-vs.-measurement tests is the error contained in the HITRAN database itself. While generally accurate, the spectroscopic constants contained within the HITRAN database are still often based off of models which contain an inherent error. When analyzing dense spectral regions, these otherwise tiny errors may manifest themselves as visible inaccuracies.

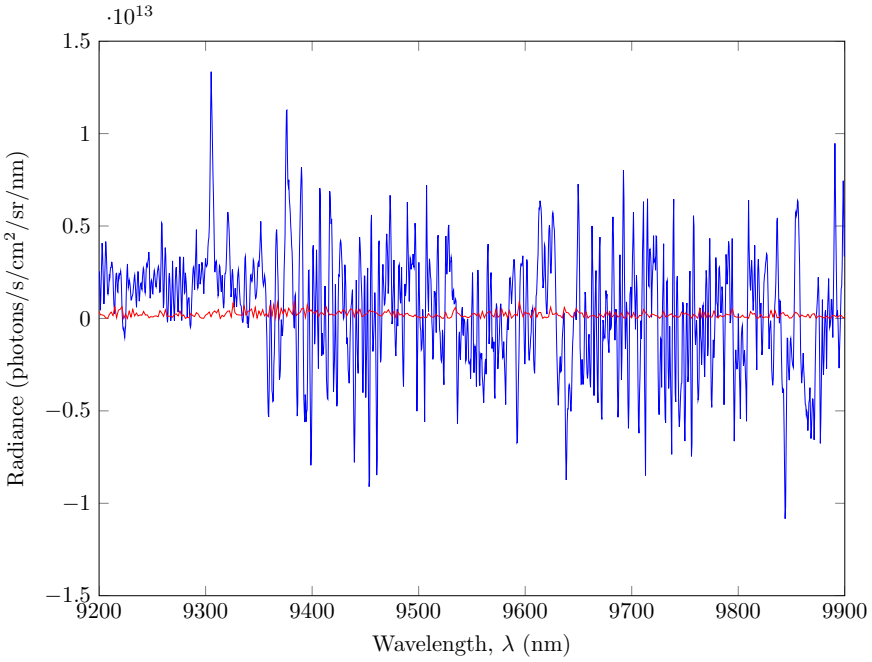

Figure 6.16: Residual of model minus the measurement (blue), with noise levels of the GOSAT instrument (red).

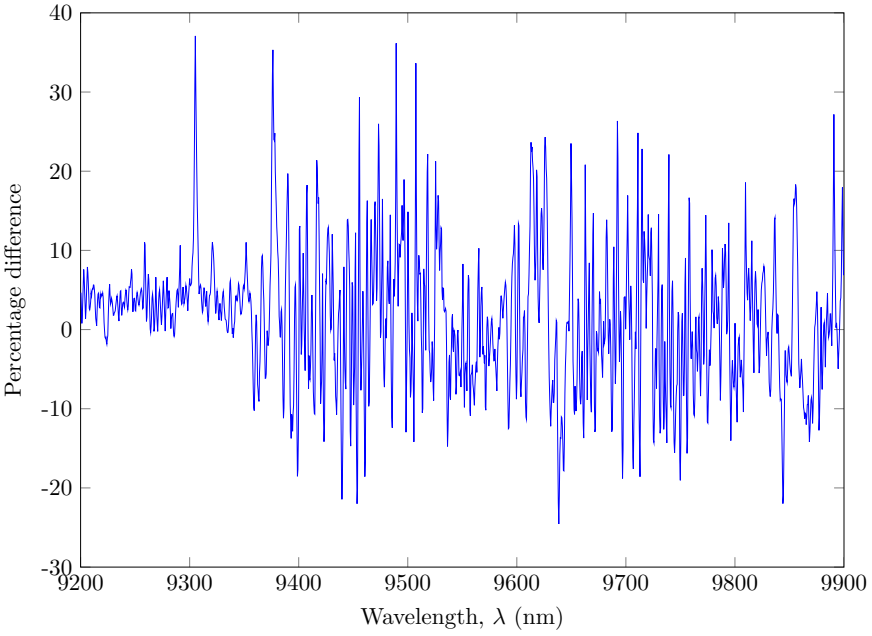

Figure 6.17: Percentage difference for band 4 O_3 absorption. Large spikes are mostly due to uncertainty in the temperature/pressure profiles and the ILS.

6.3.2 LBLRTM Comparisons

As has been shown, measurements are notoriously difficult to model accurately – there are simply too many variables most of the time. A more realistic comparison is to utilize another well-established radiative transfer model with the same inputs as that of SASKTRAN, and calculate the observed radiance using both models. One such model is LBLRTM, which has undergone numerous trials that have repeatedly shown its accuracy in modelling radiation in the infra-red (Turner et al., 2001). Comparisons were made in five bands between LBLRTM and SASKTRAN: 1200 - 1340 cm^{-1} (CH_4), 1030 - 1070 cm $^{-1}$ (O_3), 620 - 720 cm^{-1} (CO_2), 1050 - 1150 cm^{-1} (edge of O_3), and 1560 - 1660 cm^{-1} (H_2O). For each calculation, the same observer and look direction were used, and the US standard atmosphere for all 42 primary molecular species in the atmosphere (N_2, O_2, H_2O, CO_2, CH_4, N_2O, SO_2, ...) was utilized.

While LBLRTM has been extensively verified (Turner et al., 2001), there are a number of simplifying assumptions the model makes that should be addressed. Firstly, LBLRTM is a two-stream radiative transfer model that assumes a plane-parallel atmosphere, whereas SASKTRAN is a successive orders model in a fully spherical geometry. This affords SASKTRAN more accuracy in the calculations of attenuation between points in the atmosphere. LBLRTM speeds up Voigt broadening calculations (the most taxing part of the calculation in SASKTRAN) by assuming an "average wavenumber" per calculation. This would mean SASKTRAN supplies a slightly more accurate calculation of the absorption coefficients than LBLRTM. Another key difference between the two models is that SASKTRAN uses HITRAN 2008, and LBLRTM uses HITRAN 2000 – the older version misses many absorption lines accounted for in the newer version, thus giving SASKTRAN another slight increase in accuracy over LBLRTM.

Comparisons began with the dominantly CH_4 absorption band from 7462.69 - 8264.46 nm (1200 - 1340 cm^{-1}). Figure 6.18 shows the comparison between both models at their high resolution. SASKTRAN radiance was computed with a resolution of 0.005 cm^{-1} and LBLRTM

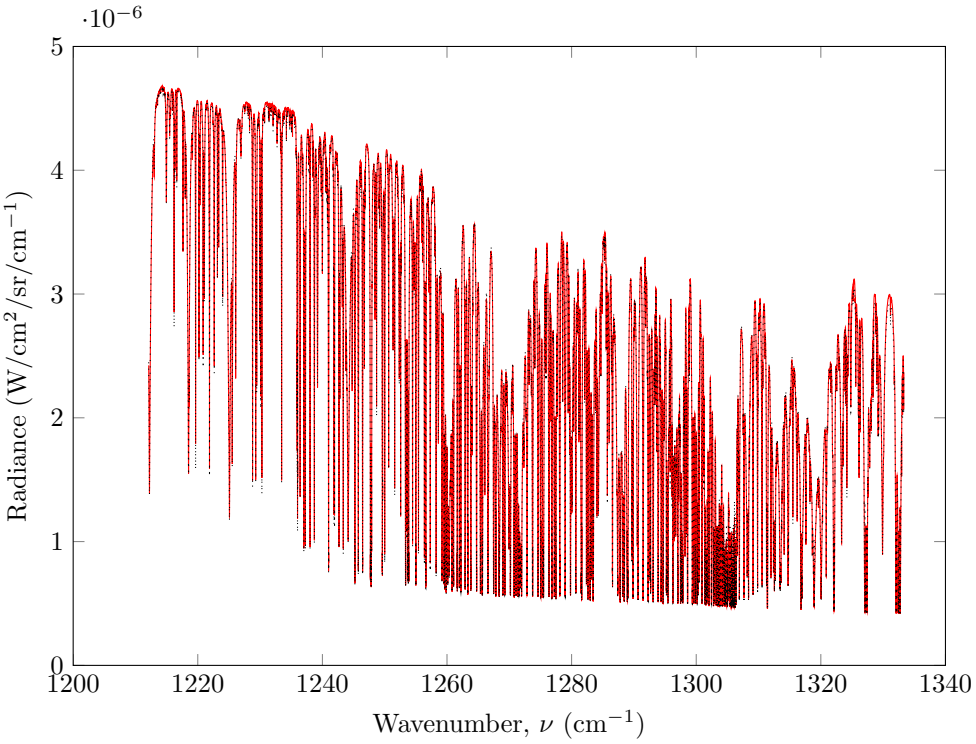

Figure 6.18: Comparison of high-resolution models SASKTRAN (red) and LBLRTM (dotted black) for the CH_4 absorption centred at 7.9 μm.

computed the radiance with a resolution of 0.00024 cm^{-1}, and both with a ground emissivity of 0.96. The models compare very well, though due to its higher resolution, LBLRTM shows several features not visible on SASKTRAN's computation. While SASKTRAN *could* have been used at a higher resolution, the already days-long computation at 0.005 cm^{-1} would have taken 20 times as long. To compare the models properly, the radiance spectra were convolved with a common instrument line shape – a Gaussian with 1.0 cm^{-1} FWHM. The low-resolution comparison of the two spectra is shown in Figure 6.19, with the percentage difference shown in Figure 6.20.

The maximum difference of 1-2% is very encouraging. Given that LBLRTM has been validated against satellite measurements and other radiative transfer models (Turner et al., 2001) and is used in the retrieval of molecular species from FIR satellite measurements (Alvarado et al., 2013), this is very good validation of SASKTRAN's ability to model thermal radiation.

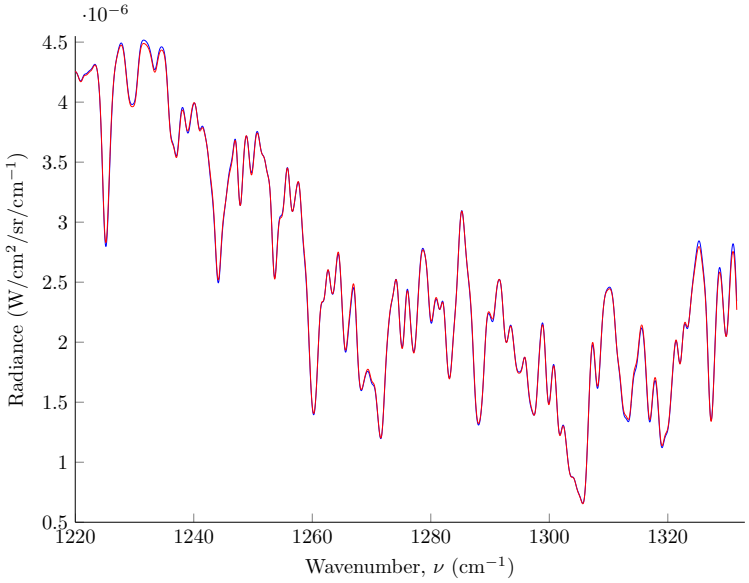

Figure 6.19: Comparison of SASKTRAN (blue) and LBLRM (red) spectra after convolution with a 1.0 cm^{-1} FWHM Gaussian in the CH_4 band centred at 7.9 μm.

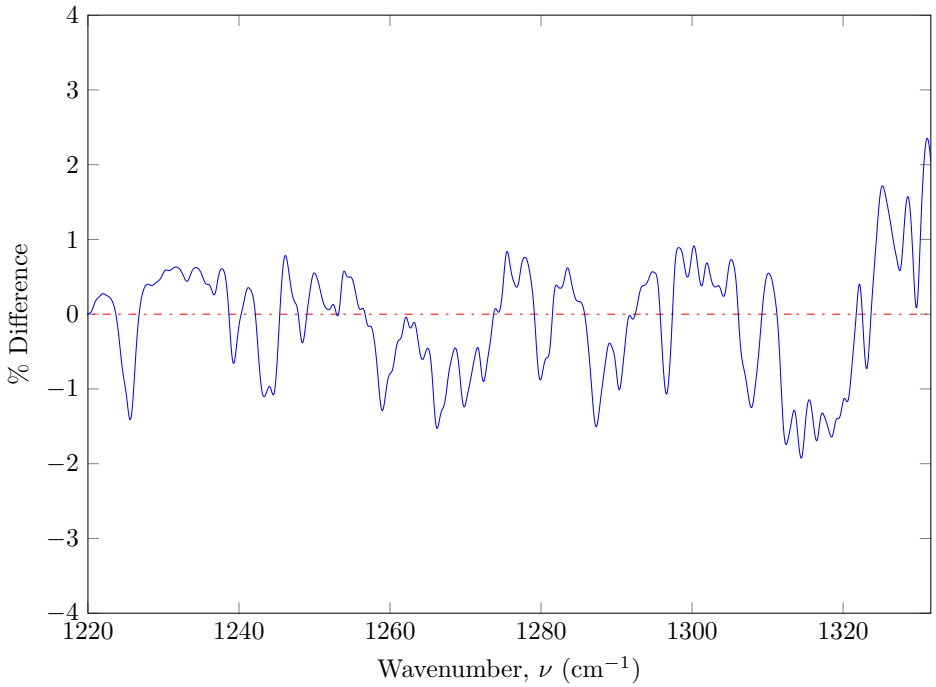

Figure 6.20: Percentage difference between both models once convolved with a 1.0 cm^{-1} FWHM Gaussian in the CH_4 band centred at 7.9 μm.

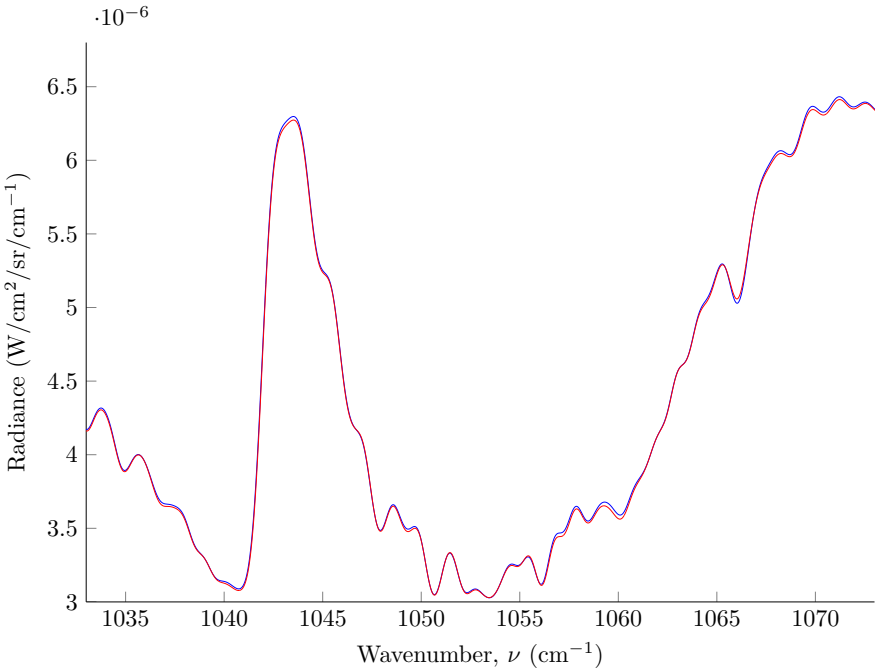

Figure 6.21: Low resolution comparison of SASKTRAN and LBLRTM in the 9.6 μm band (O_3) after convolution with 1.0 cm^{-1} FWHM Gaussian.

The next region for comparisons was the O_3 absorption band centred around 9.6 μm. The same procedure was followed as with 7.9 μm CH_4 band. The low-resolution comparisons is shown in Figure 6.21, and the percentage difference in Figure 6.22.

The results in the O_3 band centred at 9.6 μm compare even better with LBLRTM than the 7.9 μm CH_4 band - all SASKTRAN calculations lie within 1% of the LBLRTM model radiances.

Further calculations were done in the 15 μm CO_2 band (Figure 6.23), the 6 μm H_2O band (Figure 6.24), and the 9 μm multiple-species band (Figure 6.25). Only low-resolution comparisons and percent differences are shown.

Figure 6.23 shows that SASKTRAN compares well with LBLRTM calculations in the far infra-red CO_2 absorption region around 15 μm, to within 6%.

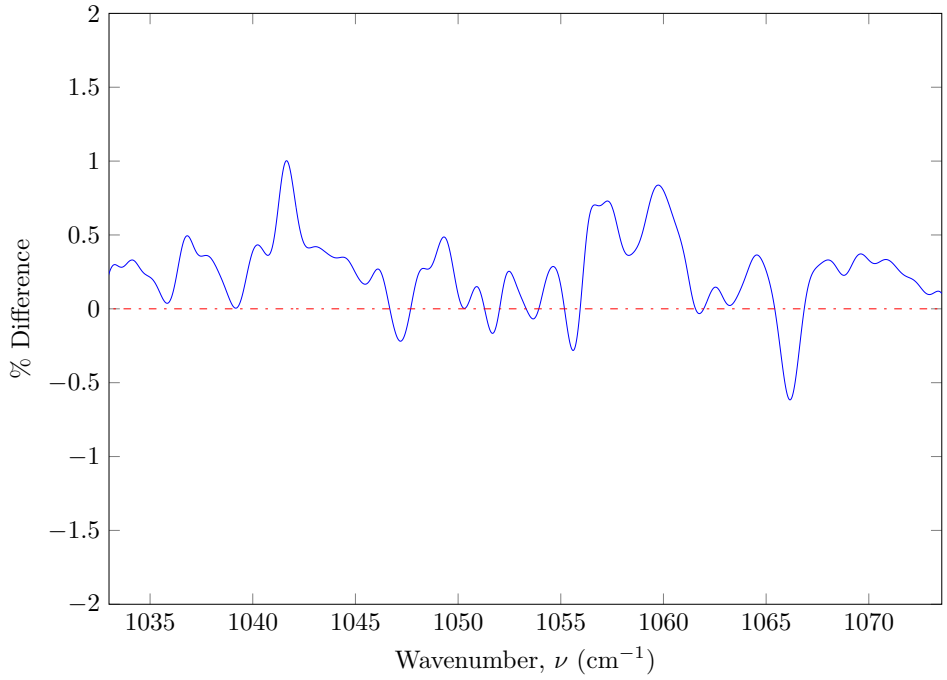

Figure 6.22: Percentage difference between SASKTRAN and LBLRTM in the 9.6 μm O_3 absorption band.

Calculation of nadir radiance in the 6 μm region, shown in Figure 6.24, had less encouraging results. This calculation is centred within a dense region of water vapour absorption lines, and is notorious within the radiative transfer community. Due to the sheer number of lines, the cumulative effect of distant lines cannot be ignored, and so the typical 25.0 cm^{-1} window needs to be expanded – these calculations used a 100.0 cm^{-1} width on either side of the wavenumber of interest. This is a daunting calculation for any line-by-line radiative transfer model – indeed with SASKTRAN's brute-force method this resulted in 5-10 seconds per wavenumber to calculate the radiance.

Historically, to get around the issue of far-wing effects, radiative transfer models utilized a **continuum model** which represented the background absorption due to the cumulative effects of the far wings of lines. Thus the window width can be reduced to decrease time in line-by-line calculations. LBLRTM utilizes the MT-CKD 2.0 water vapour continuum (Mlawer et al., 2012), which calculates the background absorption of water vapour as a function of temperature, atmospheric pressure ("foreign broadening"), and water vapour

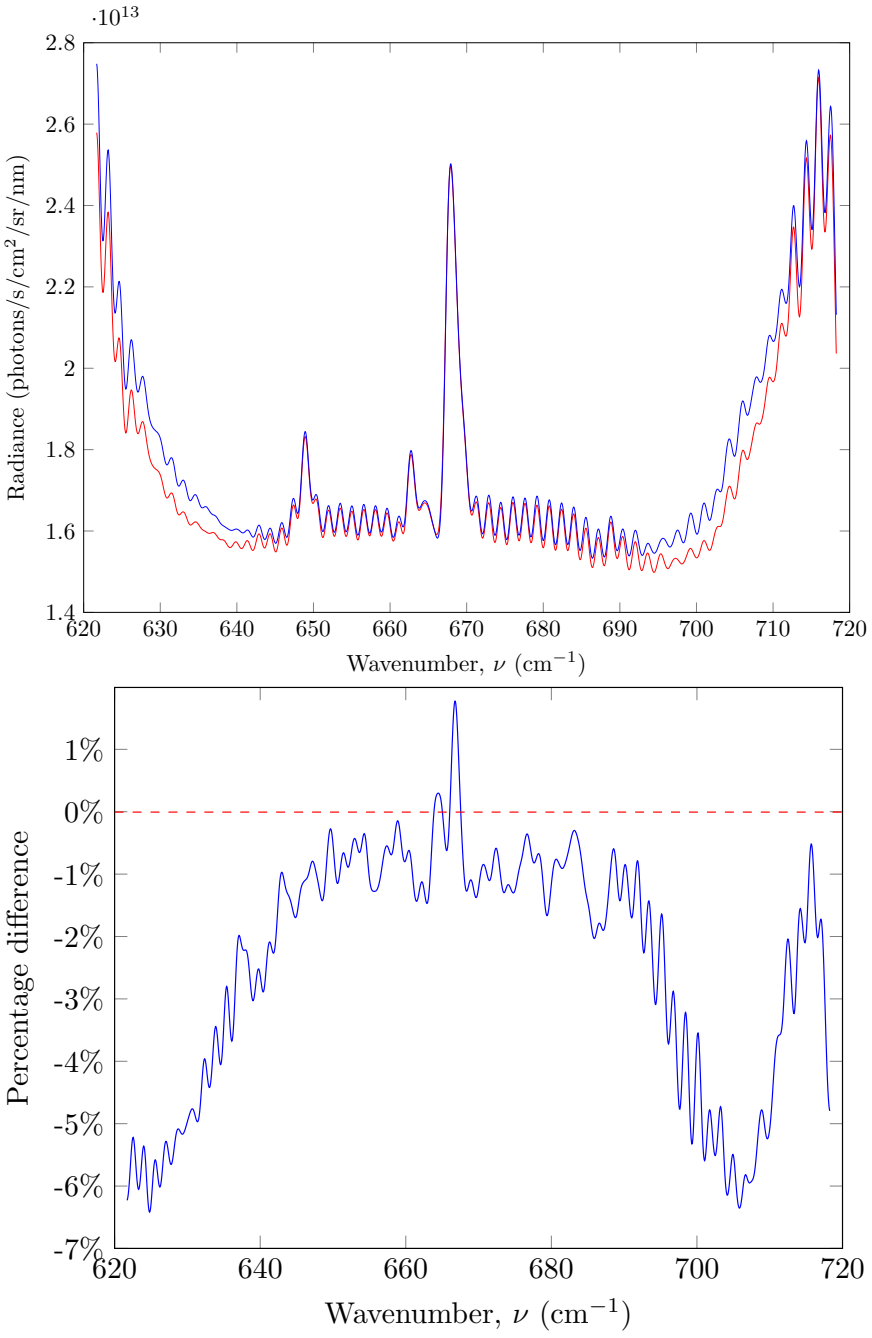

Figure 6.23: [Left] Comparison of low-resolution SASKTRAN (red) and LBLRTM (blue) radiances at the 15 μm CO_2 absorption band. [Right] Percentage difference between the SASKTRAN and LBLRTM spectra.

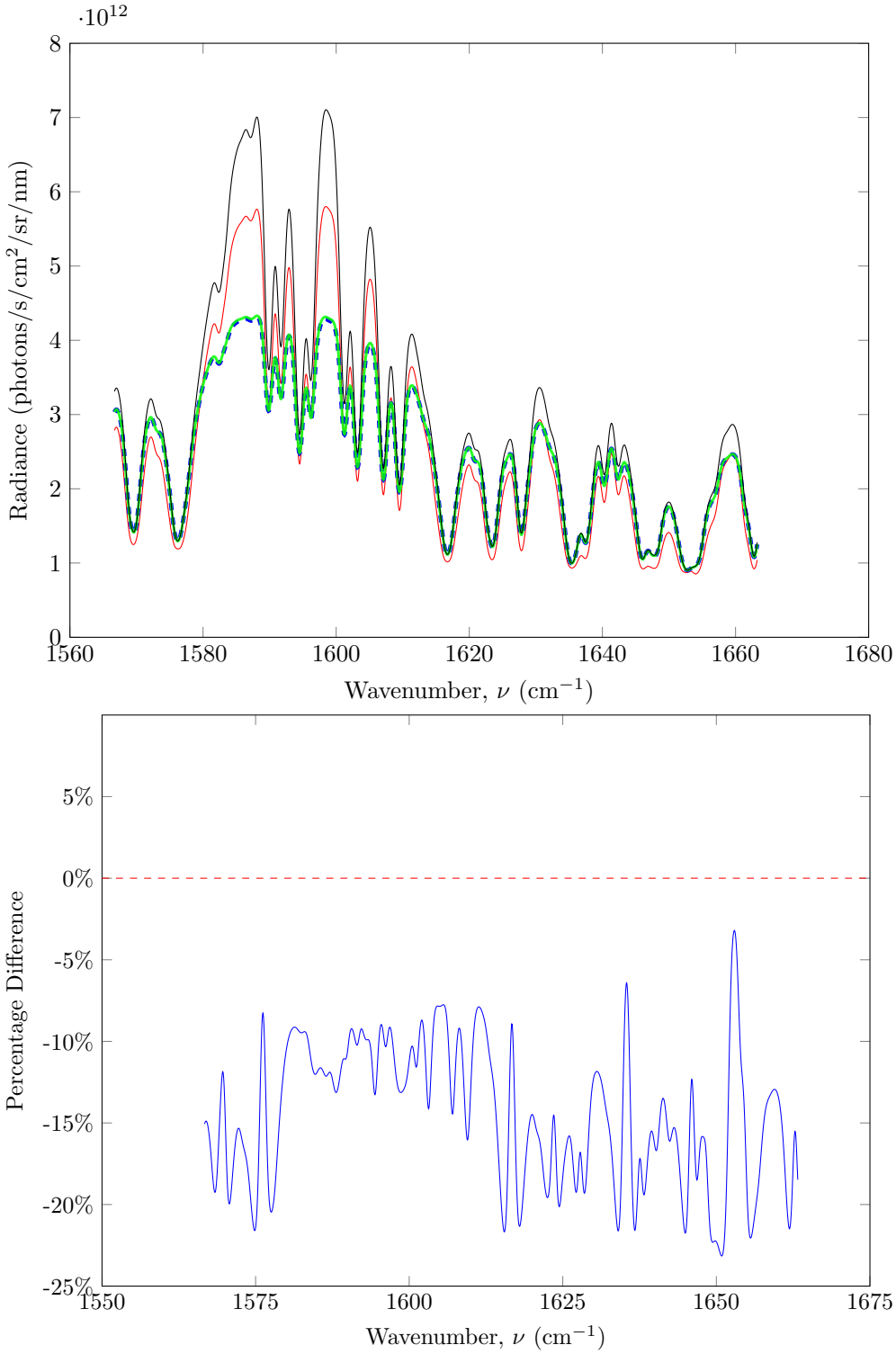

Figure 6.24: [Top] Comparison of low-resolution model spectra at the 6 μm H_2O absorption band – SASKTRAN (red) and various iterations of LBLRTM calculations with the water vapour continuum. Blue dashed line is LBLRTM with the full water vapour continuum used, green has LBLRTM ignore self-broadening effects in the continuum, and black ignores foreign-broadening effects in the continuum. [Bottom] Percentage difference between the SASKTRAN and LBLRTM (full continuum) spectra. This spectrum was calculated using a 100.0 cm^{-1} spectral width.

pressure ("self broadening"). Figure 6.24 shows the SASKTRAN calculation in red. The blue line is LBLRTM including the full water vapour continuum. Note that it appears to over-estimate the absorption. The green line is LBLRTM ignoring the effects of self-broadening in the continuum calculation – the effect is obviously small, as there is little change from the full continuum model. However, when foreign broadening is ignored in the continuum, LBLRTM underestimates the absorption significantly (black). The continuum model remains an approximation, and research shows that the absorption coefficient from the effects of the far wings of lines are over-estimated (Nesmelova et al., 1991; Niro et al., 2004), which is what was observed in these calculations. The second figure shows that percentage difference between LBLRTM and SASKTRAN when the continuum is included in full.

Comparisons of calculated radiance at 9 μm, shown in Figure 6.25, give very encouraging results. This band is on the edge of a strong ozone absorption band, but lacks significant absorption from other species. The final comparison showed agreement to within 1.5% between SASKTRAN and LBLRTM.

Sources of Error

While the models agreed very well with each other, there were still small differences in the spectra. The primary reason for the discrepancy is due to LBLRTM calculations being performed at roughly 20 times the resolution of SASKTRAN - many absorption/emission features resolved by LBLRTM were missed by SASKTRAN. The convolution with a hypothetical ILS Gaussian smoothed out most of these differences, but the effects were still visible in the low-resolution spectra. While it would have been possible to run SASKTRAN with the same resolution as LBLRTM, increasing the calculation time 20-fold was not feasible for this project.

Small differences may arise due to the spectral databases used by either model - SASKTRAN currently utilizes HITRAN 2008, while LBLRTM uses line parameters from HITRAN 2000

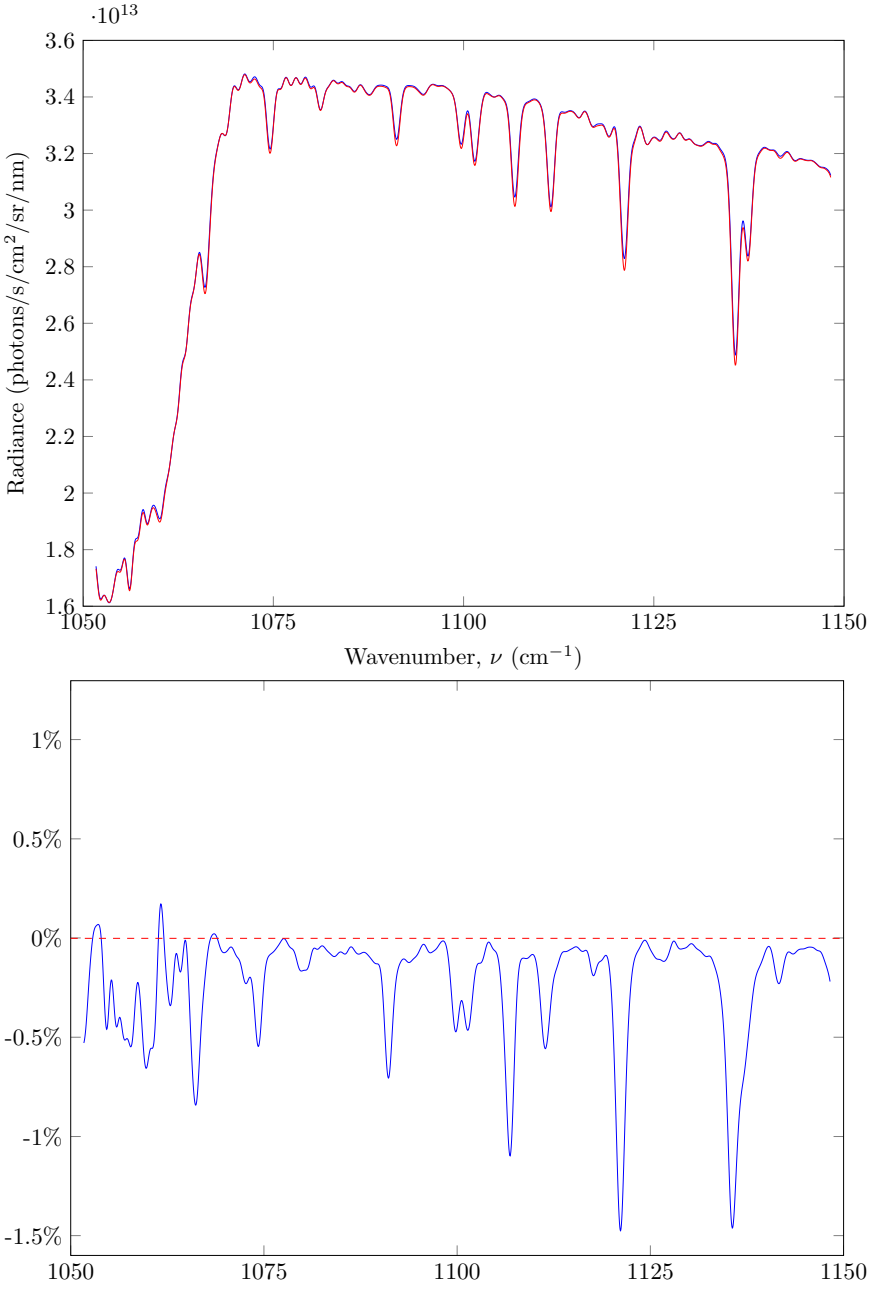

Figure 6.25: [Left] Comparison of low-resolution model spectra at 9 μm - SASKTRAN (red) and LBLRTM (blue). [Right] Percentage difference between the SASKTRAN and LBLRTM spectra.

(Clough et al., 2005). HITRAN is continuously updating its database, so some absorption lines may be missing from the 2000 version that were included in the 2008 version.

Another difference arises due to the way line broadening is performed in each model. SASKTRAN uses Voigt broadening by default, and calculates all necessary parameters exactly for every wavenumber, which is computationally intensive. Likewise, LBLRTM uses Voigt broadening, but speeds up the calculations by using an "average wavenumber" for each band calculation. This gives a small difference in the broadening of spectral lines. As such, SASKTRAN is considered to be the more accurate of the two models in calculation of absorption coefficients.

Small differences may also have arisen due to the difference in model architectures. While SASKTRAN is a successive-orders ray-tracing model in a spherical geometry including multiple scattering and solar contributions, LBLRTM is a two-stream model in a plane-parallel atmosphere which only models upwelling/downwelling thermal emissions accurately. Since spectra were computed in the true nadir geometry in the FIR, differences due to multiple scattering, spherical geometry, and solar contributions are minute, as can be seen by Figures 6.19 and 6.21. Regardless, SASKTRAN accounts for small variations in geometry, and thus considered the more accurate of the two models.

6.4 Mid Infra-red Nadir Calculations

With the ability to accurately model solar radiation in the NIR and thermal radiation in the FIR, SASKTRAN should have the capability to model radiation in the mid infra-red (MIR) region from 3 - 5 μm, where solar and thermal radiation are the same order of magnitude. This region is avoided by most radiative transfer models – typically opting to accurately model scattered sunlight or thermal radiation, but rarely both. The same is true for satellites – only a handful of instruments take radiance measurements in this spectral region, the most

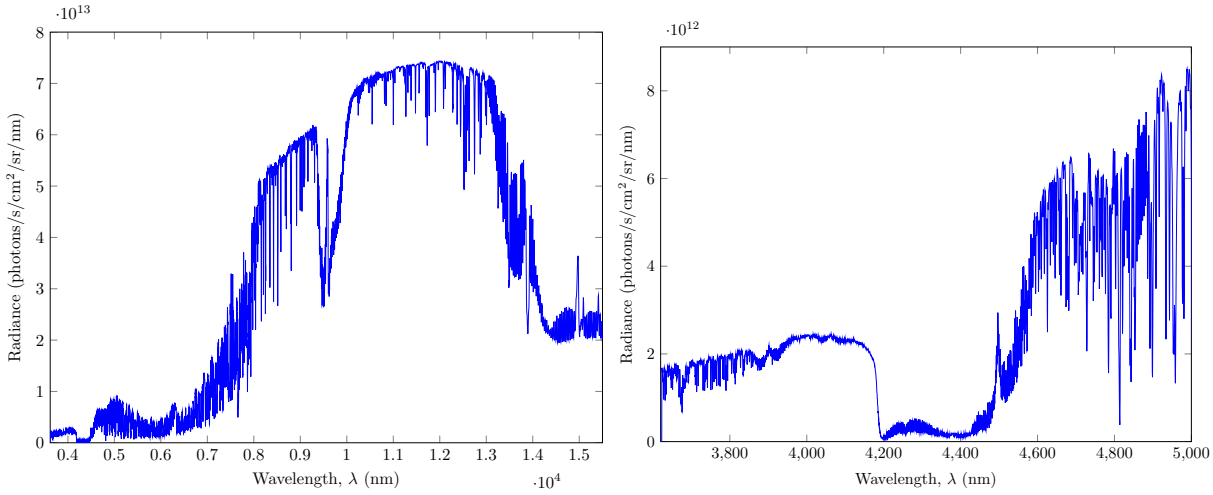

Figure 6.26: [Left] A typical IASI radiance spectrum. [Right] Zoomed-in lower left portion of the spectrum, showing the MIR region of IASI.

relevant being the *Infrared Atmospheric Sounding Interferometer* (Chalon et al., 2001) and *Atmospheric Infrared Sounder* AIRS (Kempler, 2002). A good overview of MIR radiative transfer is given in Griffin et al. (2004).

6.4.1 Comparisons with IASI

IASI is an interferometer onboard the METOP satellite as part of EUMETSAT's METOP-A program to monitor the atmosphere. It views upwelling MIR and FIR (3.7 - 15.5 μm) radiation in a nadir geometry, with the primary goal of retrieving accurate temperature and humidity profiles, and additional monitoring of trace gases like O_3, CH_4, and CO on a global scale. Of interest to my studies was the MIR region from 3.7 - 5.0 μm. Figure 6.26 shows a typical IASI spectrum.

Spectra from June 9, 2010 over North Africa were obtained, as GOSAT scans from the same time and location were determined to be cloud-free. Comparisons were made for 2100 - 2800 cm^{-1} (3.57 - 4.76 μm), with SASKTRAN computing the nadir radiance in this band with 0.05 cm^{-1} resolution. This broad band was chosen because solar and thermal contributions

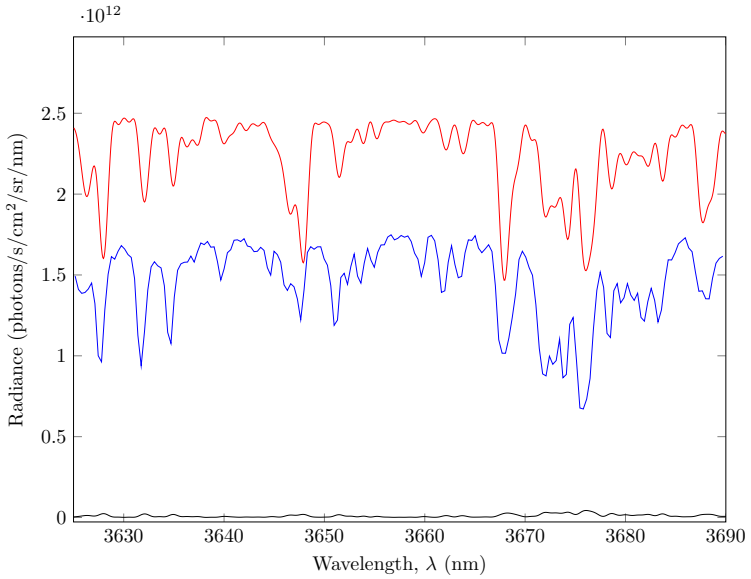

Figure 6.27: Comparison of SASKTRAN (red) and IASI (blue) measurement for 3.57 - 3.70 μm. The multiple-scatter component is shown in black.

to the radiance are of similar orders of magnitude over the band (Pan et al., 1995). In addition to the overall radiance calculation for this band, SASKTRAN was used to calculate the separate contribution from solar and thermal sources separately within the band.

Spectra in this wavenumber band were calculated using the SASKTRAN model, with rough estimates of the atmospheric profiles based off the US standard 1976 atmospheric model. Given this, the goal was to model the general absorption/emission features' shapes, rather than calculating the radiance exactly. Overall, the model did a satisfactory job of modelling this region. The results of model calculated radiance vs. IASI measurements are shown in Figures 6.27, 6.28, 6.29, and 6.30.

However, one exception occurred at the sharp change in radiance seen at 4.17 μm in Figure 6.29. This feature lies near a very strong CO_2 band, where the effects of line-coupling cannot be ignored (Clough and Iacono, 1995; Griffin et al., 2004). The current SASKTRAN model does not possess line-coupling capabilities. A full treatment of line-coupling is beyond the scope of this work, but essentially it arises at high pressures when closely-spaced absorption

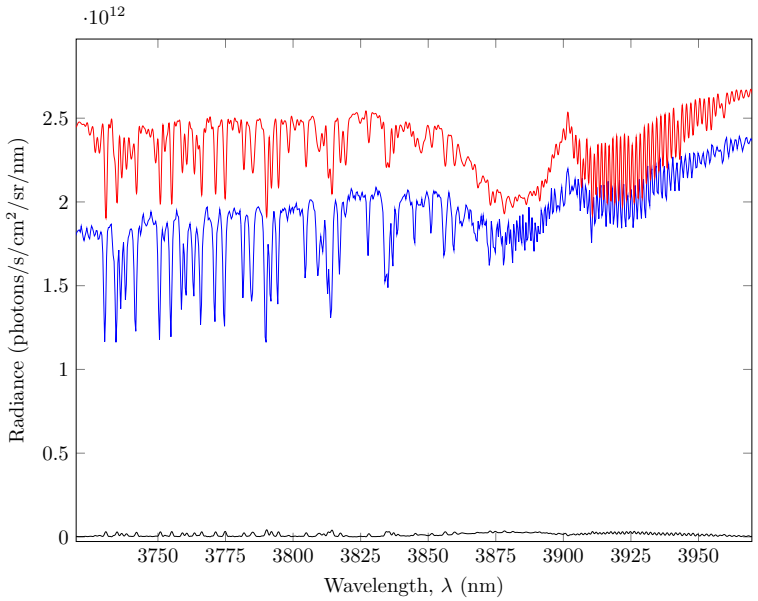

Figure 6.28: Comparison of SASKTRAN (red) and IASI (blue) measurement for 3.70 - 4.00 μm. The multiple-scatter component is shown in black.

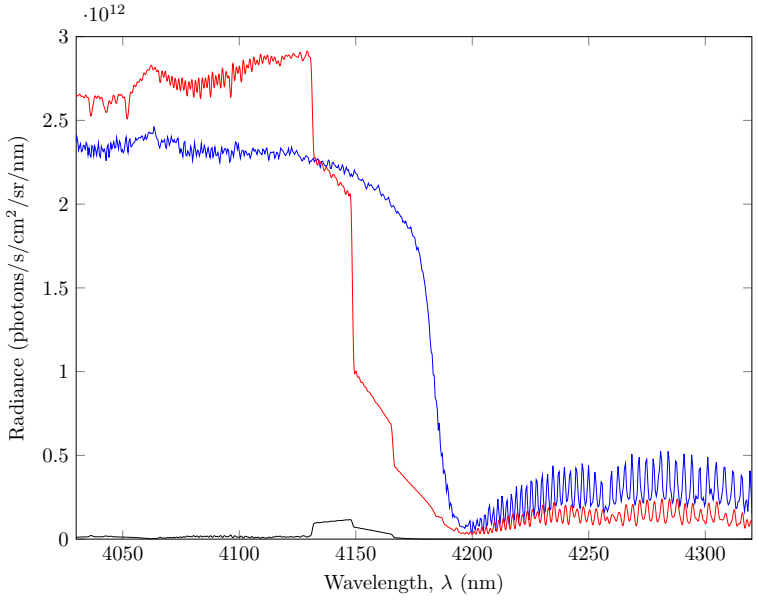

Figure 6.29: Comparison of SASKTRAN (red) and IASI (blue) measurement for 4.00 - 4.35 μm. The SASKTRAN model falls short of modelling the band features here. The multiple-scatter component is shown in black.

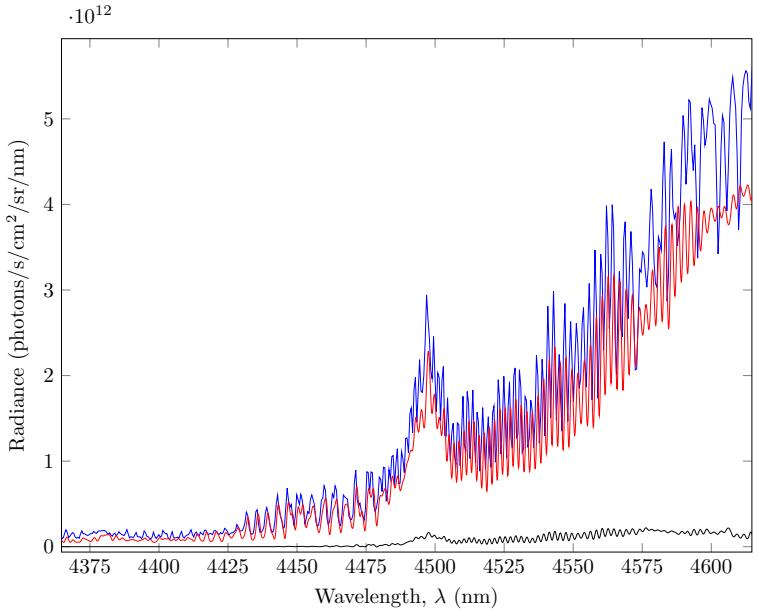

Figure 6.30: Comparison of SASKTRAN (red) and IASI (blue) measurement for 4.35 - 4.76 μm. The multiple-scatter component is shown in black.

lines broaden and overlap considerably such that they cannot be considered separately – indeed, their combined effect is less than the total effect of considering them separately. The effect is explained in more detail in chapter §4.

Figure 6.31 shows the transmission of radiation through the atmosphere as a function of wavelength around the 4.17 μm anomaly as calculated by LBLRTM, including the effects of line-mixing. The transmission drops off very sharply around 4.19 μm, to a point where the absorption (due to CO_2) is completely saturated. This may be at the heart of SASKTRAN's calculations that did not compare well in Figure 6.29. However, more study into this sensitive cross-over region is needed and thus will not be discussed further.

A significant reason for the discrepancy is due to the accidental neglect to include N_2 absorption. Molecular nitrogen has a few weak absorption lines between 3808.8 - 5018.5 nm, and due to its abundance in the atmosphere, plays a large role in the absorption features in this band (Rinsland et al., 1981). This would affect the results obtained in Figures 6.27 - 6.30.

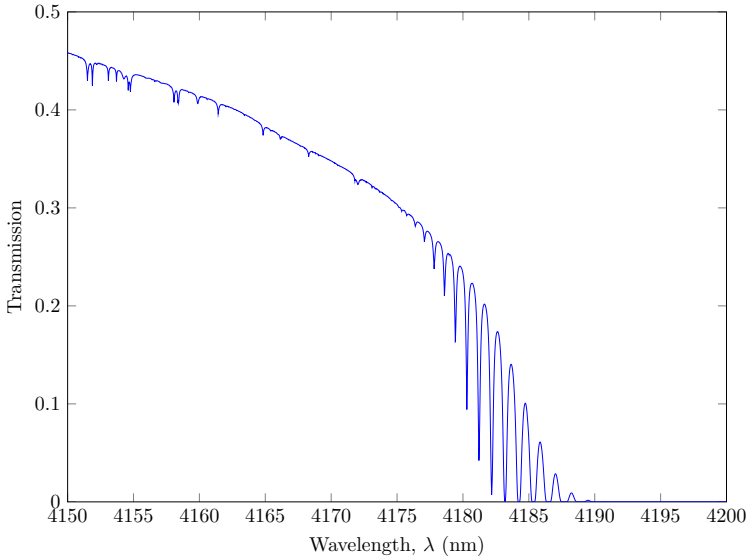

Figure 6.31: Transmission calculation near the "troublesome" 4.17 μm point by LBLRTM at 330 ppm.

Sources of Error

As mentioned, the main source of error in modelling the IASI scans was the unknown temperature, pressure, and trace gas profiles, leading to relatively large errors for all spectra. In addition, the exact emissivity of the ground at these wavelengths was not known.

One source of error that cannot be overlooked if we are to consider modelling in the MIR regions is the model's current inability to include line-coupling effects. These effects become very important in dense spectral regions, such as CO_2 bands at 4.1 μm and 15 μm (Clough and Iacono, 1995; Griffin et al., 2004).

6.4.2 Additional Studies

It was of interest to study the contribution of solar and thermal radiation to the total observed radiance in the MIR. One study by (Pan et al., 1995) had studied the contribution from each source in this region using a simplified radiative transfer model. Figures 6.32 through 6.35

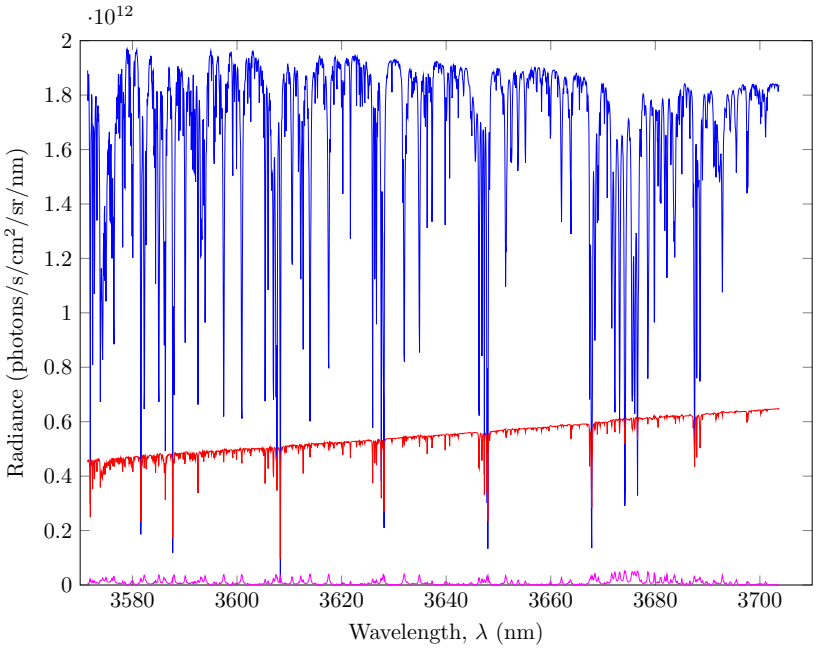

Figure 6.32: Contributions from solar (blue) and thermal (red) sources to nadir radiance from 3.57 - 3.70 μm. The second-order scattered thermal emission component is shown in magenta.

illustrate the SASKTRAN calculations of solar (blue) and thermal (red) contributions to the nadir radiance.

These results show that when observing this region, it is important to consider radiation from both sources when the sun is at SZA under 90^o. The cross-over region where both sources become equivalent agrees well with the study from (Pan et al., 1995), shown in Figure 6.36 (Pan et al., 1995), which determined the cross-over to be at roughly 2450 cm^{-1} (4.08 μm), which is very close to the cross-over of the red and blue curves shown in Figure 6.34.

The goal of this section was to provide sufficient proof of SASKTRAN's new-found ability to accurately model thermal emissions in the atmosphere without disrupting accuracy in solar radiation modelling. This was accomplished by comparing SASKTRAN model runs against satellite-based nadir measurements in the NIR from GOSAT, against FIR satellite-based nadir measurements from GOSAT and ground-based measurements from E-AERI, and against MIR satellite-based nadir measurements from IASI. All results, while not com-

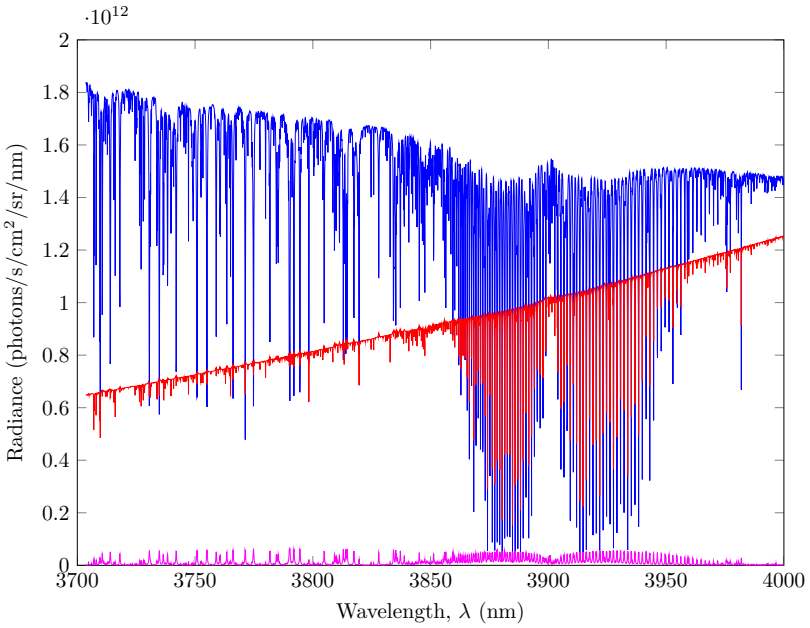

Figure 6.33: Contributions from solar (blue) and thermal (red) sources to nadir radiance from 3.70 - 4.00 μm. The second-order scattered thermal emission component is shown in magenta.

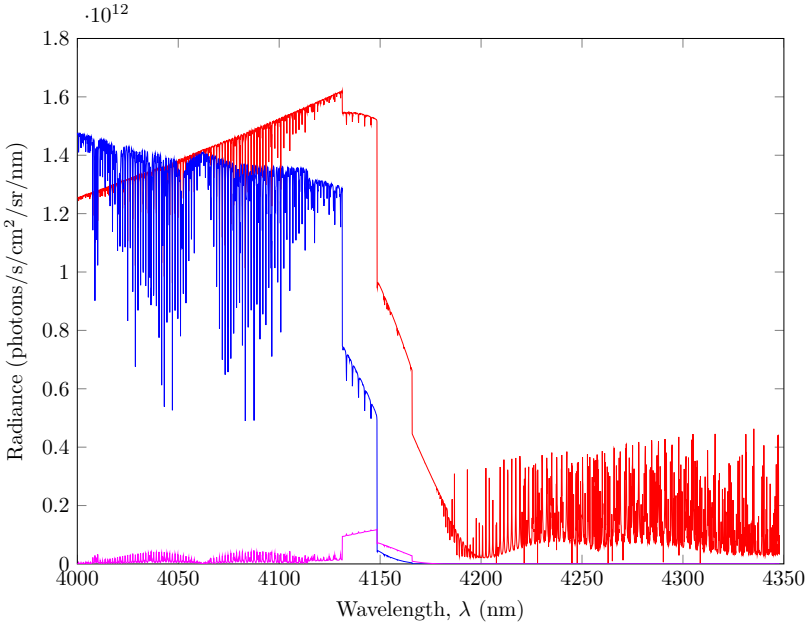

Figure 6.34: Contributions from solar (blue) and thermal (red) sources to nadir radiance from 4.00 - 4.35 μm. The second-order scattered thermal emission component is shown in magenta. As can be seen, the erroneous calculation applied equally to the thermal and solar contributions.

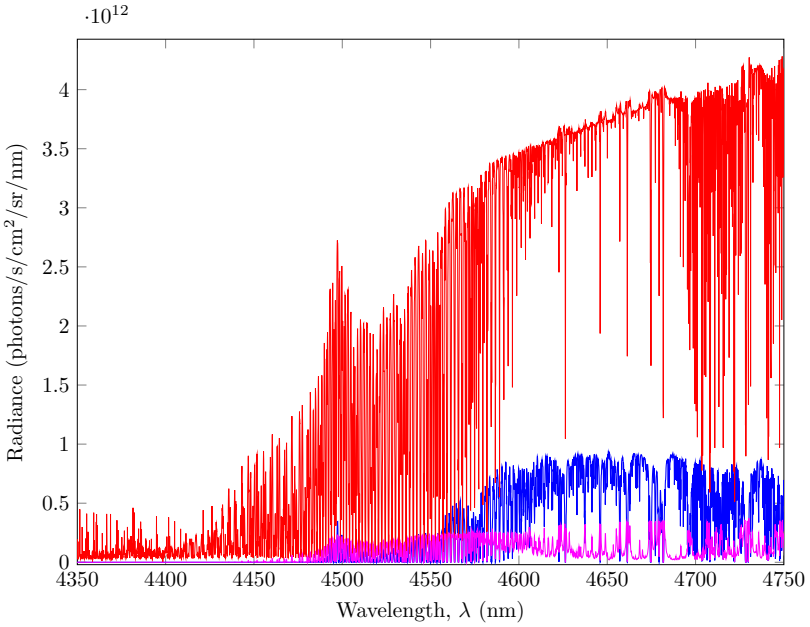

Figure 6.35: Contributions from solar (blue) and thermal (red) sources to nadir radiance from 4.35 - 4.76 μm. The second-order scattered thermal emission component is shown in magenta.

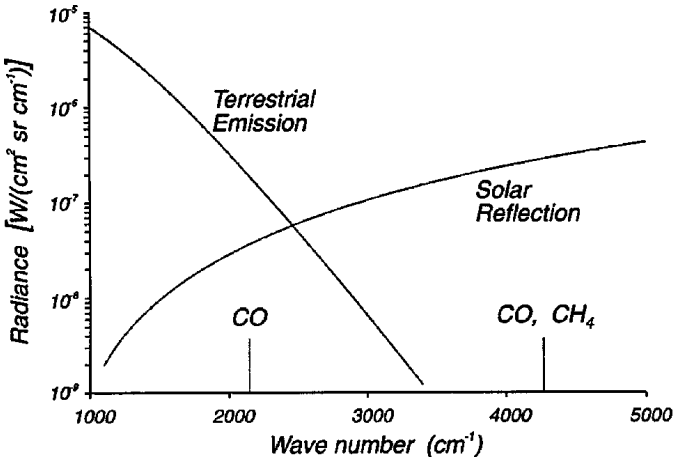

Figure 6.36: Cross over region between thermal and solar emissions, as determined by (Pan et al., 1995).

putationally within error of the measurements, qualitatively agreed well, showing important spectral features with the correct order of magnitude radiance. Encouraging verification of SASKTRAN's thermal radiation modelling capabilities occurred in comparisons with another well-tested radiative transfer model, LBLRTM. Using identical input parameters to both models, results agreed to within $\pm$ 5%. The final chapter will summarize the work that has been done in this thesis, and will give an overview future work that will be necessary to complete before the model is fully functional.

Chapter 7

Conclusion

> If we knew what it was we were doing, it would not be called research, would it?
>
> Albert Einstein

An overview of the SASKTRAN model and the additions made to it during this thesis work were given in detail. The effects of including thermal emissions in the near, mid, and far infra-red were studied using nadir calculations of radiance, and were qualitatively compared with satellite and ground-based measurements.

SASKTRAN simulations were also verified against a previously-verified radiative transfer model, LBLRTM, and agreed to within 2% for all far infra-red bands analyzed when using identical profiles for both models. Thus it was determined that most of the error in modelling arose from unknown atmospheric profiles, unknown instrument line shape functions, and, in the case of the mid infra-red calculations, exclusion of line-coupling from the absorption cross-section calculations, as well as neglecting to include contributions from N_2 absorption and emission.

7.1 Current Standing

At the time of publishing this thesis, the thermal emissions addition has been integrated into the newest version of the model – SASKTRAN v3. The newest model has three separate engines – the slightly modified successive orders engine, the new high resolution three-dimensional engine, and the Monte Carlo engine. The thermal emissions source function was integrated into the first two engines, while the Monte Carlo engine is left as future work.

All testing of the capabilities of SASKTRAN with thermal emissions was accomplished with the previous version of the model, SASKTRAN v21. As shown in Chapter §6, testing of the model's abilities to calculate nadir radiance from the near to far infra-red agreed reasonably well with satellite measurements, and agreed very well (within 2%) in the far infra-red with LBLRTM, a well-verified model.

With thermal emissions included in the SASKTRAN model, it opens doors for one of the first high-accuracy studies of radiation in the mid infra-red region. As mentioned throughout this thesis, few (if any) radiative transfer models handle both the scattering of solar radiation and the radiation from the air and ground accurately – typically they stick to one regime or the other. But with thermal emissions included in the SASKTRAN model, we can closely study the mid infra-red where solar and thermal radiation are roughly equivalent. In addition, due to the spherical geometry and multi-scattering properties of the model, it will be possible to accurately study the scattering of thermal radiation, in any viewing geometry (whereas plane-parallel models may fail in this respect).

With these added capabilities, SASKTRAN will help open the door to the information-rich infra-red portion of the atmosphere, allowing for retrievals of greenhouse gases and other trace molecules from measurements from future scientific missions where the U of S is invested.

7.2 Future Work

The addition of this model provides a great starting point for future projects and/or research areas. Before the model can be used to accurately model radiation in the infra-red, it is vital that line-coupling get included the absorption cross-section calculations. Numerous studies have shown (Kochel et al., 1997; Hartmann et al., 2009; Strow and Reuter, 1988; Rodrigues et al., 1999) how vital including line-coupling is in the retrieval CO_2 from spectral measurements.

Segueing from line-coupling to other absorption cross-section necessities, it would prove to be valuable research to explore the effects of different line broadening shapes and/or algorithms. The current model assumes a Voigt line shape for all lines, even in the far wings. However, several findings have shown the far wings of numerous spectral lines to be sub-Lorentzian, as in the case for the v_3 band of CO_2 around 2400 cm^{-1} (Tanaka et al., 2008).

In addition, the current Voigt algorithm employed by SASKTRAN is a brute-force method invoking a look-up table. Work by Abrarov and Quine (2011) shows that there are work-arounds to speed up the algorithm, or even approximate the effect of Voigt broadening at much lower spectral resolutions than typically used in radiative transfer spectroscopy.

Once accurate methods are in place for handling the absorption cross sections, it would be of interest to make attempts to accurately model spectral bands of satellite measurements. This would aid in future attempts at retrievals using SASKTRAN in the infra-red.

Once accurate methods have been developed and verified for calculating the absorption cross sections including far-wing effects and line-coupling, the next step is to perform molecular density profile retrievals from satellite infra-red measurements. The robust methods used in SASKTRAN may allow for retrievals of actual profiles of important species like CH_4 and CO_2, where previously the scientific community has been mostly making do with total column densities.

Lastly, it is necessary to include thermal emissions within the SASKTRAN Monte Carlo engine. The Monte Carlo engine, while much slower than the successive orders SASKTRAN, is an invaluable tool in verifying simulations, as it alone models the physics of scattering and absorption without approximation, so long as a large sample size is used. This will be another base line to verify the modelling of thermal infra-red by the SASKTRAN successive-orders model.

Appendix A

Chapman function

Photoionization of molecules by solar radiation is responsible for the production of various ions and atomic oxygen (the precursor to ozone). The rate of ionization depends on the neutral density, which decreases with altitude, and the incoming solar radiation, which increases with altitude. The derivation developed by Sidney Chapman in 1931 aimed to determine the rate of ion production as a function of altitude, and assumed that the ion production only depended on the amount of absorbed radiative energy.

The rate of solar absorption is given by,

$$-\frac{d\,I}{ds} = \sigma\, n_n\, I, \tag{A.1}$$

where I is the intensity of radiation, σ is the absorption coefficient, n_n is the neutral density, and s is the line of sight arc length. The primary assumption is that the rate of ion production, Q, is proportional to the absorption rate,

$$Q = -C\,\frac{d\,I}{ds} = C\,\sigma\, n_n\, I, \tag{A.2}$$

where C is an arbitrary constant. For typical atmospheric parameters, C has a value of roughly one ion-pair per 35 eV of solar energy. Maximum production rate occurs for the following,

$$\frac{d\,Q}{ds} = 0 = C\,\sigma\left(I\,\frac{d\,n_n}{ds} + n_n\,\frac{d\,I}{ds}\right). \tag{A.3}$$

For a solar zenith angle of χ, the arc length s is related to the altitude h via $ds = -dh\,\sec\chi$. This means the first term in the equation above can be arranged as follows,

$$\frac{1}{n_n}\frac{d\,n_n}{ds} = -\frac{1}{n_n}\frac{d\,n_n}{dh}\,\cos\chi = \frac{\cos\chi}{H_n}, \tag{A.4}$$

where H_n is the scale height of the neutral density. Combining the above equations, we obtain ,

$$\sigma\,H_n\,n_m\,\sec\chi = 1, \tag{A.5}$$

where the subscript m denotes the maximum of production. We now take a more approximate method to absorption than was done in the chapter on radiative transfer. Define the optical depth τ at s as $I(s) = I(\infty)\,\exp(-\tau)$, where $I(\infty)$ is the radiation intensity at the top of the atmosphere. Then,

$$\frac{d\,I}{I} = d\,\ln\,I = -\sigma\,n_n\,ds, \tag{A.6}$$

and subsequently solving,

$$\ln\Big(\frac{I(s)}{I(\infty)}\Big) = -\sigma \int_{\infty}^{s} n_n \, ds = -\sigma \, N_{ns}, \tag{A.7}$$

$$I(s) = I(\infty) \, \exp(-\sigma \, N_{nm}), \tag{A.8}$$

where N_{ns} is the column density from the top of the atmosphere to the line of sight point s, and N_{nm} is the the column density from the top of the atmosphere to the maximum production point. Since the radiative absorption coefficient is defined such that $\sigma \, N_{nm} = 1$, we have,

$$I_m = I(\infty) \, exp(-1). \tag{A.9}$$

Thus we can find the maximum ion production rate,

$$Q_m = C \, \sigma \, n_m \, I_m, \tag{A.10}$$

$$= C \, \sigma (\sigma \, H_n \, \sec\chi)^{-1} (I(\infty) \, \exp(-1)), \tag{A.11}$$

$$= \frac{C \, I(\infty) \, \cos\chi}{H_n \, \exp(1)}. \tag{A.12}$$

Knowing that the neutral density is defined by,

$$n_n = n_0 \, \exp\Big(\frac{-(h - h_0)}{H_n}\Big), \tag{A.13}$$

we can determine the height of the production peak h_m by writing,

$$\sigma \, H_n \, n_m \, \sec\chi = \sigma \, H_n \, n_0 \, \exp\Big(\frac{-(h_m - h_0)}{H_n}\Big) \, \sec\chi, \tag{A.14}$$

where n_0 is the neutral density at ground level. The dependence of the radiation intensity I on the altitude h can be determined from the above equations, giving,

$$I(h) = I(\infty)\, \exp\Big[- \sigma\, n_0\, H_n\, \sec\chi\, \exp\Big(\frac{-(h - h_0)}{H_n}\Big)\Big], \tag{A.15}$$

and to find the production rate as a function of altitude, using $Q = C\, \sigma\, n_n\, I$, we obtain,

$$Q = Q_m\, \exp\Big[1 + \frac{(h_m - h)}{H_n} - \exp\Big(\frac{(h_m - h)}{H_n}\Big)\Big]. \tag{A.16}$$

Defining $y = (h - h_m)/H_n$, we obtain the final form of the Chapman production function,

$$Q = Q_m\, \exp[1 - y - \exp(-y)] \tag{A.17}$$

Appendix B

Energy Density of Radiation in a Cavity

The following derivation is taken from Reif (1965). Consider the electromagnetic radiation which exists in thermal equilibrium inside an enclosure with a volume V and walls maintained at a temperature T. In quantum mechanical terms, the radiation is considered as an assembly of photons. In thermal equilibrium, photons are continuously being absorbed and re-emitted by the walls, and it is unnecessary to know the exact processes which bring about the equilibrium, as the probability arguments of statistical mechanics will be sufficient to solve the problem.

The photons in the enclosure must be considered as indistinguishable particles. The total number is not fixed, as that property depends on the temperature of the walls. The state s of each photon can be specified by its momentum and polarization. We can completely describe the radiation inside the cavity if we know the mean number density $\bar{n}_s$ of photons in each possible state. By virtue of Bose-Einstein photon statistics, the mean number density

of photons in a particular state s is given by,

$$\bar{n}_s = \frac{\sum\limits_{n_s} n_s \, e^{-\beta \, n_s \, \epsilon_s}}{\sum\limits_{n_s} e^{-\beta \, n_s \, \epsilon_s}}, \tag{B.1}$$

where $\beta = 1/k_B T$, and ϵ_s is the energy of the particular state s of each photon. This results becomes,

$$\bar{n}_s = \frac{\frac{-1}{\beta}\frac{\partial}{\partial \epsilon_s} \sum \, e^{-\beta \, n_s \epsilon_s}}{e^{-\beta \, n_s \epsilon_s}} = \frac{-1}{\beta}\frac{\partial}{\partial \epsilon_s} \ln(\sum \, e^{-\beta \, n_s \epsilon_s}) \tag{B.2}$$

The last sum is simply a geometric series,

$$\sum_{n_s=0}^{\infty} e^{-\beta \, n_s \epsilon_s} = \frac{1}{1 - e^{-\beta \, n_s \epsilon_s}}, \tag{B.3}$$

so that equation B.2 can be reduced to the *Planck distribution*,

$$\bar{n}_s = \frac{1}{e^{\beta \epsilon_s} - 1}. \tag{B.4}$$

Let's look closer at how the state of each photon is specified. Since we are dealing with electromagnetic radiation, the electric field $\mathbf{E}$ obeys the wave equation,

$$\nabla^2 \mathbf{E} = \frac{1}{c^2}\frac{\partial^2 \mathbf{E}}{\partial \, t^2}, \tag{B.5}$$

and is satisfied by the real part of a plane wave solution,

$$\mathbf{E} = \mathbf{A} \, e^{i \, (\mathbf{k} \cdot \mathbf{r} - \omega \, t)}, \tag{B.6}$$

where $\mathbf{A}$ is any constant describing the maximum amplitude of the electric field, $\mathbf{r}$ is the position vector, $\mathbf{k}$ is the wave vector, and ω is the frequency of oscillation. The wave vector must satisfy the following relation,

$$|\mathbf{k}| = \frac{\omega}{c} \tag{B.7}$$

Since we are dealing with a quantized wave, the photon is described with its energy ϵ and momentum $\mathbf{p}$ by the relations,

$$\epsilon = \hbar\omega, \tag{B.8}$$

$$\mathbf{p} = \hbar\mathbf{k}. \tag{B.9}$$

Since the electric field satisfies Maxwell's equation $\nabla \cdot \mathbf{E} = 0$, it follows that $\mathbf{k} \cdot \mathbf{E} = 0$, so that the electric field is always transverse to the direction of propogation. Thus there are only two orthogonal components of $\mathbf{E}$, which corresponds to only two possible states of polarization of the photon. In addition, only certain discrete values of $\mathbf{k}$ are allowed inside the enclosure, since the electric field must vanish at the edges of the enclosure. For an enclosure with dimensions L_x, L_y, and L_z, the allowed modes of the wave vector in each direction,

$$\begin{aligned} k_x &= \frac{2\pi\, n_x}{L_x}, \\ k_y &= \frac{2\pi\, n_y}{L_y}, \\ k_z &= \frac{2\pi\, n_z}{L_z}, \end{aligned} \tag{B.10}$$

where $n_\alpha = 1, 2, 3, \ldots$ in each direction. For any macroscopic volume where L_x, L_y, and L_z are large, there are very many states of the photon corresponding to any small range dk_α,

so it is easy to do some counting. Thus for given values of k_y and k_z, the number Δn_x of possible integers n_x for which k_x lies in the range $k_x + dk_x$ is,

$$\Delta n_x = \frac{L_x}{2\pi} dk_x. \tag{B.11}$$

Thus the total number of modes ΔN is given by,

$$\Delta N = \Delta n_x \, \Delta n_y \, \Delta n_z = \frac{L_x \, L_y \, L_z}{(2\pi)^3} dk_x \, dk_y \, dk_z = \frac{V}{8\pi^3} d^3\mathbf{k}, \tag{B.12}$$

where V is the volume of the enclosure, and $d^3\mathbf{k}$ is the element of volume in "$\mathbf{k}$ space." Let $f(\mathbf{k})d^3\mathbf{k}$ denote the mean number of photons per unit volume with *one* polarization and whose wave vector lies between $\mathbf{k}$ and $\mathbf{k}$ + d$\mathbf{k}$. Using the Planck relation B.4 and the number of modes of a specific wave vector per unit volume, equation B.12, then,

$$f(\mathbf{k}) \, d^3\mathbf{k} = \frac{1}{e^{\beta\hbar\omega} - 1} \frac{d^3\mathbf{k}}{8\pi^3}. \tag{B.13}$$

Given the relation B.7, we can determine the mean number of photons per unit volume of both directions of polarization and frequency between ω and ω + dω. This is achieved by summing B.13 over all the volume of $\mathbf{k}$-space within the spherical shell with radius k = ω/c and k + dk = $(\omega + d\omega)$/c, and multiplying by 2 to include both polarizations,

$$2 \, f(k)(4\pi \, k^2 \, dk) = \frac{8\pi}{(2\pi \, c)^3} \frac{\omega^2 \, d\omega}{e^{\beta\hbar\omega} - 1}. \tag{B.14}$$

To determine the mean energy per unit volume, $\bar{u}(\omega, T)$ (the energy density), we merely multiply the previous result by $\hbar\omega$,

$$\bar{u}(\omega, T)d\omega = \frac{\hbar}{\pi^2 \, c^3} \frac{\omega^3 \, d\omega}{e^{\beta\hbar\omega} - 1} \tag{B.15}$$

Converting to frequency ν,

$$\bar{u}_\nu \, d\nu = \frac{8\pi \, h \, \nu^3}{c^3} \frac{d\nu}{e^{\beta \, h \, \nu} - 1}. \tag{B.16}$$

Appendix C

Line Shape of a Fourier Transform Spectrometer

The Fourier transform spectrometer (FTS) is an invaluable tool for evaluating the spectrum of a light source. The essential setup is illustrated in Figure C.1. Light from a source enters the instrument and arrives at a beamsplitter, a semi-reflective plate which divides the light into two beams. One beam reflects off of a fixed mirror back to the beamsplitter, while the other beam reflects off of a moving mirror, which introduces a phase difference between the two beams. Interference between the two beams occurs once they recombine at the splitter, and the resulting waveform is received by the detector. The final waveform, or *interferogram*, is a function of the wavelength of light and the position of the mirror.

The phase difference, ϕ, introduced between the two beams is a function of the wavelength, λ, and the path difference introduced by the mirrors, Δx,

$$\phi = \frac{2\,\pi\,\Delta x}{\lambda}. \tag{C.1}$$

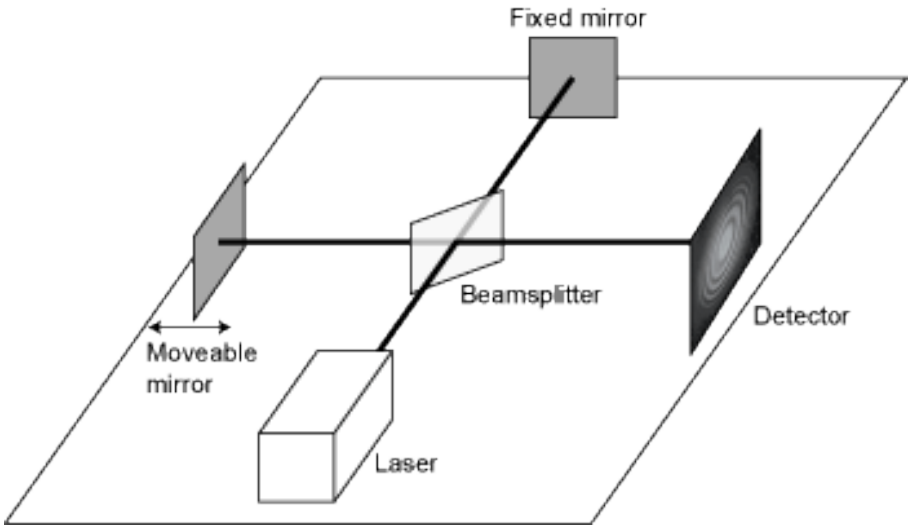

Figure C.1: Basic concept of the Fourier transform spectrometer. Light from a source (the laser in this case) enters the instrument, an is diverted into two beams by the semi-transparent beamsplitter. One beam reflects off a fixed mirror, while the other beam reflects off a moving mirror, which introduces a phase difference between the two beams. Interference occurs when the beams recombine at the beamsplitter. The combined signal finally enters the detector. The amount of interference is a function of the position of the moveable mirror and the wavelength of light.

For a plane wave entering the detector, $A\,e^{i\,\omega\,t}$, with monochromatic frequency $\omega = 2\pi\,c/\lambda$, the recombined wave is of the form,

$$\begin{aligned} E &= A\,e^{i\,\omega\,t} + A\,e^{i\,\omega\,t+i\,\phi}, \\ &= A\,e^{i\,\omega\,t} + A\,e^{i\,\phi}\,e^{i\,\omega\,t}, \\ &= A\,(\cos\omega t + i\,\sin\omega t) + A\,(\cos\phi + i\,\sin\phi)\,(\cos\omega t + i\,\sin\omega t), \\ &= A\,[\cos\omega t + \cos(\omega t + \phi) + i\,(\sin\omega t + \sin(\omega t + \phi))], \end{aligned} \tag{C.2}$$

where A is the arbitrary amplitude of the wave. The intensity of the resulting wave, I, is obtained by,

$$\begin{aligned} I = |E|^2 &= A^2\,(\cos\omega t + \cos(\omega t + \phi))^2 + A^2\,(\sin\omega t + \sin(\omega t + \phi))^2 \\ I &= 2\,A^2\,(1 + \cos\phi) \end{aligned} \tag{C.3}$$

In Fourier transform spectroscopy, it is more convenient to represent parameters as a function of the wavenumber, $\tilde{\nu} \propto 1/\lambda$, whose standard unit is cm^{-1}. For a single wavenumber and path length difference, the intensity is given as,

$$I(\Delta x, \tilde{\nu}) = I(\tilde{\nu})\,(1 + \cos(2\pi\,\tilde{\nu}\,\Delta x))$$

where $I(\tilde{\nu})$ is the spectrum of the source we are interested in. The total measured intensity at the detector for a given path length Δx, I(Δx), is a summation of all wavenumbers of

light,

$$I(\Delta x) = \int_{-\infty}^{\infty} I(\tilde{\nu})\,(1 + \cos(2\pi\tilde{\nu}\Delta x)\,d\tilde{\nu}. \tag{C.4}$$

This is just a Fourier cosine transform. The inverse transform gives us the spectral intensity, I($\tilde{\nu}$), at wavenumber $\tilde{\nu}$ in terms of the measured result I(Δx),

$$I(\tilde{\nu}) = 4\int_{-\infty}^{\infty} [I(\Delta x') - I_{ZPD}]\,\cos(2\pi\tilde{\nu}\Delta x')\,d\Delta x', \tag{C.5}$$

where I_{ZPD} is the "zero path difference" position of the mirror, where the path lengths between the mirrors are identical. Due to the finite range of the moving mirror, the limits on the integral of Δx extends from 0 to the maximum difference, typically on the order of 1 m. As a result, a monochromatic source, $\delta(\tilde{nu} - \tilde{\nu}')$, becomes a sinc function. If a purely monochromatic source were to enter the instrument, $I(\tilde{\nu}) = \delta(\tilde{\nu} - \tilde{\nu}_0)$, the interferogram would be,

$$\begin{aligned} I(\Delta x) &= \int_{0}^{\infty} I(\tilde{\nu})\,(1 + \cos(2\pi\tilde{\nu}\Delta x)\,d\tilde{\nu}, \\ &= \int_{0}^{\infty} \delta(\tilde{\nu} - \tilde{\nu}_0)\,(1 + \cos(2\pi\tilde{\nu}\Delta x)\,d\tilde{\nu}, \\ &= 1 + \cos(2\pi\tilde{\nu}_0\Delta x). \end{aligned} \tag{C.6}$$

However, since the moving mirror has only a finite path, say -L $\leq \Delta x \leq$ +L, the infinitely long interferogram in equation C.6 gets clipped at the ends by multiplying it by the rectangular

function,

$$I_{obs}(\Delta x) = I(\Delta x) \cdot \Pi\Big(\frac{\Delta x}{2\,L}\Big). \tag{C.7}$$

The ideal interferogram I(Δx) is a delta function in the frequency domain, and the rectangular function corresponds to a sinc function. Thus, the multiplication in equation C.7 is equivalent to a convolution of the delta function and the sinc function in the frequency domain,

$$\begin{aligned} I_{obs}(\Delta x) &\rightarrow I_{obs}(\tilde{\nu}), \\ I(\Delta x) \cdot \Pi\Big(\frac{\Delta x}{2\,L}\Big) &\rightarrow \delta(\tilde{\nu} - \tilde{\nu}_0) \star 2\,L\,sinc(2\,L\,\tilde{\nu}), \\ I_{obs}(\tilde{\nu}) &= 2\,L\,sinc(2\,L\,\tilde{\nu}_0). \end{aligned} \tag{C.8}$$

Thus an ideal monochromatic line is observed by a Fourier transform spectrometer as a sinc function given by equation C.8, with a FWHM of 1.207/2L. Thus the maximum optical path difference, L, determines the resolution of the instrument.

Bibliography

Abrarov, S. M. and Quine, B. M. (2011). Efficient algorithmic implementation of the voigt/complex error function based on exponential series approximation. *Applied Mathematical Computation*, 218:1894–1902.

Adams, C., Strong, K., Batchelor, R. L., Bernath, P. F., Brohede, S., Boone, C., Degenstein, D., Daffer, W. H., Drummond, J. R., Fogal, P. F., Farahani, E., Fayt, C., Fraser, A., Goutail, F., Hendrick, F., Kolonjari, F., Lindenmaier, R., Manney, G., Mc Elroy, C. T., McLinden, C. A., Mendonca, J., Park, J.-H., Pavlovic, B., Pazmino, A., Roth, C., Savastiouk, V., Walker, K. A., Weaver, D., and Zhao, X. (2012). Validation of ace and osiris ozone and no_2 measurements using ground-based instruments at 80^o n. *Atmospheric Measurement Techniques Discussions*, 5:517 – 588.

Alvarado, M. J., Payne, V. H., Mlawer, E. J., Uymin, G., Shephard, M. W., Cady-Pereira, K. E., Delamere, J. S., and Moncet1, J.-L. (2013). Performance of the line-by-line radiative transfer model (lblrtm) for temperature, water vapor, and trace gas retrievals: recent updates evaluated with iasi case studies. *Atmospheric Chemistry and Physics*, 13:6687–6711.

Armstrong, R. (1982). Line mixing in the v_2 band of co_2. *Applied Optics*, 21:2141–2145.

Arrhenius, S. (1896). On the influence of carbonic acid in the air upon the temperature of the ground. *The London, Edinburgh, and Dublin Philosophical Magazine and Journal of Science*, 5.

Bernstein, L., Bosch, P., Canziani, O., Chen, Z., Christ, R., Davidson, O., Hare, W., Huq, S., Karoly, D., Kattsov, V., Kundzewicz, Z., Liu, J., Lohmann, U., Manning, M., Matsuno, T., Menne, B., Metz, B., Mirza, M., Nicholls, N., Nurse, L., Pachauri, R., Palutikof, J., Parry, M., Qin, D., Ravindranath, N., Reisinger, A., Ren, J., Riahi, K., Rosenzweig, C., Rusticucci, M., Schneider, S., Sokona, Y., Solomon, S., Stott, P., Stouffer, R., Sugiyami, T., Swart, R., Tirpak, D., Vogel, C., and Yohe, G. (2007). Climate change 2007:synthesis report. In *IPCC Fourth Assessment Report*.

Bourassa, A., Lloyd, N., Dougenstein, D., and Llewllyn, E. (2008). Sasktran: A spherical geometry radiative transfer code for efficient estimation of limb scattered sunlight. *Journal of Quantitative Spectroscopic Radiative Transfer*, 109:52–73.

Bourassa, A. E. (2007). *Stratospheric Aerosol Retrieval From OSIRIS Limb Scattered Sunlight Spectra*. PhD thesis, University of Saskatchewan.

Buis, A. (2008). Jet propulsion laboratory. `http://www.jpl.nasa.gov/`.

Chalon, G., Cayla, F., and Diebel, D. (2001). Iasi: An advance sounder for operational meteorology. In *Proceedings of the 52nd Congress of IAF*.

Chiou, E., McCormick, M., and Chu, W. (1997). Global water vapor distributions in the stratosphere and upper troposphere derived from 5.5 years of sage ii observations (1986-1991). *Journal of Geophysical Research*, 102.

Christi, M. and Stephens, G. (2004). Retrieving profiles of atmospheric co2 in clear sky and in the presence of thin cloud using spectroscopy from the near and thermal infrared: A preliminary case study. *Journal of Geophysical Research*, 109.

Clough, S. and Iacono, M. (1995). Line-by-line calculation of atmospheric fluxes and cooling rates - application to carbon dioxide, ozone, methane, nitrous oxide and the halocarbons. *Journal of Geophysical Research*, 100.

Clough, S., Shephard, M., Mlawer, E., Delamere, J., Iacono, M., Cady-Pereira, K., Boukabara, S., and Brown, P. (2005). Atmospheric radiative transfer modeling: a summary of the aer codes. *Journal of Quantitative Spectroscopy and Radiative Transfer*, 91:233–244.

Desbiens, R., Genest, J., and Tremblay, P. (2002). Radiometry in line-shape modeling of fourier-transform spectrometers. *Applied Optics*, 41:1424–1432.

Fleagle, R. G. and Businger, J. A. (1980). *An Introduction to Atmospheric Physics*. Academic Press, Inc., Orlando, Florida 32887, U.S.A.

Fomichev, V., Ogibalov, V., and Beagley, S. (2004). Solar heating by the near-ir co_2 bands in the atmosphere. *Geophysical Research Letters*, 31.

Galli, A., Guerlet, S., Butz, A., Aben, I., Suto, H., Kuze, A., Deutscher, N., Notholt, J., Wunch, D., Wennberg, P., Griffith, D., Hasekamp, O., and Landgraf, J. (1999). The impact of spectral resolution on satellite retrieval accuracy of co_2 and ch_4. *Applied Optics*, 38:3417–3422.

Goody, R. M. and Yung, Y. L. (1989). *Atmospheric Radiation - Theoretical Basis*. Oxford University Press, 200 Madison Avenue, New York, New York 10016, 2 edition.

Griffin, M. K., hua K. Burke, H., and Kerekes, J. P. (2004). Understanding radiative transfer in the midwave infrared, a precursor to full spectrum atmospheric compensation. In *Algorithms and Technologies for Multispectral, Hyperspectral, and Ultraspectral Imagery X*, pages 348–356.

Griffioen, E. and Oikarinen, L. (2000). Limbtran: A pseudo three-dimensional radiative transfer model for the limb-viewing imager osiris on the odin satellite. *Journal of Geophysical Research*, 105.

Harris, D. C. (2010a). Charles david keeling and the story of atmospheric co_2 measurements. *Analytical Chemistry*, 82:7865–7870.

Harris, D. C. (2010b). Charles david keeling and the story of atmospheric co_2 measurements. *Analytical Chemistry*, 82:7865–7870.

Hartmann, J.-M., Tran, H., and Toon, G. (2009). Influence of line mixing on the retrievals of atmospheric co_2 from spectra in the 1.6 and 2.1 μm regions. *Atmospheric Chemistry and Physics*, 9:7303–7312.

Hase, F., Blumenstock, T., and Paton-Walsh, C. (1999). Analysis of the instrumental line shape of high-resolution fourier transform ir spectrometers with gas cell measurements and new retrieval software. *Applied Optics*, 38:3417–3422.

Henyey, L. and Greenstein, J. (1941). Diffuse radiation in the galaxy. *Astrophysical Journal*, 93:70–83.

Jardine, C. N., Boardman, B., Osman, A., Vowles, J., and Palmer, J. (2004). Methane uk. Technical report, Environmental Change Institute, University of Oxford, 1A Mansfield Road, Oxford 0X1 3SZ.

Kempler, S. (2002). *Atmospheric Infrared Sounder (AIRS) Instrument Guide*. NASA Goddard Earth Sciences Data and Information Services Center.

Kiehl, J. and Trenberth, K. E. (1997). Earth's annual global mean energy budget. *American Meteorological Society*, 78:197–208.

Kneizys, F., Abreu, L., Anderson, G., Chetwynd, J., Shettle, E., Berk, A., Bernstein, L., Robertson, D., Acharya, P., Rothman, L., Selby, J., Gallery, W., and Clough, S. (1996). Modtran report - the modtran 2/3 report and lowtran 7 model. Technical report, Phillips Laboratory.

Kochel, J.-M., Hartmann, J.-M., Camy-Peyret, C., Rodrigues, R., and Payan, S. (1997). Influence of line mixing on absorption by co_2 q branches in atmospheric balloon-borne spectra near 13 μm. *Journal of Geophysical Research*, 102:12891–12899.

Kuze, A., Suto, H., Nakajima, M., and Hamazaki, T. (2009). Thermal and near infrared sensor for carbon observation fourier-transform spectrometer on the greenhouse gases observing satellite for greenhouse gases monitoring. *Applied Optics*, 48.

Lin, C.-Y. and Lu, Z. (2014). Selection rules and transition moment integral. `http://chemwiki.ucdavis.edu/Physical_Chemistry/Spectroscopy/Fundamentals/Selection_rules_and_transition_moment_integral`.

Liou, K.-N. (1980). *An Introduction to Atmospheric Radiation*. Academic Press, Inc., 111 Fifth avenue, New York, NY 10003, U.S.A.

Ma, Q. and Tipping, R. (1991). A far wing line shape theory and its application to the water continuum absorption in the infrared region. *The Journal of Chemical Physics*, 95.

Mariani, Z., Strong, K., Wolff, M., Rowe, P., Walden, V., Fogal, P., Duck, T., Lesins, G., Turner, D., Cox, C., Eloranta, E., Drummond, J., Roy, C., Turner, D., Hudak, D., and Lindenmaier, I. (2012). Infrared measurements in the arctic using two atmospheric emitted radiance interferometers. *Atmospheric Measurement Techniques*, 5:329–344.

Maslin, M. (2004). *Global Warming*. A Very Short Introduction. Oxford University Press.

Mlawer, E. J., Payne, V. H., Moncet, J. L., Delamere, J. S., Alvarado, M. J., and Tobin, D. D. (2012). Development and recent evaluation of the mt_ckd model of continuum absorption. *Philosophical Transactions of the Royal Society A*, 370:1–37.

Monroe, R. (2014). Scripps institution of oceanography – the keeling curve. `https://scripps.ucsd.edu/programs/keelingcurve/`.

Nesmelova, L., Rodimova, O., and Tvorogov, S. (1991). On the pressure dependence of the co_2 absorption coefficient in the wing of the 4.3 μm band. *Siberian Branch of the Academy of Sciences of the USSR*.

Niro, R., Boulet, C., and Hartmann, J.-M. (2004). Spectra calculations in central and wing

regions of co_2 ir bands between 10 and 20 μm. *Journal of Quantitative Spectroscopy and Radiative Transfer*, 88.

Oreskes, N. (2004). The scientific consensus on climate change. *Science*, 306.

Osterman, G., Eldering, A., Avis, C., Chafin, B., O'Dell, C., Frankenberg, C., Fisher, B., and Wunch, D. (2014). *OCO-2 Data Product User's Guide, Pre-Launch, Simulated Data Files*. NASA Goddard Earth Science Data Information and Services Center.

Pak, B. C.-Y. (2010). *Vertical Structure of Atmospheric Trace Gases Over Southeast Australia*. PhD thesis, University of Melbourne.

Pan, L., Edwards, D. P., Gille, J. C., Smith, M. W., and Drummond, J. R. (1995). Satellite remote sensing of tropospheric co and ch_4: forward model studies of the mopitt instrument. *Applied Optics*, 34.

Ramanathan, V. (1998). Trace-gas greenhouse effect and global warming. *Ambio*, 27.

Ramanathan, V. and J.A. Coakley, J. (1978). Climate modeling through radiative-convective models. *Reviews of Geophysics and Space Physics*, 16:465–489.

Reif, F. (1965). *Fundamentals of statistical and thermal physics*. McGraw-Hill Book Company.

Rinsland, C. P., Smith, M. A. H., III, J. M. R., Park, J. H., and Farmer, C. B. (1981). Stratospheric measurements of continuous absorption near 2400 cm^{-1}. *Applied Optics*, 20.

Robbins, S. (2014). Journey through the galaxy. `http://jtgnew.sjrdesign.net/exploration_observe_spectroscopy.html`.

Rodrigues, R., Jucks, K., Lacome, N., Blanquet, G., Walrand, J., Traub, W., Khalil, B., le Doucen, R., Valentin, A., Camy-Peyret, C., Bonamy, L., and Hartmann, J.-M. (1999). Model, software, and database for computation of line-mixing effects in infrared q branches of atmospheric co_2 - i. symmetric isotopomers. *Journal of Quantitative Spectroscopy and Radiative Transfer*, 61:153–184.

Rothman, L., Gordon, I., Babikov, Y., Barbe, A., Benner, D. C., Bernath, P., Birk, M., Bizzocchi, L., Boudon, V., Brown, L., Campargue, A., Chance, K., Cohen, E., Coudert, L., Devi, V., Drouin, B., Fayt, A., Flaud, J.-M., Gamache, R., Harrison, J., Hartmann, J.-M., Hill, C., Hodges, J., Jacquemart, D., Jolly, A., Lamouroux, J., Roy, R. L., Li, G., Long, D., Lyulin, O., Mackie, C., Massie, S., Mikhailenko, S., Muller, H., Naumenko, O., Nikitin, A., Orphal, J., Perevalov, V., Perrin, A., Polovtseva, E., Richard, C., Smith, M., Starikova, E., Sung, K., Tashkun, S., Tennyson, J., Toon, G., Tyuterev, V., and Wagner, G. (2013). The hitran 2012 molecular spectrocopic database. *Journal of Quantitative Spectroscopy & Radiative Transfer*, 130:4–50.

Schmidt, G. A., Ruedy, R. A., Miller, R. L., and Lacis, A. A. (2010). Attribution of the present-day total greenhouse effect. *Journal of Geophysical Research*, 115.

Seidel, D. J. (2002). *Water Vapor: Distribution and Trends*, chapter 2. John Wiley & Sons.

Sissenwine, N. and Teweles, S. (1976). *U.S. Standard Atmosphere, 1976*. NASA.

Strow, L. and Reuter, D. (1988). Effect of line mixing on atmospheric brightness temperature near 15 μm. *Applied Optics*, 27.

Tanaka, T., Fukabori, M., Sugita, T., Yokota, T., Kumazawa, R., Watanabe, T., and Nakajima, H. (2008). Line shape of the far-wing beyond the band head of the co_2 $?_3$ band. *Journal of Molecular Spectroscopy*.

Thomsen, V. (2006). A timeline of atomic spectrocopy. *Spectroscopy*, 21:32–42.

Toon, G., Blavier, J.-F., Washenfelder, R., Wunch, D., Keppel-Aleks, G., Wennberg, P., Connor, B., Sherlock, V., Griffith, D., Deutscher, N., and Notholt, J. (2009). Total column carbon observing network (tccon). In *Fourier Transform Spectroscopy*.

Turner, D., Chevallier, F., Garand, L., Rayer, P., Scott, N., and van Delst, P. (2001). An intercomparison of line-by-line radiative transfer codes for simulating hirs radiances. Technical report, Meteorological Service of Canada - Atmospheric and Climate Science Directorate.

Vaara, M. (2003). Use of ozone depleting substances in laboratories. Technical report, Nordic Chemical Group.

Woods, A. (2006). Medium-range weather prediction – the european approach. Technical report, European Centre for Medium-Range Weather Forecasts.

Zhang, Y. (1999). Modis ucsb emissivity libary. `http://www.icess.ucsb.edu/modis/EMIS/html/em.html`.